

Paula de Oliveira Guglielmi

**Development of fiber-reinforced
all-oxide composites manufactured
by a novel lamination route**



Cuvillier Verlag Göttingen
Internationaler wissenschaftlicher Fachverlag



Development of fiber-reinforced all-oxide composites manufactured by a novel lamination route





Development of fiber-reinforced all-oxide composites manufactured by a novel lamination route

Vom Promotionsausschuss der
Technischen Universität Hamburg-Harburg
zur Erlangung des akademischen Grades
Doktor-Ingenieurin (Dr.-Ing.)
genehmigte Dissertation

von

Paula de Oliveira Guglielmi

aus

Criciúma

2016



Bibliografische Information der Deutschen Nationalbibliothek

Die Deutsche Nationalbibliothek verzeichnet diese Publikation in der Deutschen Nationalbibliografie; detaillierte bibliografische Daten sind im Internet über <http://dnb.d-nb.de> abrufbar.

1. Aufl. - Göttingen: Cuvillier, 2016

Zugl.: (TU) Hamburg-Harburg, Univ., Diss., 2016

1. Gutachter: Prof. Dr. rer. nat. Gerold A. Schneider
2. Gutachter: Prof. Dr.-Ing. Bodo Fiedler

Tag der mündlichen Prüfung: 16. Oktober 2015

© CUVILLIER VERLAG, Göttingen 2016

Nonnenstieg 8, 37075 Göttingen

Telefon: 0551-54724-0

Telefax: 0551-54724-21

www.cuvillier.de

Alle Rechte vorbehalten. Ohne ausdrückliche Genehmigung des Verlages ist es nicht gestattet, das Buch oder Teile daraus auf fotomechanischem Weg (Fotokopie, Mikrokopie) zu vervielfältigen.

1. Auflage, 2016

Gedruckt auf umweltfreundlichem, säurefreiem Papier aus nachhaltiger Forstwirtschaft.

ISBN 978-3-7369-9203-0

eISBN 978-3-7369-8203-1



For my father, who would certainly be very proud of me at this moment.

- Love you forever -





Acknowledgement

The contents of this thesis are based on the research work carried out during my stay as a research assistant at the Institute of Advanced Ceramics of the Hamburg University of Technology. The work was conducted as part of the project “Low-cost and reliable production of oxide ceramic matrix composites”, within the framework of the Brazilian-German Collaborative Research Initiative on Manufacturing Technology (BRAGECRIM).

I would like to sincerely thank Prof. Dr. rer. nat. Gerold A. Schneider for the opportunity of conducting my research work at his institute and for accepting to be my doctoral supervisor (*Doktorvater*). Thanks also to Prof. Dr.-Ing. Bodo Fiedler for reviewing this thesis and accepting to be my second examiner. Prof. Dr.-Ing. Stefan Heinrich is kindly acknowledged for accepting to be the chairman of the evaluation committee of this thesis.

My most sincere gratitude to Dr. Rolf Janssen, for giving me the opportunity of working in such an exciting and interesting collaborative project, together with researchers of my home university in Brazil. I would also like to thank him for his guidance and support, and, at the same time, for giving me the freedom to work independently and to develop my research skills during this period.

Thanks to Prof. Dr.-Ing. Dachamir Hotza, from the Federal University of Santa Catarina (UFSC), Brazil, for his kindness, support and great collaborative work during this project. I am equally grateful to Prof. Dr. Hazim Al-Qureshi and to Dr. Daniel García, both from UFSC, for also supporting and encouraging me throughout my whole doctoral work. Thank you very much for your scientific guidance, for your critical reviews and for being such great mentors!

I am deeply grateful to my dear students Gabriel Nunes, Seyed Goushegir, Murilo Hablitzel, Diego Blaese, Daniel Goulart and Victor Lauth, for their commitment, dedication and excellent scientific work, as well as for the lovely and trustful work environment. Thanks also to all other Brazilian students that came to TUHH in the



framework of the BRAGECRIM project, for the very fruitful discussions and excellent teamwork.

My very special thanks to my colleagues from the Institute of Advanced Ceramics, for always being so friendly and helpful, and for providing me with a very pleasant work environment. I had a great time working with you!

Finally, I would like to thank my family and friends, especially my mother, Dóris, my brothers, Antonio José and Luís Fernando, and my beloved husband, Ricardo, for always being there for me, and for their unconditional love, support, and encouragement throughout the period of this work. Words are not enough to express my gratitude to you. I love you!



Contents

Acknowledgement	v
Contents	vii
Nomenclature	ix
1 Introduction and Motivation	1
1.1 Outline of the thesis.....	3
2 Literature review	5
2.1 Ceramic matrix composites	5
2.2 All-oxide ceramic matrix composites	18
2.3 Reaction Bonded Aluminum Oxide.....	34
3 Preliminary studies: Definition of a suitable thermal treatment for RBAO- matrix composites	39
3.1 Introduction.....	39
3.2 Materials and methods.....	40
3.3 Theoretical calculations for the prediction of crack deflection/penetration behavior	46
3.4 Results.....	48
3.5 Discussion	56
3.6 Conclusion	58
4 Development of the novel processing route	59
4.1 Introduction.....	59
4.2 Materials and methods.....	61
4.3 Concept 1: Direct impregnation of fiber fabrics with the paraffin-based suspension	67
4.4 Concept 2: Introduction of a liquid slurry for the impregnation of fiber tows.....	69



4.5	Concept 3: Modification of the consolidation process to achieve higher fiber contents.....	73
4.6	Established Processing Route	76
4.7	Conclusion	78
5	A8Z2-matrix CMCs: matrix characterization and predictions of crack deflection	81
5.1	Introduction.....	81
5.2	Methods	82
5.3	Results.....	85
5.4	Discussion.....	92
5.5	Conclusion	95
6	RBAO-matrix CMCs: processing and microstructural features	97
6.1	Introduction.....	97
6.2	Production of low-to-zero shrinkage RBAO-matrix composites.....	98
6.3	Void formation: investigation of causes and solutions for this processing problem	106
6.4	Production of void-free RBAO-matrix composites.....	118
6.5	Conclusion	119
7	Mechanical Properties of CMCs.....	123
7.1	Introduction.....	123
7.2	Materials and methods.....	123
7.3	Results.....	126
7.4	Discussion.....	133
7.5	Conclusion	139
8	Summary.....	141
	References.....	145
	Curriculum Vitae	157



Nomenclature

2D	Two-directional
4PB	Four-point bending
a	Coefficient related to the slope of the linear function between fracture toughness and porosity
a_i	Initial notch length in SEVNB specimens
α	Elastic mismatch parameter
A8Z2	An oxide matrix composed of 80 vol% alumina and 20 vol% zirconia
A_{tex}	Total area of fiber fabric in a given composite sample
AZ-12AS	A8Z2-matrix composite sintered at 1200°C
AZ-12AG	A8Z2-matrix composite, sintered at 1200°C and aged at 1100°C for 500 h.
AZ-13AS	A8Z2-matrix composite sintered at 1300°C
b	Sample width
β	Efficiency factor related to fiber orientation
φ	Efficiency factor related to fiber integrity after processing
CIP	Cold isostatic pressing
CMC	Ceramic matrix composite
CSM	Continuous stiffness measurement
CTE	Coefficient of thermal expansion
CVI	Chemical vapor infiltration
d	Deflection of specimen at four-point bending
DBP	Double-belt press
DTA	Differential thermal analysis
E	Elastic modulus
E_0	Elastic modulus of a matrix without pores



E_c	Flexural modulus of a composite
E_m	Elastic modulus of the matrix
E_f	Elastic modulus of the fibers
ε_m	Matrix strain
ε_{m_u}	Matrix failure strain
ε_f	Fiber strain
ε_{f_u}	Fiber failure strain
ε_c	Composite strain
ε_{4PB_u}	Strain at fracture in four-point bending
F	Fiber
G_d	Energy release rate associated with crack deflection at an interface
G_p	Energy release rate associated with crack penetration across an interface
h	Sample thickness
IB	Intra-bundle matrix
IT	Inter-textile matrix
ILSS	Interlaminar shear strength
k	Coefficient related to the slope of the linear function between elastic modulus and porosity
K_o	K_{IC} of a material without pores
K_f	K_{IC} of the fiber
K_{IC}	Fracture toughness in mode I of crack propagation
K_m	K_{IC} of the matrix
L	Load
L_{max}	Maximum load
l	Sample length
LPI	Liquid precursor infiltration
LPIM	Low pressure injection molding
LS	Linear shrinkage

LSR	Linear shrinkage rate
LDC	Linear Dimensional Change
LDC _{IB}	Linear dimensional change of IB matrices
LDC _{IT}	Linear dimensional change of IT matrices
LDC _o	Linear dimensional change for $v_{Al} = 0$
m_{tex}^*	Mass per unit area of textile
n	Number of fabric layers in a given composite sample
η	Coefficient related to the slope of the linear function between LDC _{IB} and v_{Al}
ω	Proportionality constant between Γ_i and Γ_m
P	Porosity
ρ_s	Density of a sintered sample
ρ_t	True density of a powder
ρ_f	Fiber density
RBAO	Reaction bonded aluminum oxide
RB-12AS	RBAO-matrix composite sintered at 1200°C
RB _d -12AS	RBAO-matrix composite sintered at 1200°C, produced with RBAO powders dried at 300°C for 5 h.
RT	Room temperature
S	Outer load span in flexural tests
S_i	Inner load span in four-point flexural tests
SBS	Short beam shear
SEM	Scanning electron microscope
SEVNB	Single-edge V-notch beam
σ_o	Matrix cracking stress in a composite
σ_f	Stress on the fiber at a given strain
σ_{f_u}	Ultimate fiber tensile strength
σ_m	Stress on the matrix at a given strain
σ_{m_u}	Ultimate matrix tensile strength
σ_f'	Stress on the fiber at matrix failure strain



σ_c	Stress on composite at a given strength
σ_{cu}	Ultimate composite strength under axial loading
σ_{cb}	Composite strength under bending
σ_{4PB}	Stress at the outermost surface in 4-point bending
σ_{4PB_u}	Flexural strength at 4-point bending
σ_{3PB}	Stress at the outermost surface in 3-point bending
Σ	Crack deflection parameter
TD	Theoretical density
TG	Thermogravimetry
T_M	Geometric factor for SEVNB specimens
T_{Al}	Melting temperature of aluminum
Γ	Toughness
Γ_i	Toughness of the interface
Γ_f	Toughness of the fiber
Γ_m	Toughness of the matrix
Γ_1	Toughness of a material 1, in which a crack is propagating
Γ_2	Toughness of a material 2, on which a crack is impinging
τ_{3PB}	Maximum shear stress in 3-point bending
V_c	Composite volume
v_f	Fiber volume content
$v_{f_{min}}$	Minimum fiber volume content, so that $\sigma_{cu} = v_f \sigma_f$ applies
v_{Al}	Volume fraction of aluminum
YSZ	Yttria-stabilized zirconia
WMC	Weak matrix composite
WIC	Weak interface composite



1 Introduction and Motivation

Overcoming the brittleness of ceramics is still a relevant topic in materials science. Extensive research effort has been dedicated to develop microstructural designs that enhance the toughness of these materials. One of the most effective approaches is the incorporation of continuous ceramic fibers as reinforcement [1]. Provided the fiber-matrix interfaces are weak, toughening mechanisms such as crack deflection, crack bridging and fiber pullout take place, yielding a quasi-ductile fracture behavior to the so-called ceramic matrix composite (CMCs) [1,2].

Among the different classes of CMCs, much attention has been drawn to all-oxide systems because of their chemical stability in oxidizing environments [3,4]. Toughness is typically achieved in these materials by a weak, porous matrix that enables debonding at fiber-matrix interfaces [3,5]. These composites are usually produced by liquid infiltration techniques, in which matrix particles are impregnated into fiber tows or fabrics via aqueous slurries or sols [3,6–8] and then sintered for consolidation. One of the challenges of this process is the consolidation of flawless matrices, since the constrained shrinkage imposed by the rigid network of fibers causes the formation of matrix cracks during drying and sintering [1,3]. Such cracks may not just be detrimental to the mechanical properties of the composite [8–10], but also compromise its thermal shock resistance by decreasing the thermal conductivity of the material [11,12]. A method to mitigate the formation of these cracks is therefore of great interest.

In order to produce crack-free CMCs, matrix shrinkage must be avoided in both drying and sintering steps [10]. When conventional liquid infiltration routes are used to produce composites reinforced with woven fabrics, drying cracks form during the extraction of the liquid carrier, mainly in matrix-rich regions located at the crossover between fiber tows [6,7]. Alternatives to mitigate these drying cracks were proposed by Levi *et al.* [7] and Yang *et al.* [13] and consist in reducing the amount of unreinforced matrix regions by filling the large inter-tow spaces with chopped fibers or large particles, respectively. Another possible



method was proposed by Mah *et al.* [10] and consists of a shrinkage-free freeze casting of camphene-based slurries used to infiltrate fiber fabrics or preforms. Although promising results were obtained by these methods, the viability of using them to produce all-oxide CMCs in large scales should yet be proved.

With regard to the sintering-related cracks, they can be avoided by using reactive sintering routes, which ideally reduce sintering shrinkages to zero [14]. Reaction bonded aluminum oxide (RBAO) arises here as a promising matrix material for all-oxide CMCs. The sintering shrinkage of RBAO ceramics can be partially or totally compensated by the expansion associated with the oxidation of Al particles, present in the precursor powders, during heat treatments in air [15,16]. Nevertheless, although often suggested in the literature as a promising matrix material [3,17,18], there is to date no report of the use of RBAO in the production of full-scale, all-oxide composites. Research in this area is restricted to the analysis of model and mini composites consisting of a few fibers or tows dispersed in the matrix [17–19]. Therefore, the benefits and possible drawbacks of using RBAO to produce all-oxide CMCs and the related effects on the final material properties are still unclear.

This work aims at investigating the viability of using RBAO to produce all-oxide CMCs with a reduced amount of shrinkage-related cracks. Due to the high reactivity of aluminum particles with water, conventional aqueous slurries cannot be used in the processing [16]. A novel manufacturing route is therefore developed, in which organic particle carriers are used. In this route, fiber woven fabrics are first infiltrated with a low viscous ethanol-based slurry for the impregnation of matrix particles within the fiber bundles. In a subsequent step, the large inter-tow voids are filled with a paraffin-based suspension used for the lamination of thermoplastic preregs. This two-step impregnation route allows for an enhanced filling of void spaces within the fiber fabrics and guarantees a homogenous distribution of matrix particles throughout the green composites. Thereby, shrinkage is reduced and cracks are avoided also in the green state. Composites with both RBAO and a reference, all-oxide matrix are produced and characterized. A detailed analysis of the microstructure and mechanical properties of the produced composites allows for a critical evaluation of the developed processing route, as well as of the use of RBAO matrix in all-oxide CMCs.



1.1 Outline of the thesis

This thesis is divided into eight chapters. Chapters 1 and 2 comprise, respectively, this introduction and a literature review of relevant topics related to this work. Chapters 3 to 7 present the methodology used to achieve the objectives of this work, as well as the obtained results. Each of these chapters can be understood as a sub-project and can, in principle, be read separately. This structure improves the readability and comprehension of this thesis, since the methods used in each chapter differ from one another.

Chapter 3 presents preliminary studies performed on RBAO-matrix model composites, in order to determine suitable thermal treatment parameters for such composites. The knowledge acquired in this chapter is used later in the production of full-scale, all-oxide composites by the novel processing route developed in this work. Part of the experiments presented in this chapter were performed with the help of M.Sc. Seyed M. Goushegir, during his master thesis [20]. Valuable inputs to the theoretical model used in this chapter to evaluate the experimental data were given by M.Sc. João G. P. da Silva during his interchange at the Institute of Advanced Ceramics at TUHH.

In Chapter 4, the development of the novel processing route is presented, which is carried out using conventional, pure oxide matrix materials. The introduction of RBAO matrices in the composites requires other development steps, which are presented in Chapter 6. Part of the experiments presented in these chapters were performed with the help of Eng. Murilo P. Hablitzel, during his bachelor thesis [21].

Chapter 5 shows the microstructural characterization of reference composites produced with a pure oxide matrix consisting of 80 vol% Al_2O_3 and 20 vol% tetragonal ZrO_2 (A8Z2 matrix). This is the same composition as that of RBAO after the complete oxidation of the aluminum particles. Apart from being a reference material, these composites serve to evaluate the novel developed processing route. Finally, the mechanical properties of the different composites produced in this work are presented in Chapter 7, which is followed by a summary in Chapter 8.





2 Literature review

2.1 Ceramic matrix composites

Despite attractive properties such as temperature stability, high strength, low density, and good corrosion and erosion resistance, the inherent brittleness of ceramics still prevents their use in many structural applications. This drawback fostered the development of several microstructural designs to increase toughness and damage tolerance of these brittle materials. Microcracking, transformation toughening and reinforcement with particles, whiskers or continuous fibers are some examples of these designs [1,3,22], being the latter suggested as the most promising [1].

Long fiber reinforced CMCs present higher temperature capability than metals and intermetallics and larger strain to failure than monolithic ceramics [23,24]. Their mechanical behavior is normally referred to as *quasi-ductile*, even though all components (matrix, fibers and interphases) are brittle. These features, combined with their low density and corrosion resistance, make CMCs interesting for thermomechanical applications where weight saving, extended lifetime of components and elevated operating temperatures are desirable [4,25].

However, CMCs are a relatively new class of structural materials, being their use still limited to some niche applications in the aerospace and military industries, such as thermal protection [3,26] and engine nozzles [26,27], as well as brake systems for aircrafts and sport cars [27,28]. Nevertheless, the demand on high temperature materials for power generation systems, such as jet engines and stationary turbines, continues driving the interest of researchers and engineers in further developing and understanding these materials [4].

Since the early developments of fiber reinforced CMCs in the 1970s [29,30], much attention has been given to non-oxide systems composed of carbon or silicon carbide fibers, reinforcing a carbon or silicon carbide matrix [28,31,32]. The interest in these materials is explained by the high strength presented by the

covalent-bonded, non-oxide fibers at high temperatures and, most especially, by their excellent creep resistance [3,25]. However, non-oxide CMCs are prone to oxidation, which considerably limits their lifetime during applications in oxidative atmospheres [1,32,33]. This fundamental drawback has arisen the interest in developing composites consisting entirely of oxides [1,3,4,23]. The so-called all-oxide CMCs are the focus of the present work. A better overview on the developments in this area over the last decades is given in section 2.2. The following sections are dedicated to the mechanical behavior and toughening mechanisms associated with the reinforcement of ceramics.

2.1.1 Predictions of composite strength by the rule of mixtures

A fundamental difference between CMCs and other composite materials is that, in the former, both matrix and fibers are brittle. Unlike metallic or polymeric matrices, ceramic matrices are neither compliant nor ductile and cannot deform plastically prior to fracture [30]. Additionally, CMCs are considered inverse composites, since the failure strain of the matrix is lower than that of the fibers [34], as schematically shown in the stress-strain diagram in Figure 1(a). Consequently, the matrix is the first component to fail when a CMC is loaded.

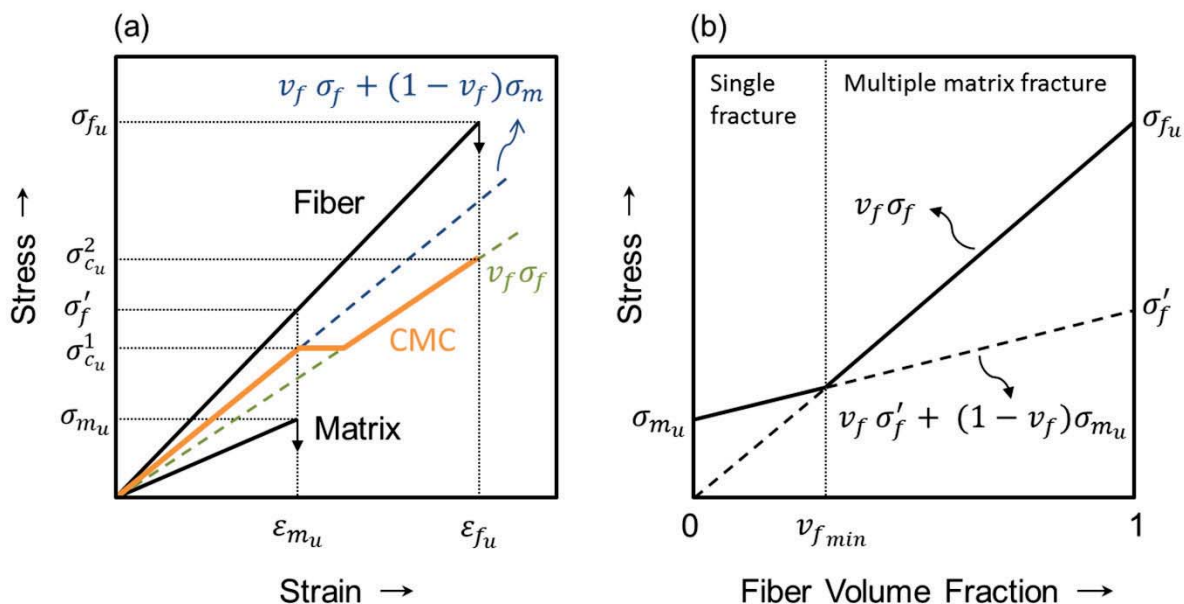


Figure 1: Schematic diagrams of an idealized ceramic matrix composite (CMC): (a) Stress-strain relationships of fiber, matrix and composite; (b) Dependence of composite failure stress on the fiber volume fraction. Adapted from Chawla [1] and Hull and Clyne [35].

Based on the mechanical properties of the fibers and the matrix and considering the volume fractions of both components, the mechanical behavior of the composite under axial tensile loading can be predicted by the rule of mixtures, as schematically shown in Figure 1. For that, it is assumed that the continuous fibers are parallel, unidirectional and homogeneously distributed in the matrix, besides presenting identical diameter and mechanical strength.

Before matrix cracking, i.e., for strains up to the failure strain of the matrix, ε_{m_u} , fibers and matrix are equally strained and the stress on the composite under axial loading, σ_c , can be calculated as follows [1,35]:

$$\sigma_c = v_f \sigma_f + (1 - v_f) \sigma_m \quad \text{Eq. 1}$$

where v_f is the volume fraction of fibers in the composite and σ_f and σ_m are the stresses on the fibers and the matrix at a given strain, respectively.

When ε_{m_u} is achieved, cracks start propagating in the matrix. Two situations may happen beyond this point: (i) if the fibers fail before the load is completely transferred from the matrix to them, then the ultimate tensile strength of the composite, $\sigma_{c_u}^1$, is a weighted average of the failure stress of the matrix, σ_{m_u} , and the stress applied to the fibers at the onset of matrix cracking, σ_f' [35]:

$$\sigma_{c_u}^1 = v_f \sigma_f' + (1 - v_f) \sigma_{m_u} \quad \text{Eq. 2}$$

If otherwise (ii) matrix cracks do not lead to the premature failure of the fibers, then a knee appears in the stress-strain curve, as schematically shown in Figure 1(a). Load is then progressively transferred from the matrix to the intact fibers, until it is completely carried by the reinforcement. In this case, failure occurs when the strain reaches the failure strain of the fibers, ε_{f_u} , and the ultimate tensile strength of the composite, $\sigma_{c_u}^2$, is simply given by [35]:

$$\sigma_{c_u}^2 = v_f \sigma_{f_u} \quad \text{Eq. 3}$$

where σ_{f_u} is the fiber ultimate tensile strength. The fact that the mechanical strength of the composite is, in this case, controlled by the fibers does not deplete the importance of having a matrix in the composite. Composite matrices are necessary, for instance, to ensure material integrity, to protect the fibers, to give a



shape to fiber-reinforced components, to guarantee cohesion in the transverse direction and for load transfer between matrix and fibers.

The situation described by Eq. 3 is only possible if the amount of fibers in the composite is enough to fully sustain the additional load, which was being carried by the matrix prior to its fracture. The minimum fiber volume fraction $v_{f_{min}}$ necessary for this to happen is determined by setting Eq. 2 equal to Eq. 3, resulting in [1,35]:

$$v_{f_{min}} = \frac{\sigma_{m_u}}{\sigma_{f_u} - \sigma'_f + \sigma_{m_u}} \quad \text{Eq. 4}$$

The dependence of composite strength on the fiber volume fraction is depicted in Figure 1(b). This figure allows for the following conclusions: (i) since $\sigma_{m_u} < \sigma'_f$, ceramic fibers will always lead to an increase in the CMC strength, being the benefit more pronounced when $v_f > v_{f_{min}}$, and (ii) the higher the fiber volume fraction, the higher the strength of the composite. In addition, according to Chawla [1], if $v_f > v_{f_{min}}$, a multiple crack failure occurs (non-brittle behavior), while for $v_f < v_{f_{min}}$, a single crack dominates the failure of the material (brittle behavior).

Although this treatment offers a good estimation of the composite strength under tensile load, it significantly simplifies the reality [1,35]. For instance, after the onset of microcracking, the slope of the stress-strain curve does not fall to zero. Instead, it changes gradually due to load transfer across the fiber-matrix interfaces [35,36]. Additionally, fibers follow a statistical Weibull distribution and do not present a single strength value, as assumed here. Moreover, a very important aspect of CMCs is not being considered in this analysis: the role of the fiber-matrix interfaces in the mechanical response of these materials.

In order for the fibers to be able to carry load after matrix failure, not just v_f must be greater than $v_{f_{min}}$, but also the fibers should remain intact, even though cracks are propagating in the matrix. For this to happen, matrix cracks must be either arrested or deflected at the fiber-matrix interfaces [33,34]. In CMCs, if the bonding between matrix and fibers is very strong, matrix cracks induce fiber fracture by a notch effect, even if $v_f > v_{f_{min}}$ [34]. In this case, the strength of the composite is most likely given by Eq. 2 and the material undergoes brittle failure. Otherwise, if the fiber-matrix bonding is weak enough, matrix cracks by-pass the fibers and

leave them intact and capable of carrying load [1,34]. In this case, composite strength is dominated by Eq. 3 and failure is accompanied by a series of energy absorbing mechanisms, such as matrix microcracking, debonding at fiber-matrix interface, crack bridging and fiber pullout.

Therefore, the reinforcement of a ceramic material with continuous fibers may not just increase its strength, but also, and frequently more important, may increase toughness and favor a non-catastrophic fracture of the material [1,30]. Hence, in order to design a CMC with enhanced mechanical properties, not just the fiber volume fraction should be optimized but, most essential, the interface between fibers and matrices.

Interfaces in CMCs have two important functions: (i) promote the deflection of matrix cracks and (ii) enable load transfer between matrix and fibers [34]. The first is crucial to achieve both strength and toughness, since both properties require that fibers are preserved from the damage of the matrix. The latter must be effective, so that high strength values are achieved [2,34]. On the one hand, crack deflection requires weak interfaces. On the other hand, load transfer is favored by fairly strong ones [34]. The design of effective interfaces for CMCs is therefore very challenging. They should be weak to promote crack deflection, but not too weak, so as to deplete load transfer. They should be strong to promote a good load transfer, but not too strong, so that fibers are prematurely broken, leading to the brittle failure of the composite. However, load transfer issues are usually disregarded and researchers focus mainly on the development of weak interfaces for crack deflection [2].

2.1.2 Microstructural designs for damage tolerance in CMCs

The different microstructural concepts to achieve crack deflection in CMCs are depicted in Figure 2. The most common concept is the introduction of a *weak interphase* between matrix and fibers (Figure 2(a)). This is achieved either by an *in-situ* chemical reaction during processing, or by coating the fibers prior to composite manufacturing [34,37]. This approach has been extensively used in non-oxide composites, mainly using C (carbon) or BN (boron nitride) interphases [34]. The disadvantage of these coatings is their susceptibility to oxidation, which normally leads to the embrittlement of the material [37]. If the interphase is



volatilized by oxidation, matrix and fibers may react and form a strong bonding that no longer allows the deflection of matrix cracks [4,38].

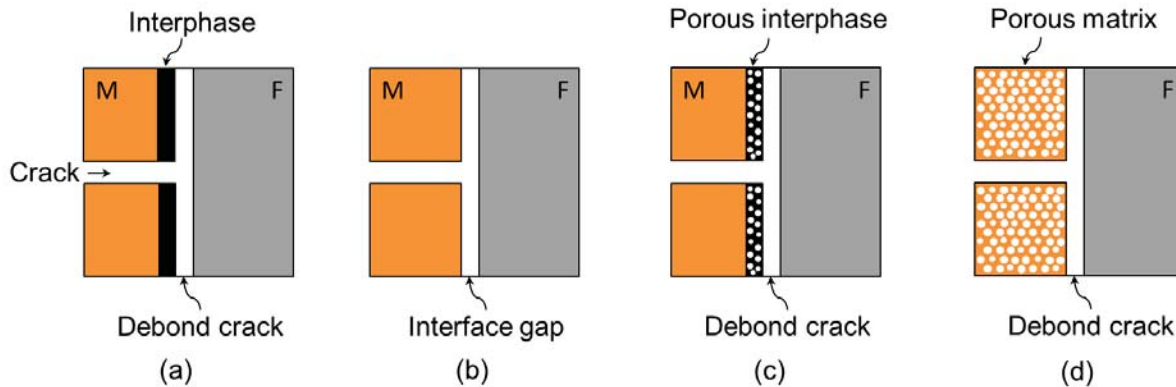


Figure 2: Microstructural designs for damage tolerance in CMCs: (a) weak interphase; (b) fugitive coating; (c) porous interphase; (d) porous matrix. M and F indicate the matrix and fiber, respectively. Adapted from Zok [4].

For all-oxide composites, La-monazite (LaPO_4) interphases show good results in terms of crack deflection, since this rare-earth phosphate bonds weakly to oxides and leads to low-toughness interfaces [4,23]. A drawback of this coating is the strength degradation caused on the oxide fibers due to deleterious reactions with monazite precursors during the necessary heat treatments [4,39].

Another way of controlling the interface properties in CMCs is through *fugitive coatings* (Figure 2(b)). In this concept, fibers are coated with carbon either by chemical vapor deposition or through pyrolysis of organic precursors prior to composite manufacturing. A post treatment at moderate temperatures volatilizes the carbon interphase by oxidation and leaves a narrow gap between matrix and fibers [4,33]. Since there is virtually no contact between matrix and fibers, this concept has the drawback of significantly reducing the load transfer between both components, which reduces composite strength [2]. Additionally, during long-term applications at high temperatures, embrittlement of the composite due to the strengthening of the interfaces may occur, since there is no barrier against chemical reaction and bonding between matrix and fibers [4].

Porous coatings (Figure 2(c)) are also a viable concept for crack deflection in CMCs, being most commonly used in all-oxide systems. They can be formed by coating the fibers with a mixture of oxide and carbon particles. After processing the composite, carbon is burned out, leading to an interphase with controlled porosity [34,38]. The bonding between fiber and matrix is strong at the contact

points, but the overall mechanical response of the interphase is weak. Crack deflection occurs within this coating, where the pores offer a low fracture energy path for the matrix cracks [38]. The successful use of this approach relies on the stability of the coating porosity at high temperatures [4]. Any densification of the coating leads to the strengthening of the interphase, harming the mechanical properties of the composite.

The *porous matrix* approach (Figure 2(d)) was developed as an extension of the porous coatings [5]. It has the advantage of obviating the need for fiber coating prior to composite processing [4]. This is the most common microstructural design used in all-oxide composites and will be discussed in more detail in section 2.2.

2.1.3 Mechanics of crack deflection

The selection of the microstructural design for crack deflection in a specific CMC depends, among other factors, on the relative elastic properties between matrix and fibers. This is illustrated in Figure 3, which shows the prediction for crack deflection or penetration into an interface between dissimilar elastic materials, according to calculations presented by He and Hutchinson [40]. This diagram may be understood as a debond map [38], in which the transition line represents the ratio G_d/G_p between the energy release rate associated with crack deflection into the interface, G_d , and the energy release rate associated with crack penetration G_p across the interface [40]. In case of a fiber-reinforced ceramic composite, a matrix crack is expected to deflect at the fiber-matrix interface when $\Gamma_i/\Gamma_f < G_d/G_p$ [40], where Γ_i is the toughness of the interface and Γ_f is the toughness of the fiber. Conversely, a matrix crack is expected to penetrate into the fiber if $\Gamma_i/\Gamma_f > G_d/G_p$ [40].

As shown in Figure 3, the ratio G_d/G_p is controlled by the elastic mismatch parameter, α , between the material in which the crack is propagating and the material on which the crack is impinging. For a CMC in which a matrix crack approaches a fiber-matrix interface, α is given by:

$$\alpha = \frac{E_f - E_m}{E_f + E_m} \quad \text{Eq. 5}$$

where E_f and E_m are the plain strain elastic modulus of fiber and matrix, respectively.

For the special case in which matrix and fibers have very similar elastic moduli ($\alpha \approx 0$), Γ_i/Γ_f should not overcome 0.25 for crack deflection to occur. As a result, an interphase with a low toughness ($< 1/4 \Gamma_f$) is required for the material to present a damage tolerant behavior [1,34,41]. This is normally the case for composites with dense matrices, such as SiC/SiC CMCs produced by chemical vapor infiltration (CVI) and dense oxide matrix CMCs [41]. These composites are called here *weak interphase composites* (WIC).

In case of porous-matrix composites, the fibers are much stiffer than the matrix, what results in values of $\alpha > 0.5$ [4]. The interface domain is therefore not so crucial, since larger values of elastic mismatch allows for a significant increase in the toughness ratio between interface and fiber, without inducing the brittle failure of the composite [33,42]. Typical examples of these *weak matrix composites* (WMC) are those fabricated by liquid infiltration processes using liquid silicon or ceramic slurries [33].

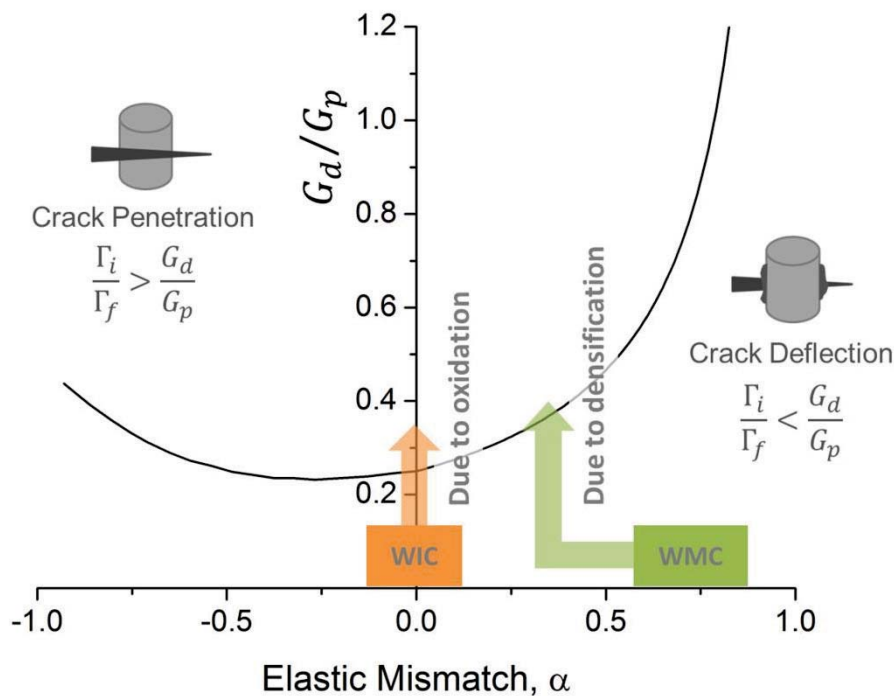


Figure 3: Ratio of energy release rates associated with deflection or penetration of a crack at the interface between dissimilar elastic materials, according to He and Hutchinson [40]. The conditions for the deflection or penetration of a matrix crack at a fiber-matrix interface in a CMC are indicated. In addition, the influence of microstructural changes of a CMC due to oxidation of interphases or matrix densification is qualitatively shown, according to Koch [33].

The influence of microstructural changes in the interphase or matrix during service at high temperatures is qualitatively shown in Figure 3 for both WICs and WMCs. If the increase in interfacial toughness due to oxidation of interphases or matrix densification leads to values of $\Gamma_i/\Gamma_f > G_d/G_p$, then crack penetration will occur and the composite will fail in a brittle manner [33].

2.1.4 Mechanical behavior and toughness in CMCs

Debonding and crack deflection at fiber-matrix interfaces are prerequisites for other toughening mechanisms such as crack bridging and fiber pullout to occur in CMCs [1]. In an ideal case, these mechanisms lead to a stress-strain curve such as that depicted in Figure 4(a).

Three regions can be identified in this diagram. Initially (region I), the mechanical response of the composite is linear elastic. In this regime, matrix and fibers are equally strained and the stress on the composite can be calculated by the rule of mixtures, according to Eq. 1 [33,43]. The linear elastic regime ends when cracks start propagating in the matrix at a stress σ_c [1,33]. Above this stress (region II), nonlinearity is a result of load transfer between matrix and fibers and of a series of failure mechanisms, such as matrix microcracking, fiber-matrix debonding, sliding between fibers and matrix, crack bridging and eventually, fiber fracture [1,33].

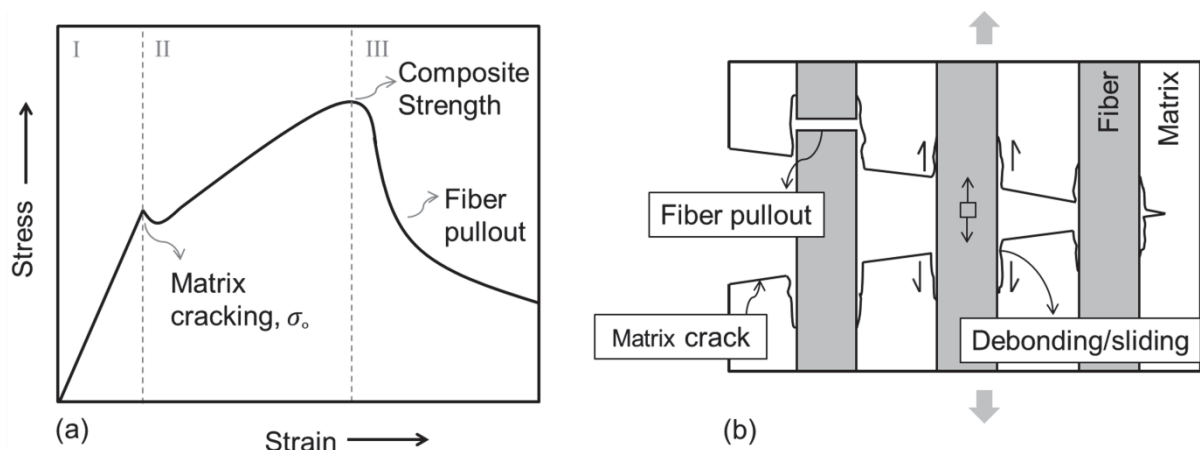


Figure 4: (a) Mechanical behavior of a damage tolerant, unidirectional CMC submitted to axial tensile loads; (b) schematic representation of toughening mechanisms present in CMCs. Adapted from Chawla [1] and Evans [22].

Figure 4(b) shows a schematic representation of these mechanisms. If the interfaces are well designed, the stress concentration in the presence of a transverse



matrix crack causes debonding at fiber-matrix interfaces (interfacial cracks parallel to the fiber axis), instead of fiber failure [33,44]. Stresses are then transferred from the matrix to the fibers, which thus bridge the matrix crack [33]. With further extension and opening of the transverse crack, interfacial cracks extend in the crack wake and stresses are transferred from the bridging fibers back to the matrix by friction, leading to the formation of new matrix cracks [1,22,33]. This process continues, and a periodic array of matrix cracks, parallel to each other and perpendicular to the fibers is formed [1,22,22]. Eventually, fibers will break in a statistical manner, following a Weibull distribution [22]. Region II is limited by the maximum attained stress σ_{c_u} , at which 15 to 30% of the fibers are broken [33]. Beyond this stress (region III), the composite is still capable of carrying reduced loads because of the remaining intact fibers, which now progressively fail and are pulled out of the matrix [1,33,43]. Fiber pullout requires additional load due to friction between fibers and matrix [23,45].

The failure mechanisms shown in Figure 4(b) contribute to the toughening of CMCs in different ways [22]: matrix cracking and debonding at fiber-matrix interfaces generate new surfaces which have an associated energy; frictional sliding during fiber pullout dissipates energy by local heating; elastic energy stored in the strained fibers is partially dissipated in the form of acoustic waves at fiber failure. As a result, much more energy is necessary to fracture a ceramic composite than a monolithic ceramic.

Nevertheless, it is common that not all these toughening mechanisms occur in a CMC. Usually, only one or two mechanisms dominate the failure of the composite and contribute to its toughness [1]. The stress-strain behavior presented in Figure 4(a) was observed in early developments of CMCs on glass or glass-ceramic matrix composites reinforced with C or SiC fibers [30,46]. However, the behavior of more recently developed fiber-reinforced CMCs usually differs from this one. For instance, the matrix cracking stress σ_c is usually not as marked as shown in Figure 4(a). Instead, there is a gradual decrease in the composite stiffness with an increasing load [33]. Additionally, the tail of the curve (region III) is normally not observed [33]. Figure 5 shows typical stress-strain curves of different long fiber reinforced CMCs tested under axial tensile loading.

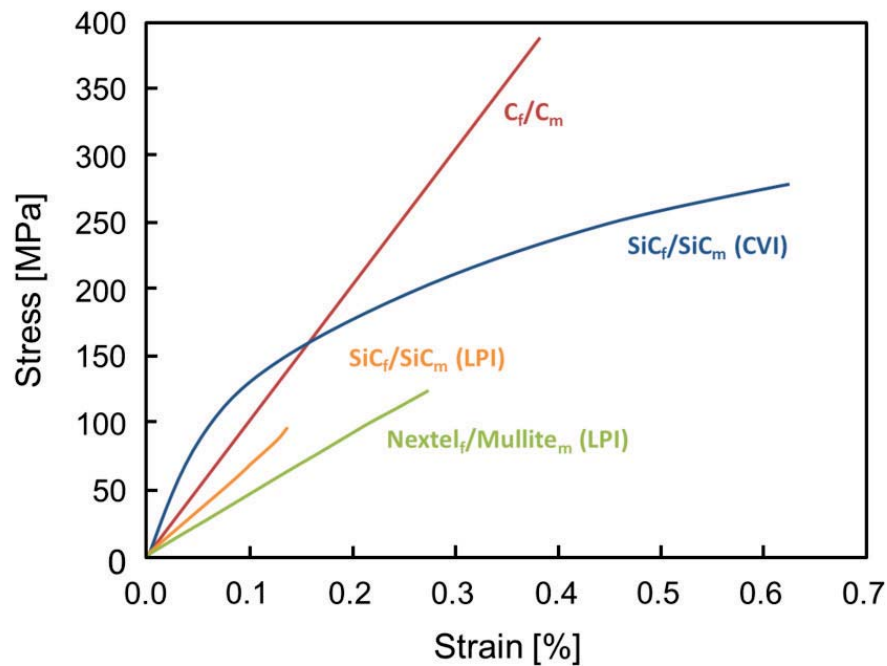


Figure 5: Representative stress-strain diagrams of different long fiber reinforced CMCs measured at room temperature under axial tensile loading. The indexes f and m stand for fiber and matrix, respectively. Adapted from Koch [33]. Copyright 2008 by Wiley-VCH Verlag GmbH & Co. KGaA. Reproduced with permission.

Analyzing these stress-strain curves, one could claim that bulk ceramics may be stronger than these CMCs. Bulk alumina (Al_2O_3), for instance, present strength values of up to ~ 500 MPa [47]; the strength of hot pressed silicon carbide (SiC) may achieve ~ 800 MPa [47] and yttria-stabilized zirconia may present strengths larger than 800 MPa [47]. However, it is important to note that, although ceramic fibers present higher strength values (~ 2 -4 GPa [48]) than these bulk ceramics, the contribution of fibers to the strength of a composite depends on its fiber volume fraction v_f , which usually varies from 0.35 to 0.45. In addition, only fibers oriented in the load direction contribute to the composite strength. For instance, in composites reinforced with two-directional woven fabrics and tested in the $0^\circ/90^\circ$ orientation, only half of the fibers contribute to the composite strength. Therefore, comparing the strength of composites with the strength of its constituting fibers may be misleading if the effective fiber volume fraction is not taken into account. Moreover, fibers may be damaged during composite processing, which results in strength degradation with regard to the strength of the as-received fibers. In addition, as mentioned previously, the interfaces of CMCs are usually designed to be very weak, so that fiber-matrix debonding occurs and the material presents a



damage tolerant behavior. These weak interfaces, however, do not favor load transfer between fibers and matrices, which detrimentally affects the strength of the composite.

The strong nonlinearity shown by the CVI $\text{SiC}_f/\text{SiC}_m$ composite is typical for WICs, in which the stiff matrix is strong enough to contribute to load sharing. Naslain and Lamon [2,34,49] showed that CVI $\text{SiC}_f/\text{SiC}_m$ with tailored interfaces that enhance load transfer without preventing crack deflection, present high strength and toughness, without showing extensive fiber pullout, although the latter is usually claimed to be indispensable for increasing toughness in CMCs.

In the case of WMCs such as C_f/C_m , porous oxide CMCs (e.g. Nextel¹/Mullite) and LPI $\text{SiC}_f/\text{SiC}_m$ (LPI stands for liquid precursor infiltration), the matrix is very weak and do not significantly contribute to the load carrying capacity of the composite [33]. Once the matrix breaks, the overall load is carried by the fibers and no load transfer from the fibers back to the matrix occurs anymore [33]. This leads to a linear elastic behavior up to composite failure [33]. In these materials, fiber failure does not occur locally and independently, but throughout large volumes of the material when the composite fails [33]. Nevertheless, damage tolerance can be detected in WMCs by acoustic signals emitted by the samples during failure [33] and by the observation of fiber pullout in the fracture surfaces [9].

Since the strength of WMCs strongly depends on the reinforcing fibers, their mechanical behavior significantly depends on the fiber orientation and load direction [33]. These materials are strong under axial loading (in fiber direction), but present much lower strength under off-axis loading (matrix dominated properties) [5,33]. This anisotropic behavior is clearly illustrated in Figure 6(a), which shows the stress-strain response of a porous matrix all-oxide composite under on-axis ($0^\circ/90^\circ$) and off-axis ($+45^\circ/-45^\circ$) loading [7]. On the other hand, the mechanical properties of stiff matrix CMCs (WICs) do not show a significant dependence on fiber orientation or load direction, as shown in Figure 6(b) [41].

¹ NextelTM is the commercial name of oxide fibers produced by 3MTM, as will be discussed in section 2.2.2.

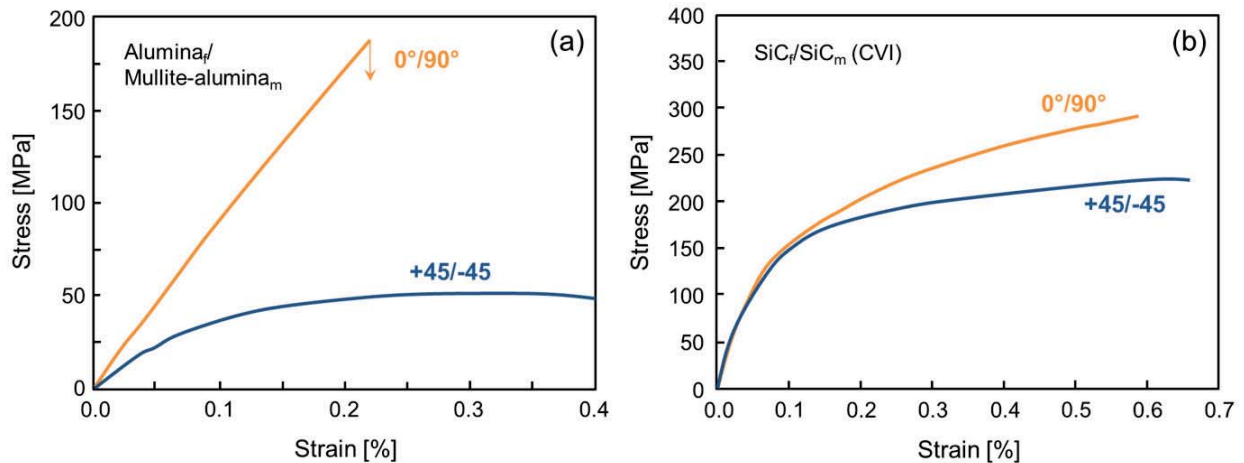


Figure 6: Representative stress-strain diagrams of CMC specimens tested under axial ($0^\circ/90^\circ$) and off-axis ($+45^\circ/-45^\circ$) tensile loading at room temperature: (a) all-oxide CMC with weak, porous matrix (WMC) and (b) CVI $\text{SiC}_f/\text{SiC}_m$ composite with stiff matrix (WIC). The indexes f and m stand for fiber and matrix, respectively. Figure (a) adapted from Zok and Levi [5]. Copyright 2001 by John Wiley and Sons, Inc. Reproduced with permission. Figure (b) adapted from Koch *et al.* [41]. Copyright 2008 by Elsevier. Reproduced with permission.

2.1.5 Laminar ceramics

Another way to profit from crack deflection to enhance the toughness of ceramic materials is to work with multilayered (laminar) ceramics, such as that shown in the inset of Figure 7. This was first reported by Clegg *et al.* [50], who showed that the fracture energy of these brittle materials can be significantly enhanced by introducing weak interfaces between dense, monolithic layers of ceramics. Since this concept is also based on crack deflection at weak interfaces between elastic materials, the He and Hutchinson diagram presented in Figure 3 can also be used to predict the crack deflection behavior [51].

When loaded, such layered ceramics undergo a layer-by-layer fracture, accompanied by a series of crack propagation/delamination events, which cause a *graceful* failure of the material, thereby avoiding a catastrophic fracture. Figure 7 shows a representative load-displacement curve of a laminar ceramic tested in bending, characterized by a stepwise reduction of the applied load after the first failure of the material.

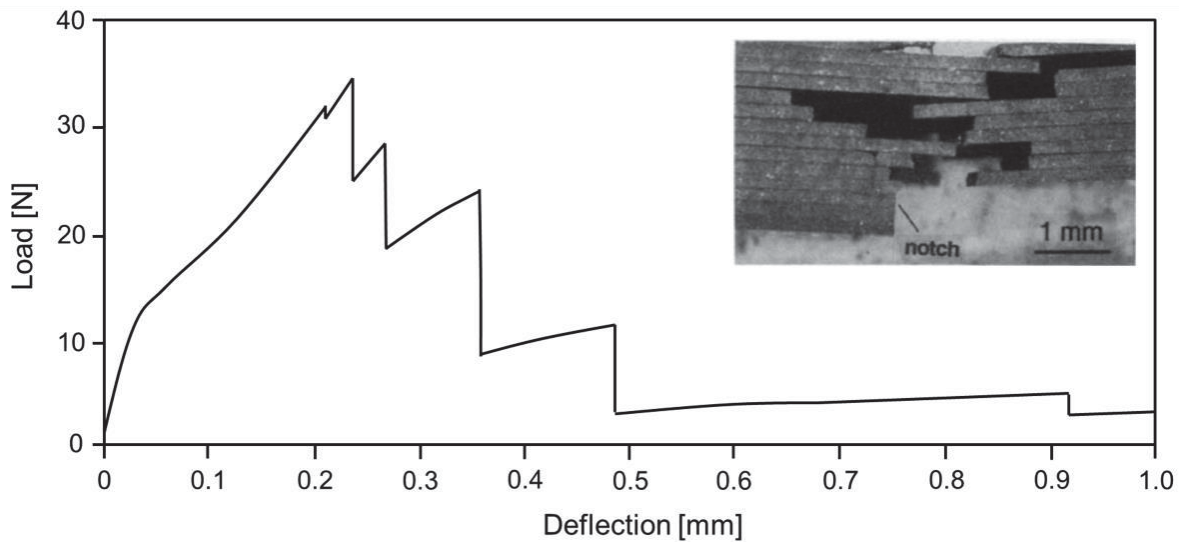


Figure 7: Load-deflection diagram of a multilayered ceramic composed of a stack of dense SiC plates coated with weak C interphases. The inset shows the fracture surface of a notched specimen tested in bending. The layer-by-layer failure leads to the stepped load-displacement curve. Adapted from Clegg *et al.* [50]. Copyright 1990 by Nature Publishing Group. Reproduced with permission.

2.2 All-oxide ceramic matrix composites

As briefly discussed in section 2.1.4, a stiff matrix can improve the mechanical properties of a CMC, mainly under off-axis loading (see Figure 6(b)). With regard to all-oxide composites, this is however not easy to achieve [23]. All-oxide CMCs are usually produced by liquid infiltration methods, where fiber textiles or bundles are impregnated with a liquid ceramic precursor or slurry of oxide particles, which are subsequently sintered for the consolidation of the matrix [3]. Therefore, there are basically two ways to consolidate a dense-matrix CMC [23]: (i) by sintering the composite at a high enough temperature to achieve reasonable densification and (ii) by several re-infiltration cycles followed by sintering at moderate temperatures. The first is limited by the microstructural instability of the currently available oxide fibers, which endure grain growth at the temperatures necessary for matrix densification (see section 2.2.2) [3]. The latter is very time-consuming and therefore prohibitively expensive in terms of processing technology. In addition, continuous fibers impose constraints to sintering, which inhibit matrix

densification [23]. As a result, the most common microstructural design for damage tolerance in all-oxide composites is the weak, porous matrix (Figure 2(d)). This is obtained either by pyrolysis of a ceramic precursor or by partially sintering the matrix particles at a low enough temperature not to damage the fibers [5]. Investigation on dense matrix oxide CMCs is still limited to the analysis of fiber-matrix debonding on model or mini-composites produced with just a few fibers dispersed in the matrix [3,19,52].

Porous matrix all-oxide CMCs were first developed in the mid-1990s [53,54], as a simple and inexpensive approach to produce damage tolerant, oxidation resistant CMCs, without the need of fiber coatings. Lange, Tu and Evans [53,54] demonstrated the effectiveness of this concept by showing the non-catastrophic failure of composites produced with alumina fibers reinforcing porous mullite or Si_3N_4 matrices. The failure characteristics of these CMCs were compared to that of wood. Since then, much research has been done on the development and understanding of porous matrix oxide composites. This section presents an overview about the progress in these materials over the past decades.

2.2.1 Implications of porous matrices for crack deflection

As discussed in sections 2.1.1 and 2.1.3, a minimum requirement for damage tolerance in CMCs is the arrest or deflection of matrix cracks at fiber-matrix interfaces. The conditions for crack deflection according to He and Hutchinson [40] are presented in Figure 3. For $\alpha > 0$, the ratio G_d/G_p can be approximated by the following empirical equation [9,42,55]:

$$\frac{G_d}{G_p} = \frac{1}{4(1 - \alpha)^{0.9}} \quad \text{Eq. 6}$$

According to Fugita *et al.* [42], Eq. 6 fits exactly the He and Hutchinson [40] criterion at $\alpha = 0$ and has an error of $\leq 4\%$ for the range $0 \leq \alpha \leq 0.95$.

Due to the absence of fiber coatings, the properties of the fiber-matrix interfaces in a porous matrix oxide composite can be assumed to be very similar to those of the matrix. However, the particle packing around fibers is not as efficient as in the bulk matrix [56], so that the following relationship applies:



$$\Gamma_i = \omega \Gamma_m \quad \text{Eq. 7}$$

where ω is a proportionality constant ≤ 1 and Γ_m is the toughness of the matrix. As discussed in section 2.1.3, for a given α , crack deflection is expected when $\Gamma_i/\Gamma_f < G_d/G_p$. By setting this condition in Eq. 6 and combining the result with Eq. 5 and Eq. 7, a nondimensional parameter for the prediction of crack deflection can be defined as follows [4,42]:

$$\Sigma \equiv 0.134 \left(\frac{\Gamma_f}{\Gamma_m} \right) \left(1 + \frac{E_f}{E_m} \right)^{0.9} > \omega \quad \text{Eq. 8}$$

In a conservative approach, Γ_i is assumed to be equal to Γ_m , so that $\omega = 1$. In this case, crack deflection is expected to occur when $\Sigma > 1$.

Therefore, by knowing the isolated properties of the fibers and matrix to be used in a specific composite, it is possible to predict if a damage tolerant behavior will be achieved or not. Additionally, by knowing how Γ_m and E_m relate to a given matrix parameter (e.g. porosity or composition), it is possible to modify Eq. 8 in order to estimate Σ as a function of one of these variables, which can be controlled during processing. For instance, Fugita *et al.* [57] predicted a critical value of alumina concentration for a mullite matrix strengthened by precursor-derived alumina, above which crack penetration into mullite fibers occurs, with a subsequent loss in damage tolerance [4,57]. In a similar approach, other authors estimated the minimum matrix porosity necessary for damage tolerance in oxide CMCs [9,55]. This approach is also used in this work for RBAO-matrix composites reinforced with polycrystalline alumina fibers, as will be presented in Chapter 3.

2.2.2 Oxide fibers

The most common oxide fibers used in CMCs are produced by 3M™ under the commercial name Nextel™. Among the different grades of Nextel™ fibers, Nextel™ 610 and Nextel™ 720 are the most commonly used for high temperature applications [3,4]. The properties of these fibers, as measured at room temperature, are summarized in Table 1, according to information provided by the supplier [58].

Table 1: Properties of Nextel™ oxide fibers measured at room temperature [58].

Fiber	Chemical Composition (wt %)	Diameter (μm)	CTE ($\text{ppm}/^\circ\text{C}$)	Tensile Strength (MPa)	Elastic Modulus (GPa)
Nextel™ 610	>99 Al_2O_3	10-12	8.0	3100	380
Nextel™ 720	85 Al_2O_3 15 SiO_2	10-12	6.0	2100	260

Nextel™ fibers are produced via a sol-gel technique and present a very fine microstructure, with grain sizes in the range of nanometers. Although this leads to high strength values at room temperature, it also results in microstructural instability and creep susceptibility at high temperatures [48]. Figure 8 shows the grain size and strength of both Nextel™ 610 and Nextel™ 720 as function of temperature [3]. At room temperature, Nextel™ 610 consists of ~ 80 nm alpha-alumina grains, while Nextel™ 720 consists of a bimodal grain size distribution of ~ 80 nm alumina and ~ 300 nm mullite grains [3]. For both fibers, grain coarsening starts at $\sim 1200^\circ\text{C}$, leading to a decrease in fiber strength. Although Nextel™ 610 presents a higher strength at room temperature, it undergoes a more pronounced temperature-induced strength deterioration than Nextel™ 720. This is a result of the ~ 4 orders of magnitude lower creep rate of Nextel™ 720 in relation to Nextel™ 610 [3], which can be attributed to the chemical composition and the large size of the mullite grains [3].

In summary, although advantageous in terms of oxidation resistance, fiber strength degradation and creep issues are limiting factors to the application of oxide CMCs at temperatures above 1100°C - 1200°C .

2.2.3 Oxide matrices and processing of all-oxide CMCs

While fiber microstructural stability is important for the composite strength, the stability of matrix porosity dictates the retention of damage tolerance when all-oxide CMCs are applied at high temperatures [23]. As indicated in Figure 3, matrix densification during service leads to a decrease in the elastic mismatch between

fibers and matrix, and may induce the brittle failure of the composite if no low toughness fiber coating is used.

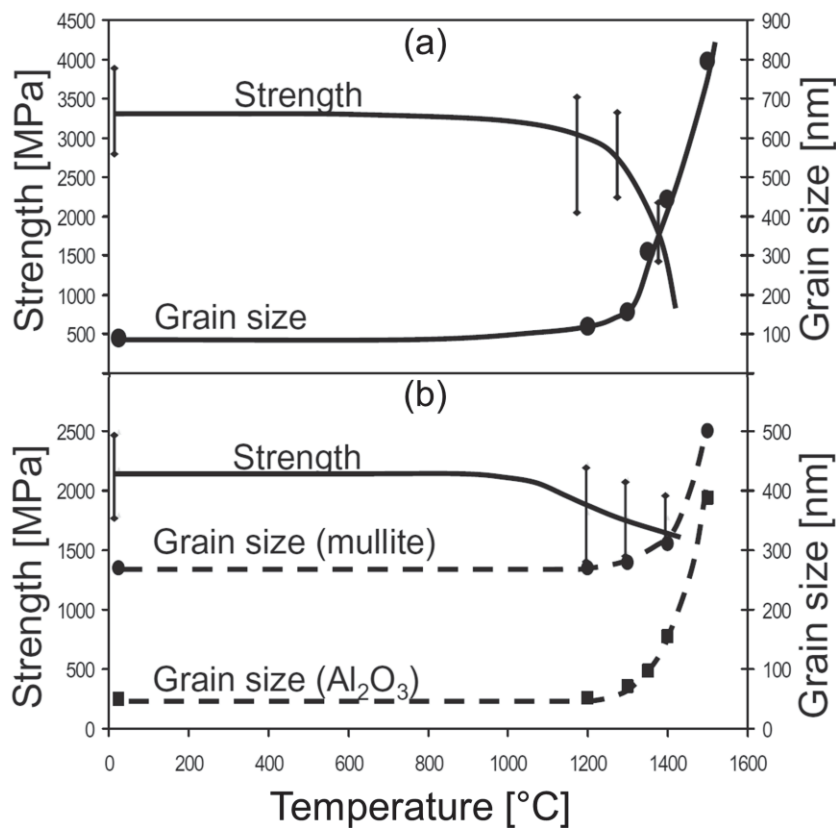


Figure 8: Strength and grain size of (a) Nextel™ 610 and (b) Nextel™ 720 measured at room temperature and after isothermal firing for 1 h at different temperatures. Adapted from Schmücker and Mechnich [3]. Copyright 2008 by Wiley-VCH Verlag GmbH & Co. KGaA. Reproduced with permission.

Other concerns related to the weak, porous matrices are their permeability, low thermal conductivity, poor wear resistance and low compression and interlaminar properties [3,4,23]. These problems are further intensified by the presence of matrix cracks and defects formed during processing, due to the constrained shrinkage imposed by the rigid fiber network during drying or sintering [7,12,13]. Designing an effective porous matrix is therefore very challenging. In terms of mechanical properties, it must be weak enough to ensure damage tolerance, yet sufficiently strong to give good off-axis properties [5]. Additionally, it should withstand high temperatures without enduring considerable microstructural changes [4].

Different approaches have been proposed to enhance matrix stability at high temperatures. The most common is the use of a bimodal grain distribution, in

which large oxide particles form a contiguous network, bonded together by smaller and more sinterable particles, as shown in Figure 9 for a mullite-alumina particle network. While the large grains give long-term stability against sintering, the smaller ones give mechanical strength and integrity to the matrix [4].

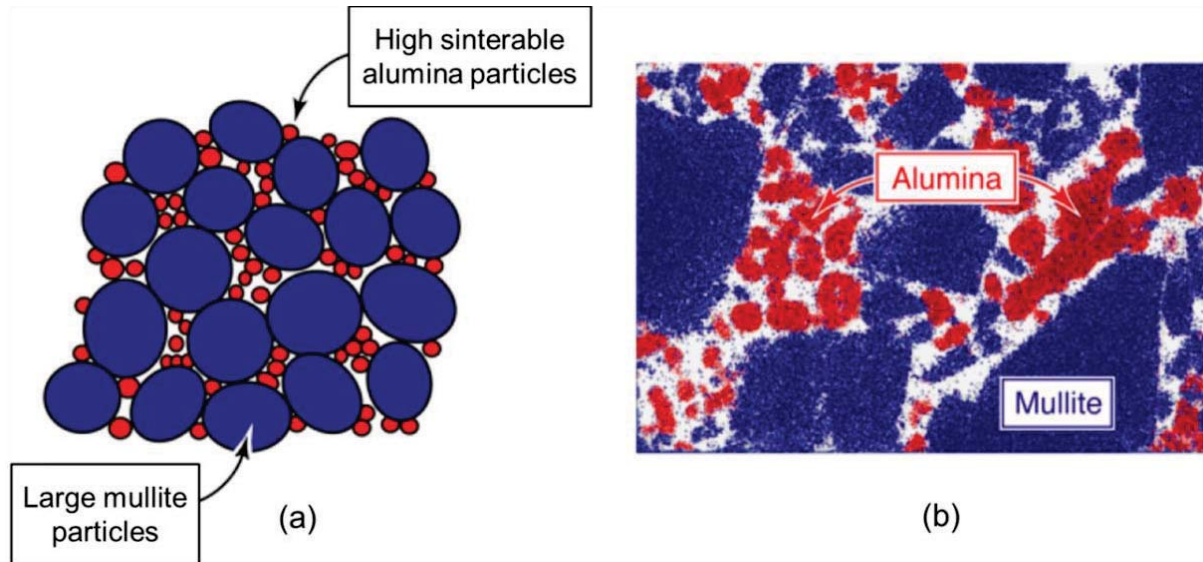


Figure 9: Bimodal matrix distribution for high temperature stability: (a) schematic of a matrix topology consisting of large mullite grains bonded together by small alumina particles; (b) Compositional map of a mullite-alumina matrix, obtained by energy-dispersive spectroscopy of transmission electron microscope foils. Adapted from Zok [4]. Copyright 2006 by John Wiley and Sons, Inc. Reproduced with permission.

This concept was first presented by Levi *et al.* [7]. In their study, the contiguous network was formed by mullite particles ($\sim 1 \mu\text{m}$) and submicron alumina particles ($\sim 200 \text{ nm}$) were used as a binder. The latter start sintering at about 800°C . Mullite was selected because of its sluggish sintering kinetics up to $\sim 1300^\circ\text{C}$, which further enhances microstructural stability. In their processing [7], a stack of Nextel™ (610 or 720) woven fabrics (fiber preform) is infiltrated with an aqueous slurry of the mullite and alumina particles, under the assistance of vacuum. After drying, a pre-sintering treatment is performed at 900°C , for the bonding of the matrix network. In order to strengthen the matrix, the composite is re-infiltrated with an alumina precursor solution, which is pyrolyzed at 900°C . After a series of re-infiltration and pyrolysis cycles, the composite is sintered at 1200°C for 2 h. In-plane tensile tests were performed in these composites and a fibrous failure was observed, even when the specimens were previously exposed to 1200°C for 100 h. This indicates the stability of the matrix, at least under these temperature and time



conditions. Further investigation on the effects of thermal ageing on these oxide CMCs over longer-term exposure was performed by Carelli *et al.* [59] and will be discussed in section 2.2.4.

The stability of this mullite-alumina matrix system was investigated in more detail by Fugita *et al.* [42,57]. Results showed that samples containing ≤ 20 vol% alumina do not present significant shrinkage or porosity changes ($< 0.5\%$) after 1000 h exposure at 1200°C . Additionally, the densification process in samples containing 30 vol% alumina after 1000 h at 1200°C is very slow, so that porosity decreases less than 3%. Nevertheless, for larger alumina contents, shrinkage starts after an exposure of about 100 h to 1200°C . This confirms the effectiveness of the large mullite particles in hindering matrix densification.

Further advancing on porous matrix CMCs was obtained by Simon [6]. His approach is also based on a bimodal grain distribution, but both large and small particles are composed of mullite. In this approach, fiber textiles are impregnated with a low viscous slurry of particle agglomerates presenting a core-shell structure. In an ideal case, the large mullite particles ($\sim 1 \mu\text{m}$) are fully covered by the highly sinteractive mullite nanoparticles ($< 100 \text{ nm}$). After impregnation, fabric layers are laid up by hand and joined by a vacuum bagging technique. Following this step, matrix setting occurs via an *in situ* reaction that slowly changes the pH of the suspension to a value which causes particle coagulation (isoelectric point). This reaction is caused by the presence of a time-delayed setting agent (AlN powder), added to the colloidal suspension in the beginning of the process. Coagulation leads to the formation of a homogeneous, stiff particle network, with well-distributed fine-scale porosity. Final sintering is performed at temperatures $> 1200^\circ\text{C}$ and no reinfiltration cycles are needed to strengthen the matrix. Figure 10 shows the microstructure of a composite produced by this route [6]. The homogeneous distribution of fibers in this microstructure resulted in very good mechanical properties, as will be presented in section 2.2.4.

Figure 10 also evidences the problem of matrix cracks formation during processing. Such cracks may not only be detrimental to the composite mechanical properties [8–10], but also have a negative effect on the thermal conductivity and, consequently, on the thermal shock resistance of the material [11,12]. It is,

therefore, of great interest to mitigate the formation of these cracks. For this purpose, matrix shrinkage must be avoided both during drying and sintering.

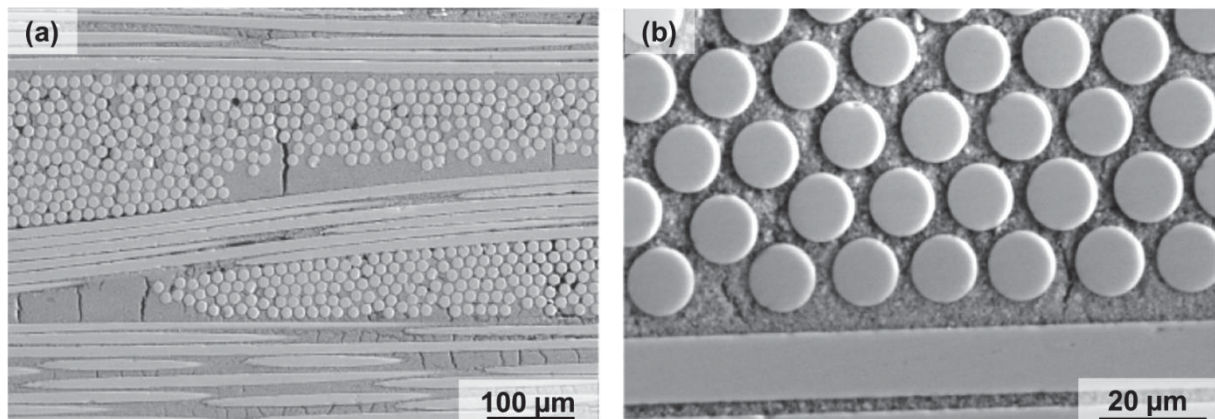


Figure 10: Microstructure of an all-oxide CMC composed of an all-mullite matrix reinforced by Nextel™ 720 woven fabrics [6]. This material was produced by the colloidal route reported by Simon [6]. Copyright 2005 by John Wiley and Sons, Inc. Reproduced with permission.

A few approaches have been proposed to avoid the formation of drying-related cracks. As can be seen in Figure 10, these flaws are usually concentrated in matrix-rich regions [6,7,59]. Hence, in order to mitigate the formation of these cracks, Levi *et al.* [7] suggested the filling of the large cross-over regions of the fiber fabrics with chopped fibers. This was done by coating the fiber cloths with a paste of short fibers before slurry infiltration of the preform. This approach alleviated the formation of matrix cracks, but there was an associated decrease in the packing efficiency and fiber volume content, which may be detrimental to the mechanical properties of the material. The same principal was investigated years later by Yang *et al.* [13], but instead of short fibers, large SiC particles were used. In their work, a fiber preform was infiltrated with a slurry containing small mullite and alumina matrix particles (1 μm and 0.2 μm, respectively) for impregnation within the fiber tows, as well as large SiC particles (>10 μm) to fill the large spaces between the fiber tows [13]. This approach showed to be effective in diminishing the drying cracks, besides bringing advantages in terms of thermal diffusivity of the composite [13]. However, SiC particles are susceptible to oxidation, so more investigation is needed to prove the effectiveness of this approach when pure oxide particles are used.

In order to mitigate sintering-related cracks, reactive sintering routes, which allow the tailoring of the matrix sintering shrinkage to zero, have been often proposed



[1,3,45,60]. Nevertheless, this approach has not yet been tested in full-scale, all-oxide composites. Research in this area is still limited to the analysis of model samples containing only a few fibers dispersed in a matrix [18,19]. The use of a reactive sintering route for the consolidation of crack-free composites is one of the objectives of this work. More information on the subject will be given in section 2.3.

Recent progress in the development of matrix systems for oxide CMCs has been reported by Rüdinger and Pritzkow [8]. They have investigated different matrix systems over the past decade, including mullite-mullite, mullite-alumina and alumina-alumina. However, the best microstructure and mechanical properties were obtained by using a mixture of large alumina particles bonded together by high sinterable zirconia nanoparticles. According to Rüdinger and Pritzkow [8], alumina and zirconia are more resistant than mullite to high temperature corrosion in water vapor or oxygen containing atmospheres. By using this alumina-zirconia system, composites can be produced via aqueous slurry infiltration, without the assistance of vacuum, or the need of organic precursors or reinfiltration cycles to strengthen the matrix [8]. Additionally, the authors reported that matrix compositions containing 15 to 30 wt% ZrO_2 present virtually no shrinkage when sintered at $1200^\circ C$, which helps reducing the formation of shrinkage-related matrix cracks. High in-plane and off-axis strength values were obtained for Nextel™ 610 reinforced composites produced with this matrix system (see Table 2). However, no data of strength retention after high temperature exposure was presented.

Extensive research activities on all-oxide composites are also performed by the German Aerospace Center (DLR) [3,61]. In contrast to the processing routes presented previously, composites are manufactured via filament winding and are therefore called Wound Highly Porous Oxide CMCs (WHIPOX™) [3]. In this process, fiber tows are infiltrated with an aqueous slurry of the matrix particles and subsequently wound on a mandrel. Fiber orientation can be controlled by adjusting the fiber winding angle. Axisymmetric components can be directly produced by selecting the appropriate geometry of the mandrel. Otherwise, composite laminates can be produced by stacking prepregs cut from the wound green bodies in the moist state. Composites are sintered at $\sim 1300^\circ C$, with no subsequent reinfiltration cycle for the strengthening of the matrix [3].



The most common matrix system used by DLR is alumina, with up to 30 wt% silica [3]. In contrast to the other matrix systems presented previously, this alumina-silica matrix is not bimodal. Instead, matrix particles present a uniform size distribution and are submitted to a special pre-treatment to increase sinterability at the temperatures necessary for the composite production [3]. WHIPOX™ composites present a wide range of mechanical properties, depending on the winding pattern, matrix composition and fiber type, as reported elsewhere [3] and summarized in Table 2.

Apart from the significant development shown in this section concerning the processing of all-oxide CMCs, significant research is still going on in order to optimize material properties and manufacturing routes of these materials [8,62–64]. Much attention is given to the development of low cost and reliable techniques suitable for series production. Additionally, routes that enable the manufacturing of large, as well as complex-shaped CMC components should be developed, including new concepts for the reliable joining and assembling of CMC structures [65,66].

2.2.4 Mechanical properties of all-oxide CMCs

Porous matrix oxide composites present a very anisotropic mechanical behavior, as shown in Figure 6(a). Depending on the test configuration and direction of applied load in relation to the fibers, the mechanical response can be dominated either by the fibers or by the matrix [3]. Furthermore, processing parameters, matrix composition and porosity, as well as fiber content, type and orientation (unidirectional or woven fabric) strongly influence the mechanical properties of the material, which makes it difficult to compare values published by different authors [3]. In any case, the composition and mechanical properties of the different all-oxide CMCs discussed in the present and previous sections are summarized in Table 2.



Table 2: Properties of different all-oxide CMCs. All the mechanical data presented was obtained at room temperature.

Properties	Levi <i>et al.</i> [7]	Carelli <i>et al.</i> [59]	Mattoni <i>et al.</i> ¹ [9]	Simon [6]	DLR (WHIPOX™) [3]	W.E.C. Pritzkow (Keramiklech®) ³ [8]
Matrix Composition	Mullite/Alumina					
Fiber Type	N610 (WF)	N720 (WF)	N720 (WF)	N610 (WF)	N610 (FL) and N720 (FL)	N610 (WF)
Fiber Configuration	0°/90°	0°/90°	0°/90°	0°/90°	Various ²	0°/90°
Fiber Content (vol%)	33-39	~39	-	~48	25-50	-
In-Plane Strength (MPa)	>200 ^(t)	~145 ^(t)	~220 ^(b)	290-310 ^(t)	55-120 ^(t)	~350 ^(b)
ILSS (MPa)	8-10 ^(sb)	-	~10 ^(sb)	12.5-14 ^(sb)	5-30 MPa	>20 ^(sb)
Elastic Modulus (GPa)	~100 ^(t)	~60 ^(t)	-	104-110 ^(t)	40-200 ^(t)	92 ^(b)
Strain at Fracture (%)	~0.27 ^(t)	~0.26 ^(t)	-	0.25 - 0.32 ^(t)	-	>0.3

N610: Nextel™ 610; N720: Nextel™ 720; WF: Woven Fabric (2-dimensional, 8-harness satin); FL: Filament tensile; ^{sb} short beam shear; ^b bending

¹Results shown for a material produced with 2 precursor reinfiltration cycles (matrix porosity of ~35%)

²Depending on the winding pattern

³Keramiklech® FW12/FW30

For design purposes, preference is given to tensile tests, if in-plane composite strength is to be determined. However, in real applications, composites are submitted to different kinds of loading, what makes it important to characterize the material under different load conditions. Although high strength is usually obtained in the fiber direction, interlaminar failure due to the low strength of matrix and interfaces is still a limiting design issue for all-oxide composites with porous matrices [23].

Under axial tensile loading, all-oxide CMCs normally show a linear elastic stress-strain behavior up to failure, as shown in Figure 6(a). To the author's knowledge, the only report on all-oxide composites presenting a well-developed quasi-ductile behavior under tension was published by Simon [6,67], who also reported the highest tensile strength values obtained for these kind of materials. A comparison between the stress-strain curves published by Simon [6] and those reported by Levi *et al.* [7] and Carelli *et al.* [59] for another family of oxide composites is shown in Figure 11.

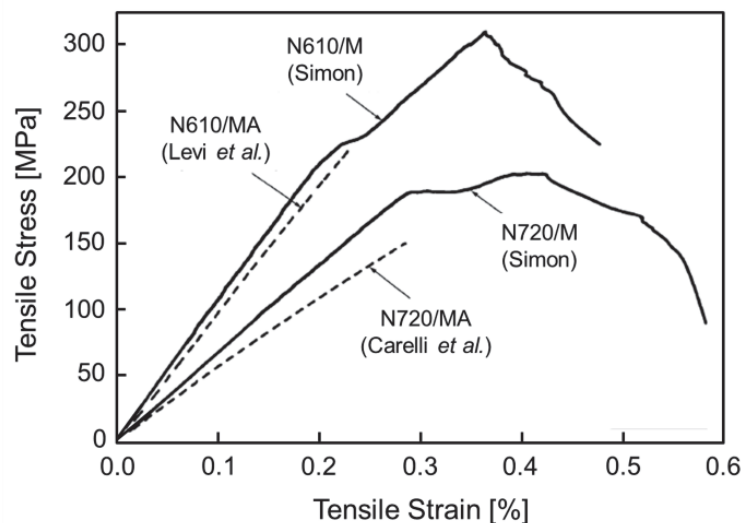


Figure 11: Stress-strain curves obtained by axial tensile tests on all-oxide CMCs ($0^\circ/90^\circ$) produced by Simon [6], Levi *et al.* [7] and Carelli *et al.* [59]. All measurements were performed at room temperature. N610 or N720 refer to the Nextel™ fiber used. M and MA stand for mullite and mullite-alumina matrix, respectively. Adapted from Simon [6]. Copyright 2005 by John Wiley and Sons, Inc. Reproduced with permission.

The materials presented in Figure 11 differ in their processing routes and matrix compositions. As briefly presented in section 2.2.3, Simon [6] uses a bimodal mullite grain distribution in his colloidal route. Levi *et al.* [7] and Carelli *et al.* [59]



work with a bimodal mullite-alumina matrix (see Figure 9), strengthened by a precursor-derived alumina. All composites shown in Figure 11 were produced with fiber woven fabrics in a $0^\circ/90^\circ$ configuration. The higher strength and elastic modulus of composites produced with Nextel™ 610 are due to the better mechanical properties of these fibers at room temperature, in relation to the mullite-containing Nextel™ 720 (see Table 1).

Fracture surfaces of representative samples from Simon [6] and Carelli *et al.* [59] are shown in Figure 12. It can be seen that samples produced by Simon [6] present a more fibrous fracture surface (Figure 12(a)) than those produced by Carelli *et al.* [59] (Figure 12(b)). According to Simon [6], fracture mechanisms associated with the quasi-ductile behavior of his samples involve crack deflection at fiber-matrix interfaces, uncorrelated fiber fracture within fiber bundles, uncorrelated bundle fracture and shear-induced delamination on matrix regions between layers of the reinforcing fabric. It is believed that the superior mechanical results obtained for his samples are a consequence of the fine-grained and homogeneous microstructures achieved with his colloidal processing route (see Figure 10) [6,33].

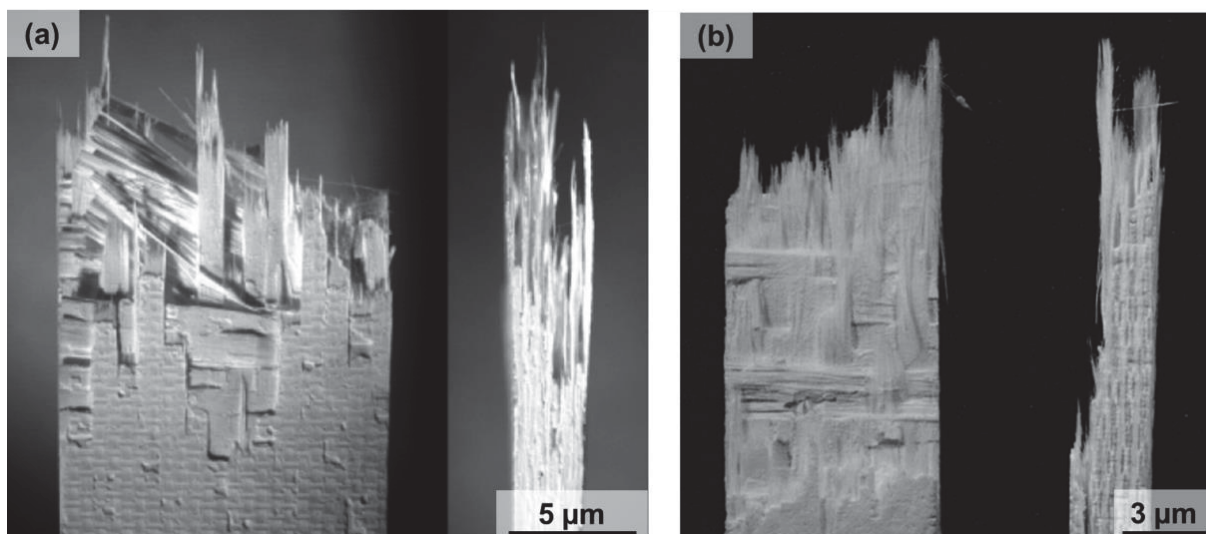


Figure 12: Fracture surfaces of all-oxide CMCs tested in axial tensile loading ($0^\circ/90^\circ$) at room temperature: (a) composite produced by Simon [6], consisting of an all-mullite matrix and Nextel™ 720 fibers; (b) composite produced by Carelli *et al.* [59], consisting of a mullite-alumina matrix reinforced by Nextel™ 720 fibers. Figure (a) adapted from Simon [6] and figure (b) adapted from Carelli *et al.* [59]. Copyright of both pictures by John Wiley and Sons, Inc. Both pictures reproduced with permission.

In order to assess the high temperature microstructural stability of all-oxide CMCs, Carelli *et al.* [59] and Simon [6] also investigated the strength retention of their

composites after 1000 h exposure to temperatures varying between 1000°C and 1300°C. Results are shown in Figure 13(a). All composites are reinforced with Nextel™ 720 woven fabric in a 0°/90° configuration. As an indication of the extent of matrix sintering, the variation of composite Young's moduli after the ageing treatments was also investigated. Results are shown in Figure 13(b).

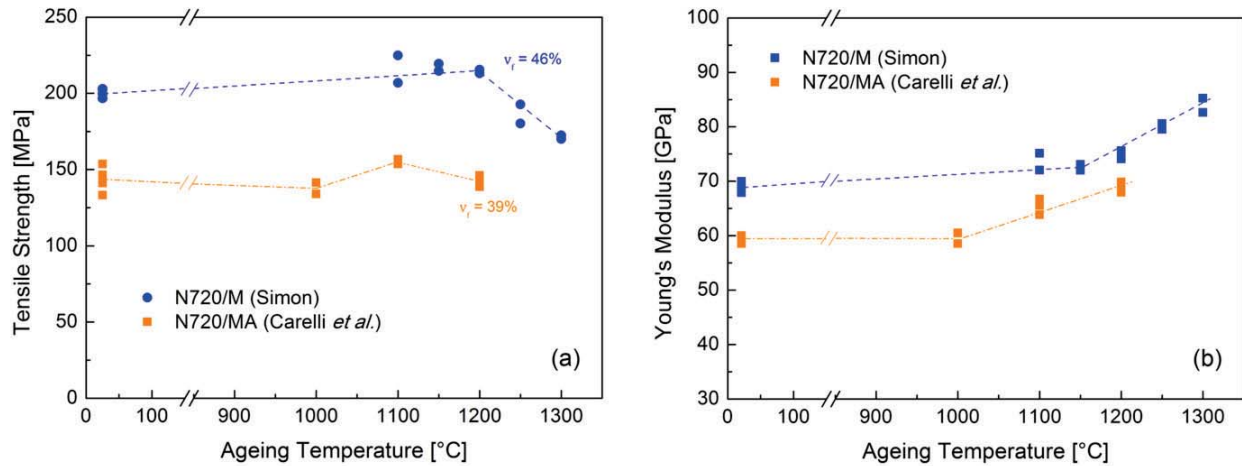


Figure 13: Effect of ageing on the mechanical properties of different all-oxide CMCs: (a) retained tensile strength after 1000 h ageing at different temperatures; (b) Young's modulus after 1000 h ageing at different temperatures. N720 refer to the Nextel™ 720 fiber. M and MA stand for mullite and mullite-alumina matrix, respectively. Adapted from Simon [6] and Carelli *et al.* [59].

As it can be seen, both composite systems present strength retention up to 1200°C. This indicates that the bimodal matrix approach discussed in section 2.2.3 is effective on enhancing the stability of matrix porosity at high temperatures. Nevertheless, the mullite-alumina matrix used by Carelli *et al.* [59] starts to densify at about 1000°C, as indicated by the increase in elastic modulus (Figure 13(b)). The associated decrease in matrix porosity and the subsequent strengthening of interfaces lead to a reduction in the damage tolerance of the composites [59]. A better performance is presented by the all-mullite system used by Simon [6]. Apart from the higher strength values obtained over the temperature range investigated, a significant densification of the all-mullite matrix starts only at 1200°C (Figure 13(b)). This confirms the superior stability of this matrix, in comparison to the mullite-alumina composition. Beyond 1200°C, the retained strength of the all-mullite composites reduce gently, due to matrix densification and grain coarsening of the Nextel™ 720 fibers [6].



Matrix porosity can also be controlled during processing by, for instance, varying the number of matrix precursor reinfiltration cycles. This was investigated by Mattoni *et al.* [9] in order to analyze the influence of matrix porosity on the mechanical properties of a family of all-oxide CMCs. Composites were produced with Nextel™ 720 woven fabric and a bimodal mullite-alumina matrix, following the processing route developed by Levi *et al.* [7] (see section 2.2.3). After a first heat treatment at 900°C for the pre-sintering of the matrix, composites were submitted to an increasing number of reinfiltration cycles, varying from 2 to 10. After each cycle, the precursor was pyrolyzed at 900°C. Final sintering was performed at 1200°C. By this approach, composites containing about 29% to 35% matrix porosity could be produced. Figure 14 shows the mechanical behavior obtained by in-plane flexural tests performed on these composites [9].

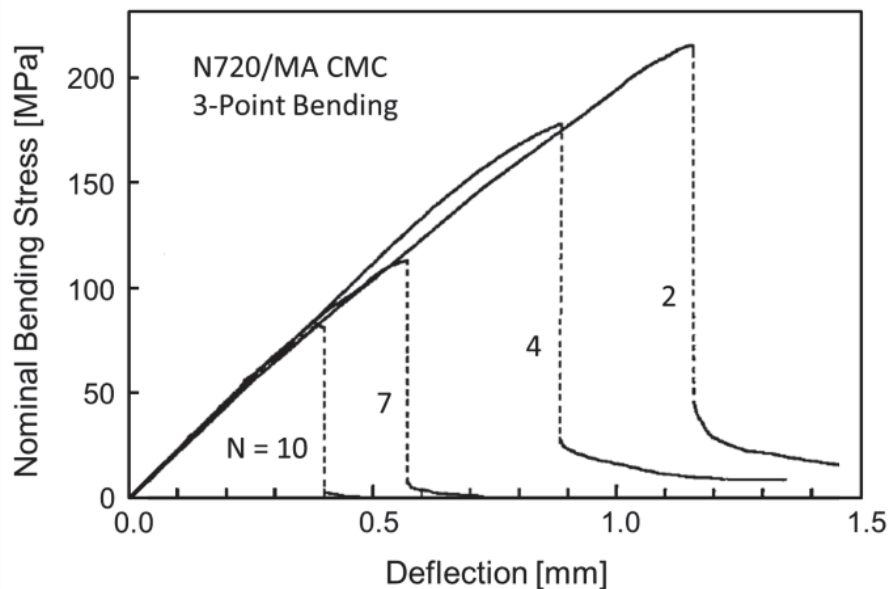


Figure 14: Effect of matrix porosity on the mechanical properties of all-oxide CMCs composed of a mullite-alumina matrix (MA) reinforced by Nextel™ 720 fibers (N720). Porosity was varied by changing the number of precursor reinfiltration cycles (N). Adapted from Mattoni *et al.* [9]. Copyright 2004 by John Wiley and Sons, Inc. Reproduced with permission.

As observed by Mattoni *et al.* [9], the decrease in matrix porosity leads to a decrease in the mechanical strength. This trend is accompanied by a decrease in the amount and length of fiber pullout, as it can be seen on the fracture surfaces shown in Figure 15 [9].

According to Zok and Levi [5], highly porous matrices deform inelastically by mechanisms such as fracture of necks between particles and particle

rearrangement. This decreases stress concentration around broken fibers and favors a stochastic, random fiber failure (uncorrelated fiber fracture). In this case, extensive fiber pullout is observed in the fracture surface, as shown in Figure 15(a) [9], and higher composite strength values are achieved due to the enhanced fiber strength utilization in the composite [5,9]. On the other hand, denser matrices lead to a more localized load sharing behavior, which reduces the composite strength and toughness [9]. In the absence of weak fiber coatings, the high stress concentration around broken fibers induces the fracture of adjacent fibers, leading to correlated fiber failure and planar fracture surface as shown in Figure 15(c) [9].

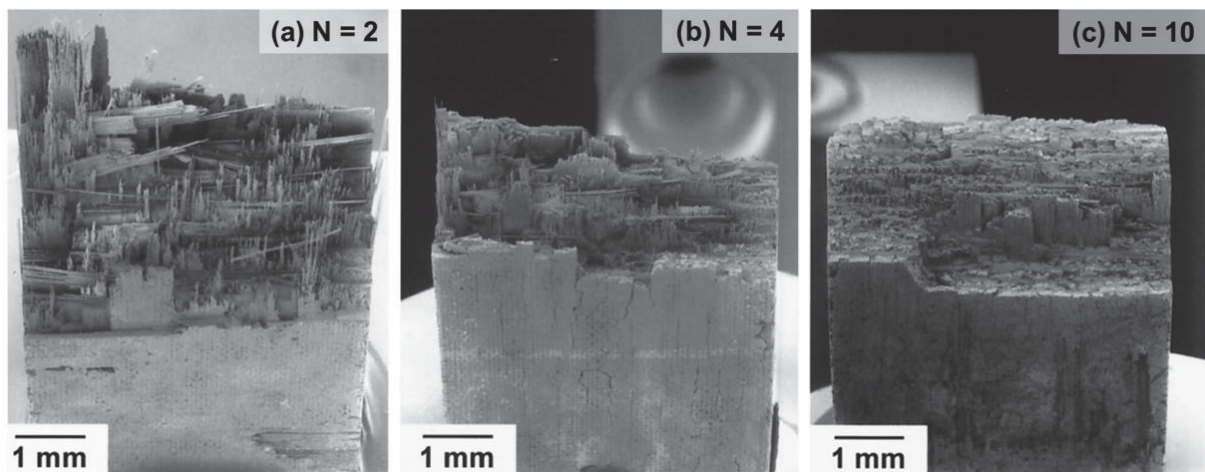


Figure 15: Fracture surfaces of all-oxide CMCs containing different values of matrix porosity. N stands for the number of precursor reinfiltration cycles. Adapted from Mattoni *et al.* [9]. Copyright 2004 by John Wiley and Sons, Inc. Reproduced with permission.

Similar to Mattoni *et al.* [9], many researchers prefer the use of flexural tests to assess the properties of ceramic composites because of the easiness of sample preparation and testing. These tests are generally used for material development and are suitable for comparison between similar samples. However, care should be taken when selecting specimen dimensions, so that the desired mechanical properties (on-axis or off-axis) are measured. Depending on the sample thickness h in relation to the load span S , specimens may fail under tension/compression or by interlaminar shear. Large S/h ratios are recommended if the fiber-dominated properties are to be measured, whereas small S/h ratios favor interlaminar failure. This can be better understood by analyzing the governing equations in a flexure test [1]: in 3-point bending, for instance, the maximum flexural stress occurs at the outermost surface of the sample and is given by:



$$\sigma_{3PB} = \frac{3LS}{2bh^2} \quad \text{Eq. 9}$$

where L is the applied load and b is the sample width. In the same test configuration, the maximum shear stress τ occurs in the mid-plane of the sample and is given by:

$$\tau_{3PB} = \frac{3L}{4bh} \quad \text{Eq. 10}$$

Dividing Eq. 10 by Eq. 9, one obtains:

$$\frac{\tau_b}{\sigma_b} = \frac{h}{2S} \quad \text{Eq. 11}$$

Eq. 11 indicates that, for the same sample thickness h , a reduction in the load span S causes the sample to endure higher shear stresses, which can cause interlaminar failure, provided the composite interlaminar shear strength is achieved before the material breaks under tension or compression [1]. This is very common in ceramic matrix composites, because of their high mechanical anisotropy, as discussed in section 2.1.4. In fact, short beam shear (SBS) tests are often performed to assess the interlaminar shear strength (ILSS) of CMCs [7–9,67]. In this case, S is selected so that sample failure is dominated by an interlaminar crack that propagates in the specimen midplane. ILSS is then calculated by Eq. 10 [68]. Likewise, large load spans should be selected for the assessment of strength in the fiber direction, which can be calculated by Eq. 9 [69].

2.3 Reaction Bonded Aluminum Oxide

The RBAO process was developed by Claussen *et al.* [15] in the late 1980s, as an alternative to the conventional processing of alumina ceramics. The motivation was to overcome typical processing problems associated with large shrinkages, such as shape distortion and cracking [15,70]. RBAO ceramics present low shrinkages due to the oxidation of Al particles present in the precursor powder during heat treatments in air. The expansion associated with this oxidation (28 vol%) may partially or totally compensate for the shrinkage at a given sintering temperature, depending on the Al amount in the powder and on the green density of the sample [71]. Advantages of the low shrinkages include the production of

near net shape ceramic components, as well as the easy incorporation of non-yielding second phases, such as fibers and platelets, without the creation of harmful residual stresses [15,71].

2.3.1 RBAO process

RBAO precursor powders are usually composed of a mixture of Al and Al₂O₃. Normally, Y₂O₃-stabilized ZrO₂ (YSZ) is also added to this mixture in order to enhance the oxidation process, as well as to improve microstructure and mechanical properties of the sintered materials [71,72]. Zirconia hinders the grain growth of alumina and is fundamental for obtaining fine-grained and homogeneous microstructures [16]. This results not just in high strength values, but also in superplastic deformation at high temperatures [73].

RBAO powder mixtures are normally intensively milled for particle comminution and homogenization. This enables the use of coarse grained Al and oxide starting powders, which leads to a reduction in the raw material costs [72]. Milling must be performed in an organic medium, usually ethanol or acetone, since aluminum readily reacts with water to form oxides and hydroxides. Nevertheless, due to the high solubility of water in these polar liquids, moisture is inevitably absorbed from the atmosphere, leading to the formation of these reaction products on the surfaces of the freshly milled Al particles [74]. Up to 60% of aluminum can react during milling [16], decreasing the effective Al amount available for shrinkage compensation during sintering [73]. Additionally, these hydroxides decompose upon heating and may cause defects such as entrapped pores and bloating, if the outer surfaces of the RBAO sample densify prior to the complete hydroxide decomposition [16,72].

Figure 16 shows the result of a simultaneous thermal analysis of an RBAO powder compact consisting of a mixture of Al and Al₂O₃. The upper diagram shows the results of thermogravimetry (TG) and differential thermal analysis (DTA). The lower diagram presents the associated evolution of chemical species, detected simultaneously by mass spectroscopy. The weight loss up to ~380°C is due to the evaporation of H₂O, H₂ and C_xH_y species, as indicated by mass spectroscopy. The evaporation of C_xH_y results from desorption of molecules adsorbed from the milling liquid, whereas the evaporation of H₂O and H₂ results from the desorption

of physically adsorbed water, as well as from the decomposition of aluminum hydroxides [16]. The presence of hydroxides and adsorbed species is beneficial to the passivation and safe handling of the RBAO powder prior to sintering [72]. The problems associated with their evaporation, such as pores and bloating can be circumvented using slow heating rates ($\leq 1^\circ\text{C}/\text{min}$).

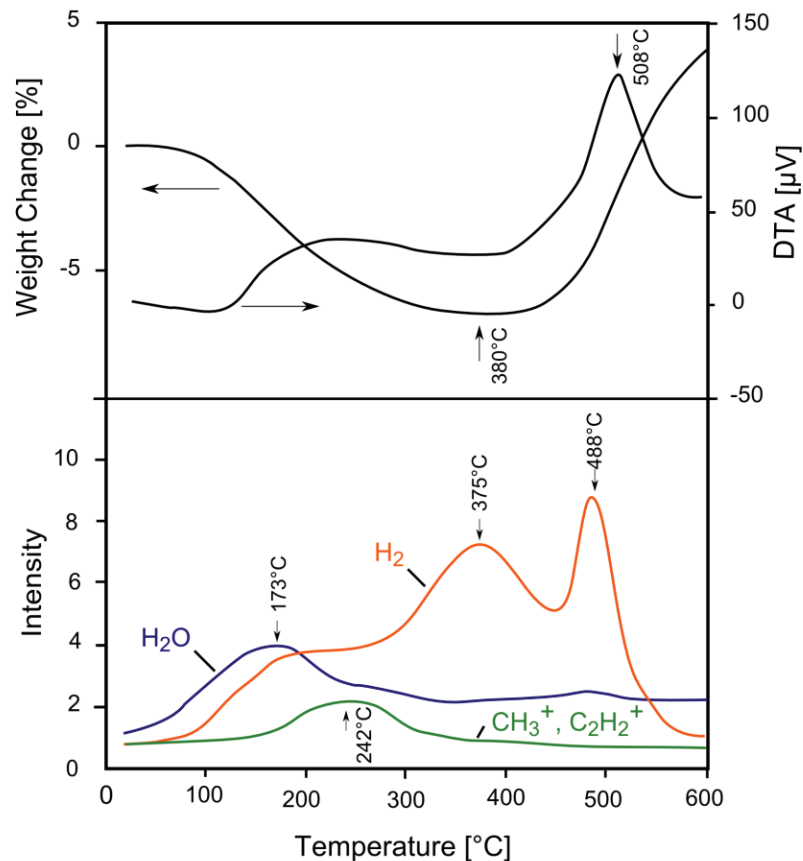


Figure 16: Simultaneous thermal analysis of an RBAO powder composed of Al and Al₂O₃. The upper diagram shows the results of TG/DTA. The lower diagram presents the corresponding mass spectroscopy data. Adapted from Holz [75].

The effective milling of Al particles is fundamental for a successful RBAO process. During heat treatment, oxidation of aluminum occurs both by solid/gas and liquid/gas reactions. The first occurs at temperatures below the melting point of aluminum (660°C) and the latter, above it. Figure 16 shows that oxidation starts at $\sim 380^\circ\text{C}$ (characterized by a gain in weight) and has a maximum solid/gas reaction rate at $\sim 508^\circ\text{C}$. Claussen *et al.* [73] suggested that there is a critical particle size ($\sim 1\ \mu\text{m}$), below which oxidation occurs completely by solid/gas reaction. The latter is advantageous, since melting of large aluminum particles leads to microstructural defects such as voids and cracks, formed due to the outward flow of the molten aluminum through the open pore system [15,16,76].



2.3.2 RBAO conformation techniques

After milling and drying, RBAO precursor powders can be shaped by any powder metallurgy conformation route. Cold isostatic pressed (CIP) RBAO green bodies present high densities (>60 %TD) and mechanical strengths (up to 70 MPa), because of the strong Al/Al contact bridges formed due to plastic deformation of the Al particles [70,72]. This enables easy green machining, which associated with the low sintering shrinkages enhances the near net shape capability of the RBAO process [71,72]. Other possible method for the production of complex-geometry, near net shaped RBAO ceramics is the low-pressure injection molding (LPIM) [77]. In this case, a binder system based on paraffin is used as carrier for the RBAO particles [78]. Low temperatures (70-90°C) and pressures (0.2-0.8 MPa) are needed in this method for the production of RBAO green bodies [14,78]. Although no plastic deformation of Al particles takes place, high green densities of up to 60 %TD are achieved in LPIM by adjusting the solid content of the suspensions with the help of different polar surfactants [78]. Nevertheless, the mechanical strength of sintered injection-molded RBAO parts is usually 50-60% lower than that of their cold-isostatic pressed counterparts [77]. This is due to large defects formed by air or volatile species that remain entrapped during the injection or debinding processes, leading to large pores or voids after sintering [77].

2.3.3 RBAO as matrix in ceramic composites

The use of RBAO as a means to avoid sintering-related matrix cracks in CMCs has been suggested by many authors [3,45,60,73]. In addition to the easy incorporation of non-shrinking second phases due to the low shrinkages [15,71], superplastic deformation during sintering helps reducing densification mismatch stresses between matrix and reinforcement, also contributing to crack mitigation [73,79]. Other factor mentioned as a benefit of RBAO matrices is the easy flow of matrix particles around fibers, due to the plastic deformation of aluminum during pressing [45,73]. However, this does not apply for long fiber reinforced composites produced by infiltration techniques.

Wendorff *et al.* [19,79,80] were the first to demonstrate the possibility of producing defect-free, RBAO-matrix composites reinforced with monocrystalline alumina filaments (sapphire fibers with a diameter of ~ 120 μm). Their work



focused on the analysis of the fiber-matrix interfacial behavior in model composites, containing a few fibers dispersed in the matrix [80]. Results showed that composites sintered up to 1300°C presented crack deflection and fiber-matrix debonding, without the need of fiber coatings (damage tolerance enabled by the porous matrix). On the other hand, toughening mechanisms in composites sintered above 1300°C were only observed in the presence of weak interphases [79]. Although interesting results were found, the knowledge obtained with the investigation of model specimens was not transferred to full-scale, RBAO-matrix composites. Additionally, the use of small diameter, commercial oxide fibers was only investigated to a rudimentary level [19].

The use of RBAO matrix was also investigated by Keller *et al.* [18], who analyzed minicomposites consisting of a few Nextel™ 610 fiber tows infiltrated with an RBAO-containing slurry suitable for gel-casting. The objective here was to produce dense matrix composites reinforced with monazite-coated fibers. The use of fiber tows resulted in composite samples with considerable higher fiber volume contents than those investigated by Wendorff. In this case, however, the authors did not succeed in producing defect-free RBAO matrices [18]. Radial cracks were observed in the minicomposites, leading to overall high porosities (>25%), although dense matrix regions (>90%) were observed between the cracks [18]. Again, this investigation was limited to small samples and no full-scale composite was produced.



3 Preliminary studies: Definition of a suitable thermal treatment for RBAO-matrix composites

3.1 Introduction

Producing a good performing ceramic matrix composite is not just a matter of incorporating fibers into a ceramic matrix and sintering them together. Depending on the processing parameters used, what should be a strong and tough composite may behave as a brittle, monolithic ceramic. One of the key processing parameters controlling this behavior is the sintering temperature.

As discussed in section 2.1.1, a prerequisite to achieve both strength and toughness in a CMC is the deflection of matrix cracks at fiber-matrix interfaces, which preserves fibers from a premature failure. This is achieved in this work by the porous matrix approach, described in section 2.2. Porosity is obtained here by partially sintering the matrix particle network. Sintering temperature should therefore be carefully selected in order to obtain a matrix which is weak enough for damage tolerance and strength under fiber-dominated loadings, while sufficiently strong to guarantee acceptable off-axis properties. In addition, the sintering temperature should be selected, so that no strength degradation occurs due to fiber grain coarsening.

This chapter² focuses on the compatibility between RBAO matrices and commercially available, polycrystalline alumina fibers (Nextel™ 610). This preliminary investigation is performed on model composites and has the objective of determining the best thermal treatment, which may optimize the mechanical properties of composites from this fiber-matrix system. The selected thermal

² This chapter has been partially published in the article “Fiber-matrix compatibility in an all-oxide ceramic composite with RBAO matrix” in the *Journal of the American Ceramic Society* [81]. Copyright 2011 by John Wiley and Sons, Inc. The material from this article is reused in this thesis with permission.



treatment is then used later in the processing of full-scale composites ($v_f > 30$ vol%), manufactured by the novel processing route developed in this work.

Model composites are produced here by introducing a few single Nextel™ 610 fibers into RBAO green bodies and subsequently sintering them at different temperatures to investigate the fiber-matrix interface at different porosity levels. Toughening mechanisms such as crack deflection and fiber pullout are qualitatively investigated by (i) analyzing the path of Vickers-induced matrix cracks formed in the vicinity of the fibers and (ii) by evaluating the crack surface of bending samples, respectively. The experimental results³ are then compared to theoretical calculations conducted to predict the crack deflection behavior as a function of matrix porosity, taking into account the crack deflection parameter introduced by Fugita *et. al.* [42] (Eq. 8). For this purpose, elastic modulus and fracture toughness of the RBAO matrices are measured by means of nanoindentation and Single Edge V-Notch Beam (SEVNB) techniques, respectively. Since the grain growth of Nextel™ 610 may also be influenced by the surrounding matrix [82], the grain growth of fibers embedded in RBAO matrices is also investigated at different sintering temperatures. Finally, an aged sample is evaluated, as a means to analyze the effect of long-term temperature exposure on the crack deflection behavior and fiber grain growth.

3.2 Materials and methods

3.2.1 RBAO Matrix

The RBAO matrix powder was prepared by attrition milling 40 vol% aluminum powder (ECKA AS 081, 20 μm average particle size, Eckart-Werke, Wackersdorf, Germany) together with 30 vol% fine alumina powder (Ceralox HPA 0.5, 0.4 μm average particle size, RWE-DEA, Hamburg, Germany), 10 vol% coarse alumina powder (Almatis T60, 13 μm average particle size, USA) and 20 vol% fine yttria-stabilized zirconia powder (TZ-3Y, 28 nm average crystallite size, Tosoh, Toyama, Japan). The coarse alumina powder was added to enhance the milling efficiency and achieve a final particle size of ~ 1 μm . This is important not just for the

³ Part of the experiments presented in this chapter was performed with the help of M.Sc. Seyed M. Goushegir during his master thesis [20].

oxidation process, but also to achieve a good infiltration of fiber bundles during the processing of full-scale composites. YSZ was added to enhance the aluminum oxidation process and improve the microstructure and mechanical properties, as discussed in section 2.3.1. Attrition milling (Netzsch PE 075, Netzsch Feinmahltechnik, Germany) was performed on 100 g powder batches, at 700 rpm for 7 hours. A 500 cm³ alumina crucible was used, together with 1500 g of 3 mm zirconia balls (YTZ grinding media, Tosoh, Toyama, Japan) and 200 ml acetone as the wetting media. After milling, the RBAO powder was dried for 48 h at room temperature in a drying cupboard, and subsequently sieved (200 μm opening sieve) in a vibratory sieve shaker (AS 200 digit, Retsch, Germany) for deagglomeration.

It is important to note that, in this preliminary investigation, the RBAO composition was not yet tailored to achieve zero shrinkage after sintering. The amount of fibers used in the model composites produced here is very low and does not impose large constraints during sintering, even at high temperatures. This enables the production of crack-free model composites, which are suitable for the analyses conducted in this initial evaluation. Tailoring of the aluminum amount is performed later in Chapter 6, when full-scale, RBAO-matrix CMCs are produced.

3.2.2 Fibers

Single Nextel™ 610 alumina fibers were obtained from a roving, which was cut into ~4 cm long fiber bundles and treated in a muffle furnace at 700°C for 30 min, in order to remove the PVA coating present in the as-received fibers. This treatment is called *desizing* and was performed according to instructions provided by the supplier [58]. A heating rate of 5°C/min was used.

3.2.3 Sample preparation

The preparation of RBAO-matrix model composites, as well as RBAO monolithic (fiber-free) samples is schematically shown in Figure 17. For the model composites, a layer of RBAO powder (~1.5 g) was first poured into a bar-shaped die (40 mm × 5 mm × 4 mm) and leveled. Then, a few single fibers (up to 5) were placed onto the RBAO powder bed using tweezers. Another layer of RBAO powder (~1.5 g) was then poured onto the fibers and the procedure was repeated for another layer of fibers and RBAO powder. The green bodies were consolidated

by uniaxial pressing at 15 MPa for 30 s (WCH 10, P/O/Weber, Germany), with subsequent cold isostatic pressing at 300 MPa for 2 min (KIPP 200ES, P/O/Weber, Germany). Monolithic samples were prepared by pressing 3 g of RBAO powder using the same pressing procedure described above. These samples were used to characterize matrix porosity, as well as elastic modulus and fracture toughness after each sintering condition. Sintering of both monolithic and model-composite samples was performed in air, in a box furnace (Nabertherm HT 04/17, Germany), for 30 min at temperatures from 1100°C to 1500°C, with temperature intervals of 100°C. The heating cycle is schematically shown in Figure 18. This was selected according to a DTA/TG analysis of the RBAO matrix powder (Figure 20), as will be shown in section 3.4.1. The slow heating rates up to 1000°C are necessary in order to avoid sample bloating or cracking due to gas evolution from the particle surfaces, or due to the expansion associated with the oxidation process.

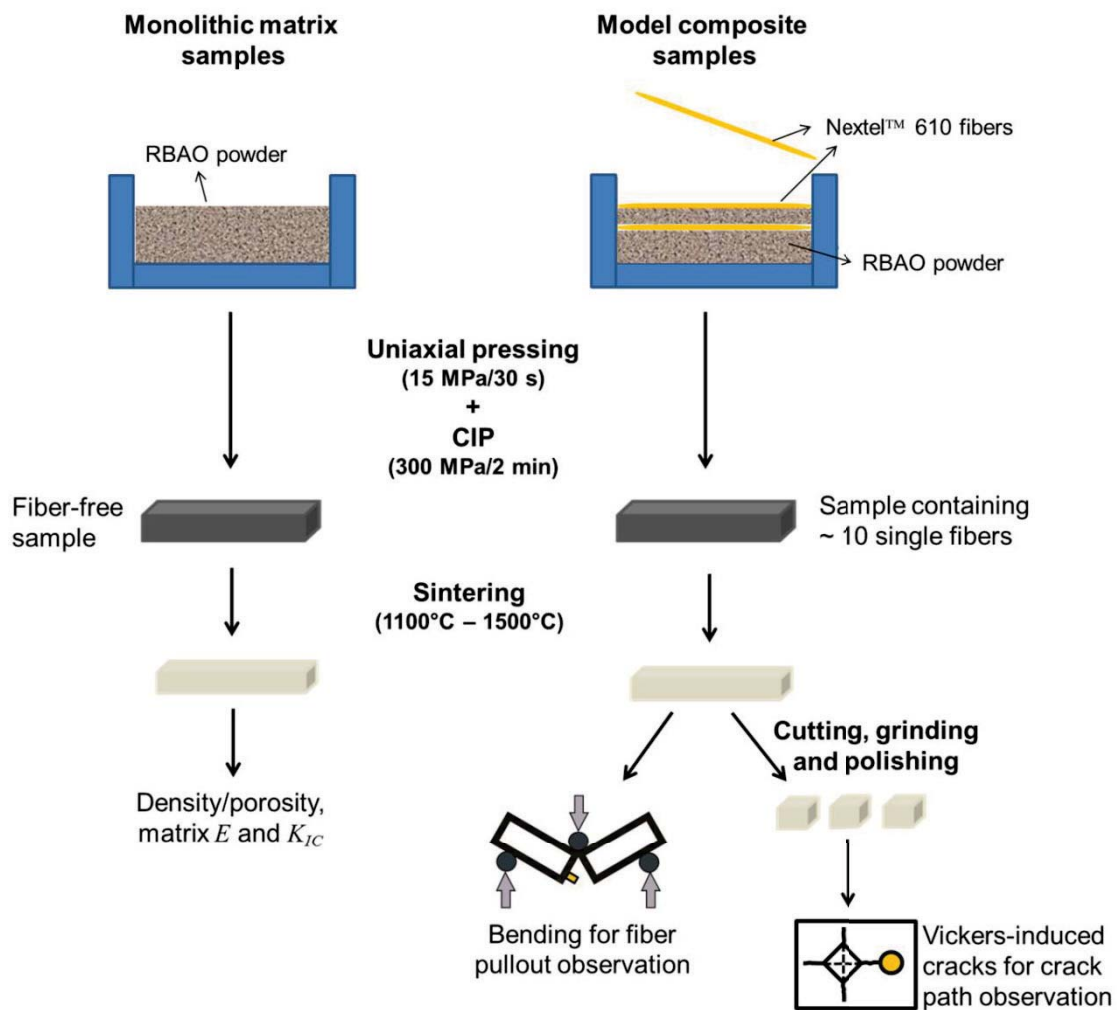


Figure 17: Schematic representation of the preparation of RBAO-matrix model composites. K_{IC} stands for fracture toughness and E for elastic modulus.

For some characterization methods, the sintered model composites were cut into cubes (~4 mm long), as indicated in Figure 17. This was done using a precision cut-off machine (EXAKT, Norderstedt, Germany), equipped with a 150 μm thick diamond disc. Samples were then mounted in a polymeric resin and the cross sections were ground and polished to a 3 μm finish using a semi-automatic polishing machine (Saphir 550, ATM, Mammelzen, Germany).

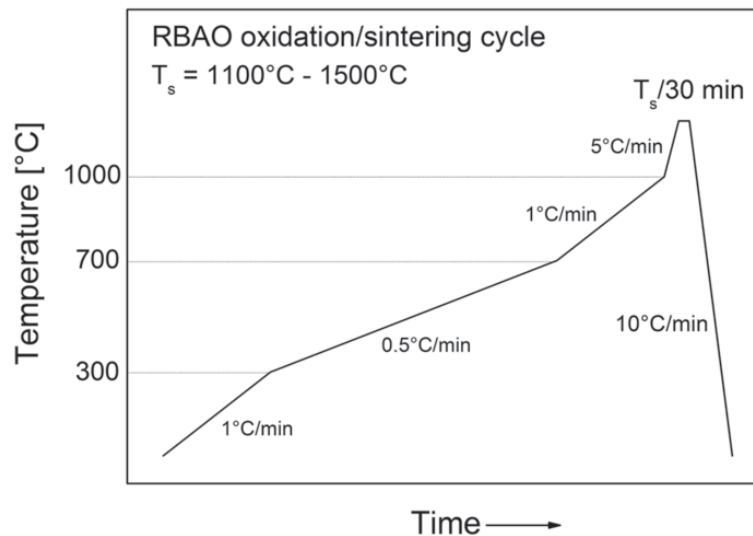


Figure 18: Heating cycle for oxidation and sintering of RBAO samples.

It should be emphasized that the samples produced here by pressing serve as an initial evaluation to determine a process window for the manufacture of full-scale, all-oxide composites by the novel route developed in this work. Since the amount of fibers used in the model composites analyzed in this chapter was very low (up to ~10 single fibers per sample), no fiber volume fraction was determined.

3.2.4 RBAO powder characterization

In order to investigate the milling efficiency, the particle size distribution of the milled RBAO powder was measured by laser diffraction using a Mastersizer S (Malvern Instruments, Herrenberg, Germany). For that, a sample of the milling slurry (~1 ml) was collected using a pipette and dispersed in ~4 ml ethanol. Before measuring, the slurry was sonicated for deagglomeration. For the sake of comparison, an RBAO powder with the same composition, but milled without the addition of coarse alumina particles was also measured.

Differential thermal analysis (DTA) was performed together with thermogravimetry (TG) on the milled RBAO powder in order to establish the heat



treatment presented in Figure 18. This was conducted in a Netzsch simultaneous thermal analyzer (STA 409, Netzsch, Selb, Germany), from room temperature to 1000°C at a heating rate of 1°C/min.

True density⁴ of a fully oxidized RBAO powder was measured using a helium pycnometer (AccuPyc 1305, Micromeritics, Aachen, Germany) equipped with a 5 cm³ chamber. For this analysis, loose RBAO powder was heated to 1300°C for 30 min, following the heating cycle presented in Figure 18. The value of true density obtained was used in the calculation of RBAO matrix porosity after sintering.

3.2.5 Characterization of monolithic samples

The density of the sintered monolithic samples was measured by the Archimedes' method using a mixture of 86 vol% glycerin and water, with known density. Porosity, P , was then calculated from the ratio between the density of the samples, ρ_s , and the true density of the fully oxidized RBAO powder, ρ_t , as follows:

$$P = 1 - \frac{\rho_s}{\rho_t} \quad \text{Eq. 12}$$

Fracture toughness, K_{IC} , of monolithic RBAO samples sintered at different conditions was measured by the Single Edge V-Notch Beam (SEVNB) technique [83,84]. Specimens were ground in a flat bed grinding machine (HFS204, Blohm, Hamburg, Germany) to obtain plan-parallel samples of 40 mm × 4 mm × 3 mm. The tensile surfaces were polished to a 1 μm finish and a notch perpendicular to this surface was introduced with a 150 μm thick diamond cutting disc. The notch tip was sharpened to a final radius of 10 μm with a razor blade embedded in diamond pastes from 6 μm to 1 μm. Notches were prepared so that their total initial length, a_i , was ~60% of the sample height, h . Five test specimens from each sintering temperature were fractured in a very stiff, in-house made 4-point bending device [85] with an inner span, $S_i = 10$ mm, and an outer span, $S = 20$ mm. Tests were performed at a displacement rate of 5 μm/s and K_{IC} values were calculated according to [86]:

$$K_{IC} = \frac{L_{max}(S - S_i)3T_M\sqrt{\delta}}{b\sqrt{h} h 2(1 - \delta)^{3/2}} \quad \text{Eq. 13}$$

⁴ True density is the density of the solid particles that compose a powder.

where L_{max} is the maximum attained force during the test, $\delta = a_i/h$ and T_M is a geometric factor as follows [86]:

$$T_M = 1.1215\sqrt{\pi} \left[\frac{5}{8} - \frac{5}{12}\delta + \frac{1}{8}\delta^2 + 5\delta^2(1-\delta)^6 + \frac{3}{8}\exp\left(-6.1342\frac{\delta}{(1-\delta)}\right) \right] \quad \text{Eq. 14}$$

As will be discussed in section 3.3, the measured values were fitted to a linear function, so as to predict K_{IC} of the RBAO matrices as a function of porosity.

A Nanoindenter XP (MTS Nano Instrument, Oak Ridge, USA) was used to determine the elastic moduli of the RBAO matrices sintered at different conditions by using the continuous stiffness measurement (CSM) technique [87]. A Berkovich tip was used for the measurements and the indents were performed so that the final indentation area was 8-10 times larger than the matrix grain size. Indents were performed on the polished surfaces of broken SEVNB samples. Twelve indents were made on samples of each heat treatment condition. The acquired data was also fitted to a linear function to predict the elastic modulus dependence of the RBAO matrix on porosity.

3.2.6 Characterization of RBAO model composites

To analyze the crack deflection behavior after each sintering temperature, a Vickers microhardness instrument (Zwick 3212, Germany) was used to create matrix cracks in the vicinity of the fibers, using a load of 5 kg for 10 s. Indents were performed on the polished cross-section surfaces of the model composites. The distance between the edge of the indenter impressions and the fibers was set to be at least 3-5 times the fiber diameter. Crack propagation paths were analyzed using scanning electron microscopy (SEM) (Gemini Leo 1530 FESEM, Zeiss, Peabody, USA) in at least 6 fibers distributed in samples sintered at each condition.

The occurrence of fiber pullout was investigated by analyzing the fracture surfaces of sintered model composites fractured using a 4-point bending device (ATS-Universal Testing Machine Series 1600, Applied Test Systems, Butler, USA) with inner and outer load spans of 10 mm and 20 mm, respectively. A notch perpendicular to the tensile side of the samples was introduced before testing using a blade runner embedded in 6 μm diamond paste. Since the objective of these



experiments was only to qualitatively observe the occurrence of fiber pullout from the fracture surfaces, no mechanical data was obtained from these bending tests.

Microstructure of fibers after the different sintering temperatures was observed from polished and etched cross-sections of the model composites, using the in-lens detector of the SEM. Etching was first performed chemically, by polishing the cross sections with an active silica-based solution (OP-S, Struers, Willich, Germany) for 15 min. Subsequently, thermal etching was conducted in a box furnace for 15 minutes at 100°C below the sintering temperature of the samples. The average grain sizes of the fibers were measured using the lineal intercept method. For this, 6 arbitrary lines were drawn over the SEM micrographs of the fibers and the number of grains intercepting each line was counted. Average grain sizes were then determined by dividing the total true line length (calculated considering the scale bar of each micrograph) by the total number of grains counted.

Ageing experiments for 100 h at 100°C below the sintering temperature were performed on an as-processed sample sintered at 1300°C to observe the possible changes in the fiber-matrix interface, as well as in the fiber microstructure. Vickers matrix cracks were also induced in the aged sample, so as to observe the crack path near the fiber.

3.3 Theoretical calculations for the prediction of crack deflection/penetration behavior

In this work, the dimensionless parameter Σ (Eq. 8) introduced by Fugita *et al.* [42] to predict the probability of crack deflection in ceramic composites is modified, so as to predict the crack deflection behavior in the RBAO-Nextel™ 610 system as a function of matrix porosity.

Based on values of K_{IC} and elastic modulus, E , the toughness of a material can be estimated by the well-known relationship:

$$\Gamma = \frac{K_{IC}^2}{E} \quad \text{Eq. 15}$$

Substituting this equation in Eq. 8, one obtains:

$$\Sigma = 0.134 \left(\frac{K_f}{K_m} \right)^2 \left(\frac{E_m}{E_f} \right) \left(1 + \frac{E_f}{E_m} \right)^{0.9} \quad \text{Eq. 16}$$

where K_f and K_m are the fracture toughness of the fiber and matrix, respectively.

To determine the dependence of fracture toughness on porosity of the RBAO matrices, a linear function was fitted to the experimental K_{IC} data as follows:

$$K_m = K_o(1 - aP) \quad \text{Eq. 17}$$

where K_o is the fracture toughness of a completely dense matrix and P is the porosity.

The same was done with the values of elastic modulus measured by nanoindentation, which were fitted using the following equation:

$$E_m = E_o(1 - \kappa P) \quad \text{Eq. 18}$$

where E_o is the elastic modulus of a completely dense matrix.

Combining Eq. 17 and Eq. 18 with Eq. 16, the crack deflection parameter can be calculated as a function of RBAO matrix porosity as follows:

$$\Sigma = 0.134 \left[\frac{K_f}{K_o(1 - aP)} \right]^2 \left[\frac{E_o(1 - \kappa P)}{E_f} \right] \left[1 + \frac{E_f}{E_o(1 - \kappa P)} \right]^{0.9} \quad \text{Eq. 19}$$

A value of $E_f = 380$ GPa, as reported by the supplier [58], was used in the calculations. The fracture toughness of the fiber was considered equal to that of a fine grained, dense alumina sample, measured by Yoshimura *et al.* [88], so that $K_f = 3.68 \text{ MPa}\sqrt{\text{m}}$.

As mentioned in section 2.2.1, the condition for crack deflection is met when $\Sigma > \omega$. In a conservative design in which the interface toughness is considered equal to the matrix toughness, $\omega = 1$ (see Eq. 7) and crack deflection at fiber-matrix interfaces is expected when $\Sigma > 1$.



3.4 Results

3.4.1 Powder Characterization

The particle size distribution of the RBAO precursor powder used for the production of model composites is shown in Figure 19 (blue curve). This diagram also shows the effect of the addition of a coarse alumina powder on the RBAO particle comminution. Using the coarse alumina powder described in section 3.2.1, a median particle size (D50) of 1.4 μm was achieved, together with a narrow distribution curve. On the other hand, without the addition of coarse alumina particles, the curve is much broader with a D50 of 2.7 μm .

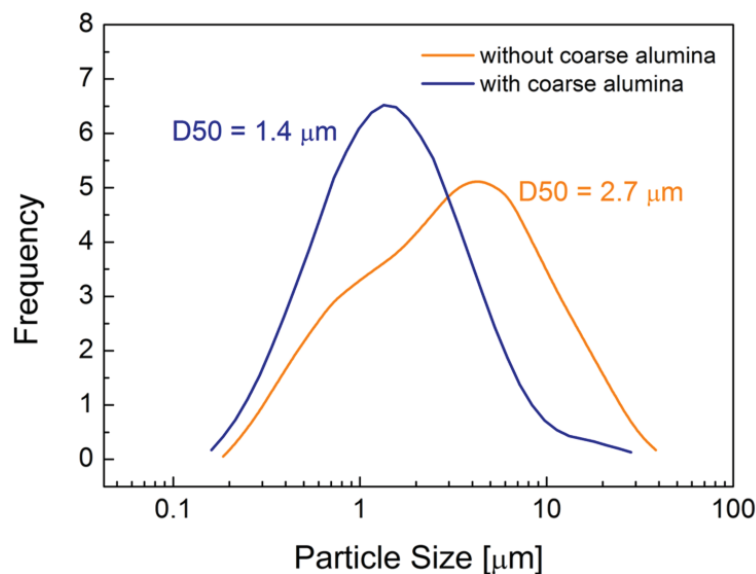


Figure 19: Particle size distribution of the RBAO matrix powder used in the preparation of model composites (blue curve). For the sake of comparison, the distribution of an RBAO powder milled without the addition of coarse alumina particles is also shown (orange curve).

An average value of $\rho_t = 4.41 \pm 0.02 \text{ g/cm}^3$ was measured by He-pycnometry for the true density of the fully-oxidized RBAO loose powder. This is in good agreement with the value of 4.40 g/cm^3 predicted by the rule of mixtures for the nominal RBAO composition after full oxidation, i.e., 20 vol% tetragonal zirconia (6.09 g/cm^3) and 80 vol% alumina (3.98 g/cm^3).

Figure 20 shows the results of the simultaneous thermal analysis conducted on the RBAO green powder. The weight lost between room temperature and $\sim 300^\circ\text{C}$ may be attributed to the evaporation of water and decomposition of hydroxides and organics present on the freshly milled particle surfaces. In order to avoid sample

bloating because of these volatiles, a slow heating rate of $1^{\circ}\text{C}/\text{min}$ was adopted between room temperature and 300°C for the RBAO heating cycle shown in Figure 18. Above 300°C , the sample starts gaining weight, which indicates the beginning of the oxidation process. In the solid state, the maximum oxidation rate occurs at $\sim 506^{\circ}\text{C}$, indicated by the sharp exothermic peak on the DTA curve. At 660°C , the remaining aluminum particles melt and oxidation continues slowly by liquid/gas reaction until $\sim 817^{\circ}\text{C}$. At this temperature no more variation on the sample mass is detected, indicating the complete oxidation of the aluminum particles.

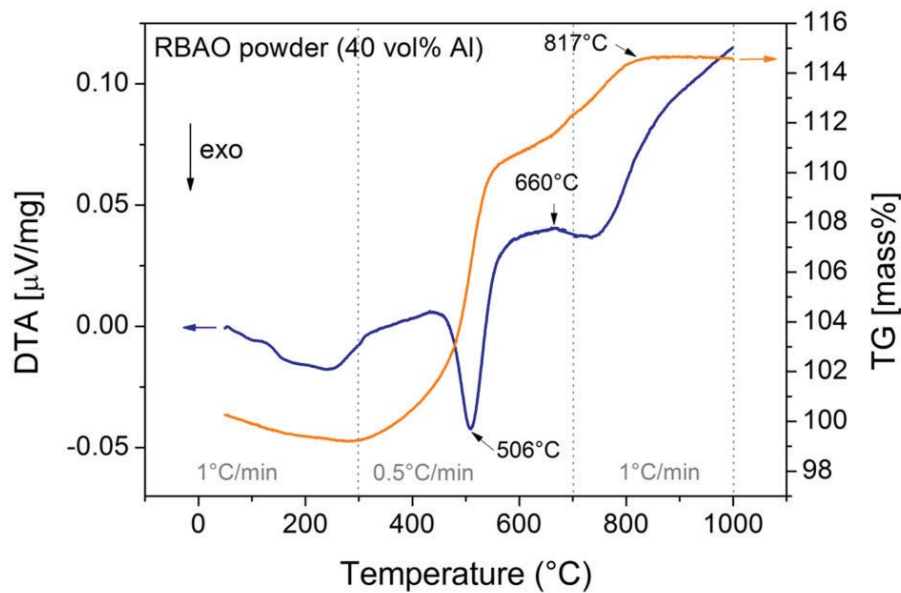


Figure 20: DTA/TG analysis of the RBAO precursor powder after 7 h milling. The heating rates selected after this analysis are also indicated.

Because of the highly exothermic oxidation reaction between $\sim 400^{\circ}\text{C}$ and $\sim 600^{\circ}\text{C}$, an even slower heating rate is necessary, so as to produce crack-free RBAO samples. Figure 21 shows a comparison between two monolithic RBAO samples produced with the same precursor powder, but using different thermal cycles. The sample shown in Figure 21(a) was sintered using a heating rate of $1^{\circ}\text{C}/\text{min}$ until 1000°C , while the sample shown in Figure 21(b) was sintered according to the heating cycle presented in Figure 18. The presence of cracks in the sample shown in Figure 21(a) indicates that a heating rate lower than $1^{\circ}\text{C}/\text{min}$ is necessary during the oxidation reaction. Therefore, a value of $0.5^{\circ}\text{C}/\text{min}$ between 300°C and 700°C was selected for the sintering of composites in this work. Between 700°C and 1000°C , a heating rate of $1^{\circ}\text{C}/\text{min}$ was selected, since the oxidation process



continues further. Above 1000°C, the heating rate can be increased to 5°C/min, as indicated in Figure 18, in order to decrease the total time of thermal treatment.

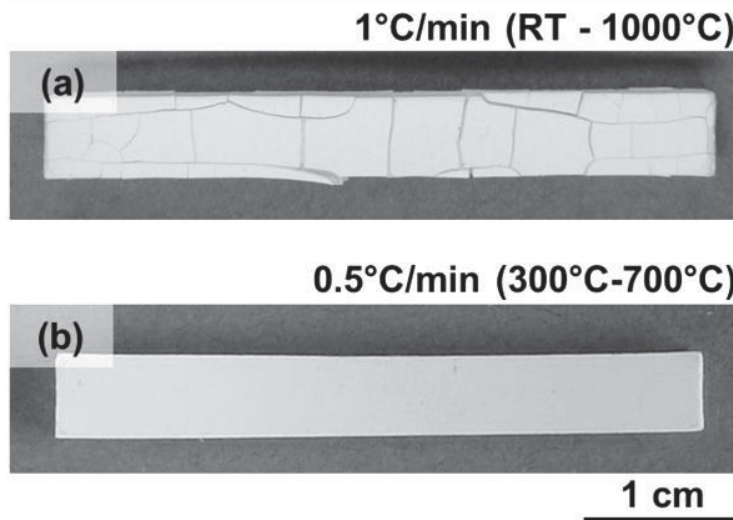


Figure 21: Effect of heating rate on the sintering of RBAO samples. (a) sample heated at 1°C/min between room temperature (RT) and 1000°C and (b) sample sintered according to the heating cycle shown in Figure 18.

3.4.2 Matrix properties

The variation of elastic modulus as a function of porosity resulting from the different sintering temperatures of the RBAO matrices is shown in Figure 22. Porosity values varied from $37 \pm 1\%$ to $19 \pm 1\%$ in samples sintered between 1100°C and 1400°C, respectively. Increasing the sintering temperature to 1500°C results in a dense matrix with porosity of $5 \pm 2\%$. Due to this decrease in porosity with increasing sintering temperature, the elastic modulus of the RBAO matrices increases by a factor of ~ 4 with sintering temperatures from 1100°C to 1500°C. A value of 81 ± 7 GPa was measured for the elastic modulus of a sample sintered at 1100°C, while a value of 314 ± 24 GPa was measured for a sample sintered at 1500°C. The data was fitted according to Eq. 18, resulting in $E_0 = 348.27$ GPa and $\kappa = 2.15$. The values measured by nanoindentation in this study are in good agreement with values reported elsewhere [89] for porous RBAO samples measured by the resonant beam technique.

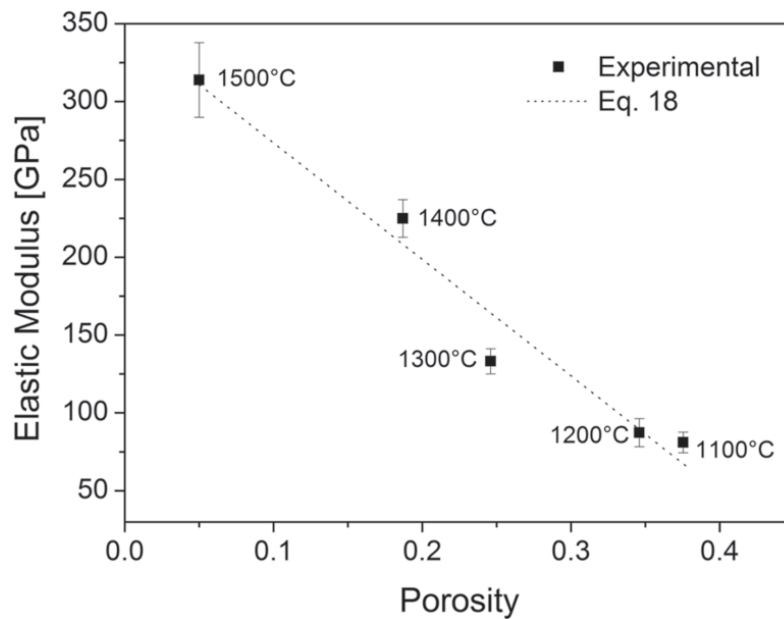


Figure 22: Elastic modulus as a function of porosity for the RBAO matrices sintered at different temperatures. Experimental data were obtained by nanoindentation.

The values of fracture toughness of the RBAO matrices also increased with increasing sintering temperature, as shown in Figure 23. K_{IC} increased from $1.3 \pm 0.02 \text{ MPa}\sqrt{m}$ for samples sintered at 1100°C , to $3.5 \pm 0.3 \text{ MPa}\sqrt{m}$ for samples sintered at 1500°C . The data fitting according to Eq. 17 resulted in $K_0 = 3.71 \text{ MPa}\sqrt{m}$ and $a = 1.88$.

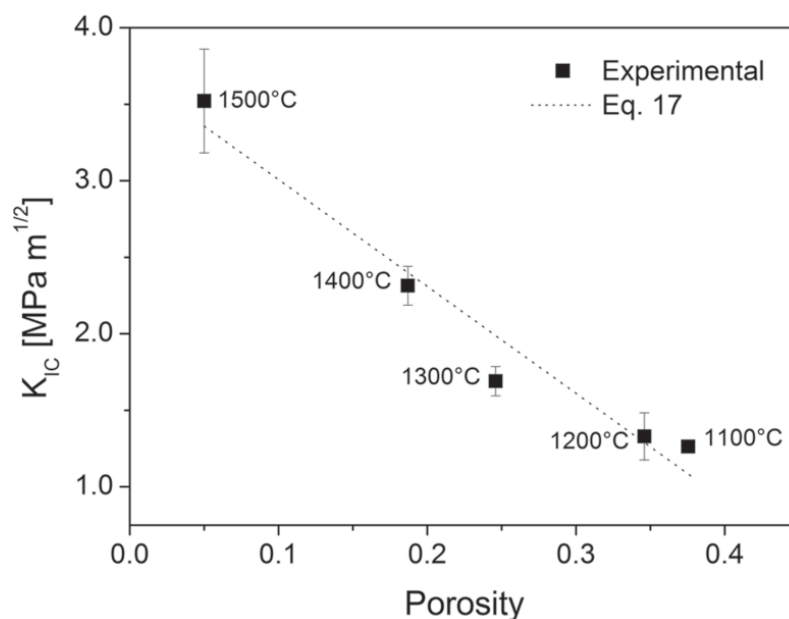


Figure 23: Fracture toughness as a function of porosity for the RBAO matrices sintered at different temperatures. Experimental data were obtained by the SEVNB method.



3.4.3 Experimental observations on model composites

The effect of matrix porosity on the crack deflection behavior of the RBAO-matrix model composites is shown in Figure 24, in which the path of Vickers-induced matrix cracks is demonstrated for representative samples sintered from 1100°C to 1500°C. Cracks are being deflected into the fiber-matrix interface in samples sintered up to 1300°C (Figure 24(a) to (c)), while they penetrate into the fibers in samples sintered at and beyond 1400°C (Figure 24(d) and (e)). This indicates that RBAO matrices with bulk porosities higher than ~25% (obtained at 1300°C) enable a damage tolerant composite behavior when Nextel™ 610 fibers are used as reinforcement.

Fracture surfaces of model composites sintered up to 1300°C are shown in Figure 25. Fiber pullout was observed in all these samples. Figure 25(a) and (b) show the pulled out fiber, while Figure 25(c) shows the matrix area where fiber-matrix debonding occurred. The smooth surfaces of the pulled out fibers shown in Figure 25(a) and (b), with very low amount of attached matrix particles, indicate that the surface quality of these fibers was not damaged during processing and reaction sintering.

The influence of sintering temperature on the microstructure of Nextel™ 610 fibers is shown in Figure 26, for representative samples sintered from 1100°C to 1500°C. Average fiber grain sizes of 81 ± 2 nm and 82 ± 4 nm were obtained for samples sintered at 1100°C and 1200°C, respectively, which are similar to values reported for the as-received fibers [3]. A pronounced fiber grain coarsening occurred in samples sintered at 1300°C (Figure 26(c)), in comparison to those sintered at lower temperatures. Average fiber grain sizes of 134 ± 18 nm, with some coarser, elongated grains reaching ~400-600 nm were measured for samples sintered at 1300°C. Increasing the sintering temperature to 1500°C resulted in an average grain size of 1.2 ± 0.4 μm, with some very large grains of ~3-8 μm (Figure 26(d)).

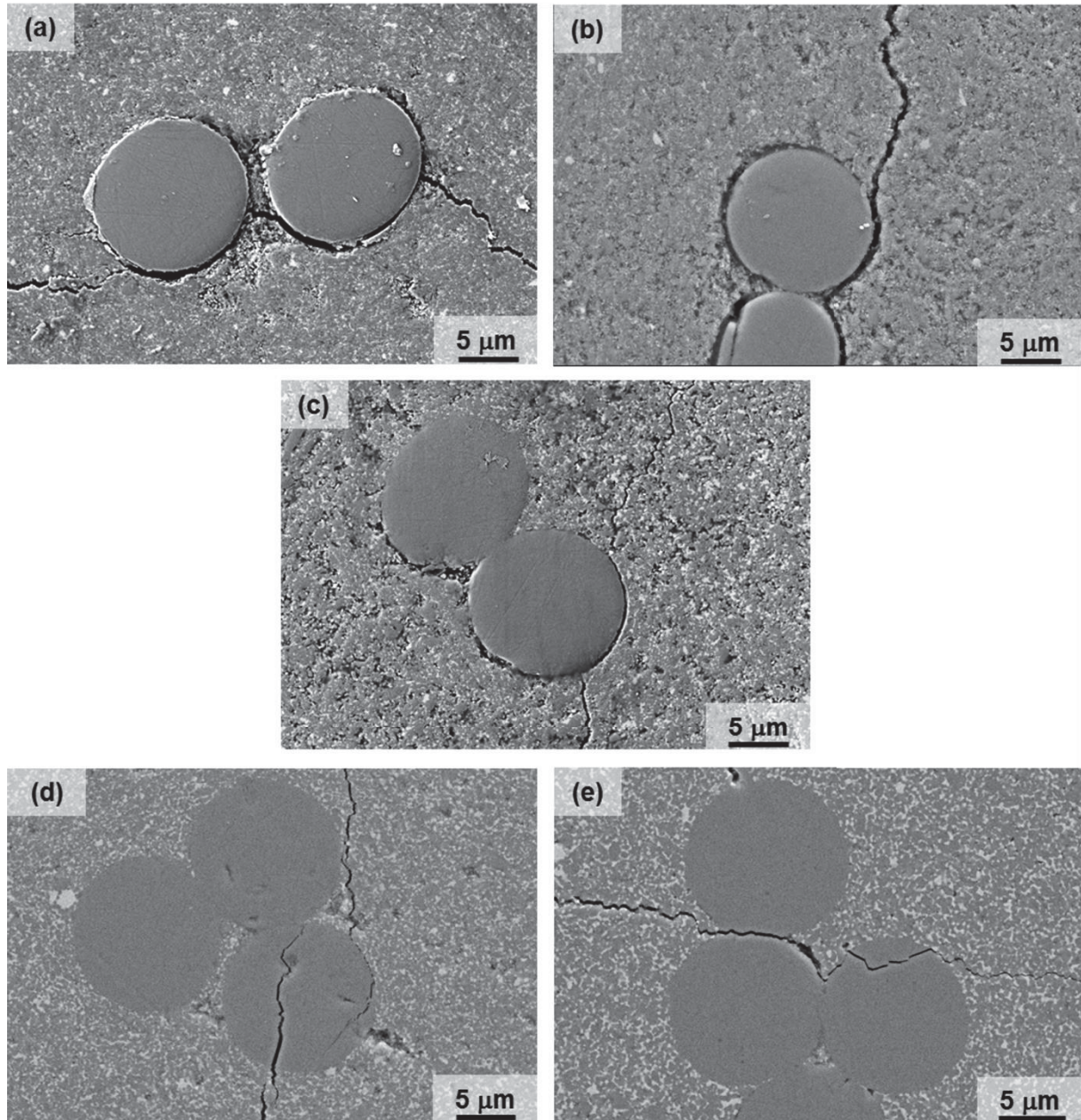


Figure 24: Crack propagation behavior in RBAO/Nextel™ 610 model composites sintered for 30 min at different temperatures: (a) 1100°C, (b) 1200°C and (c) 1300°C, (d) 1400°C and (e) 1500°C.

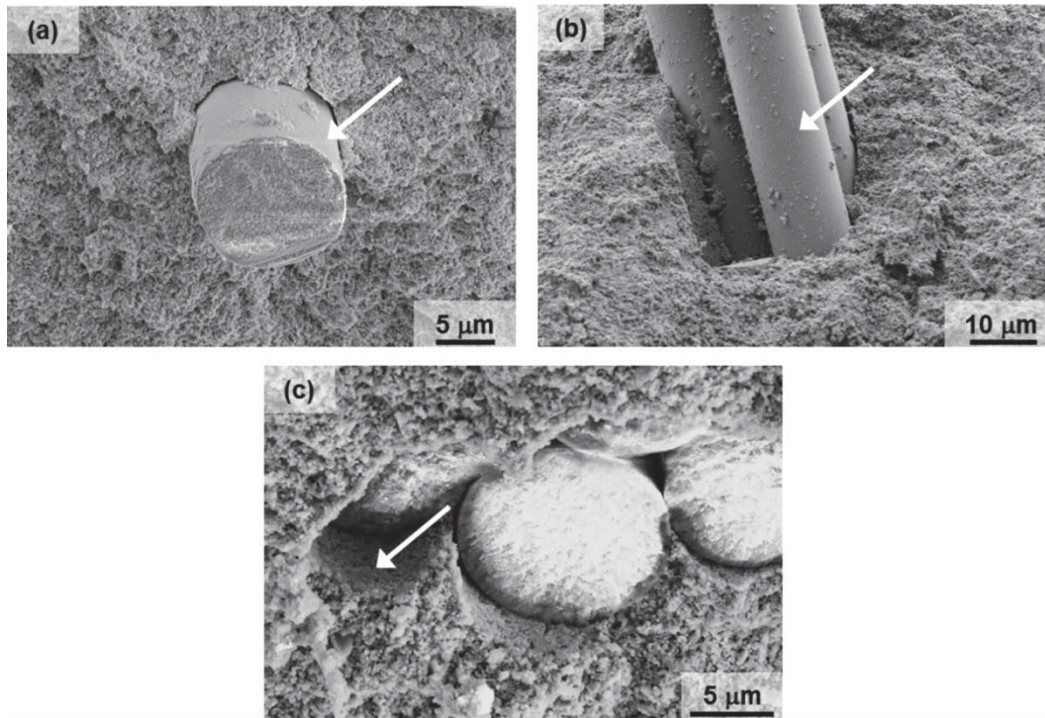


Figure 25: Fiber pullout observation on fracture surfaces of RBAO/Nextel™ 610 model composites sintered for 30 min at (a) 1100°C, (b) 1200°C and (c) 1300°C. The arrows in (a) and (b) indicate pulled out fibers, while the arrow in (c) shows the debonded matrix area related to a pulled out fiber.

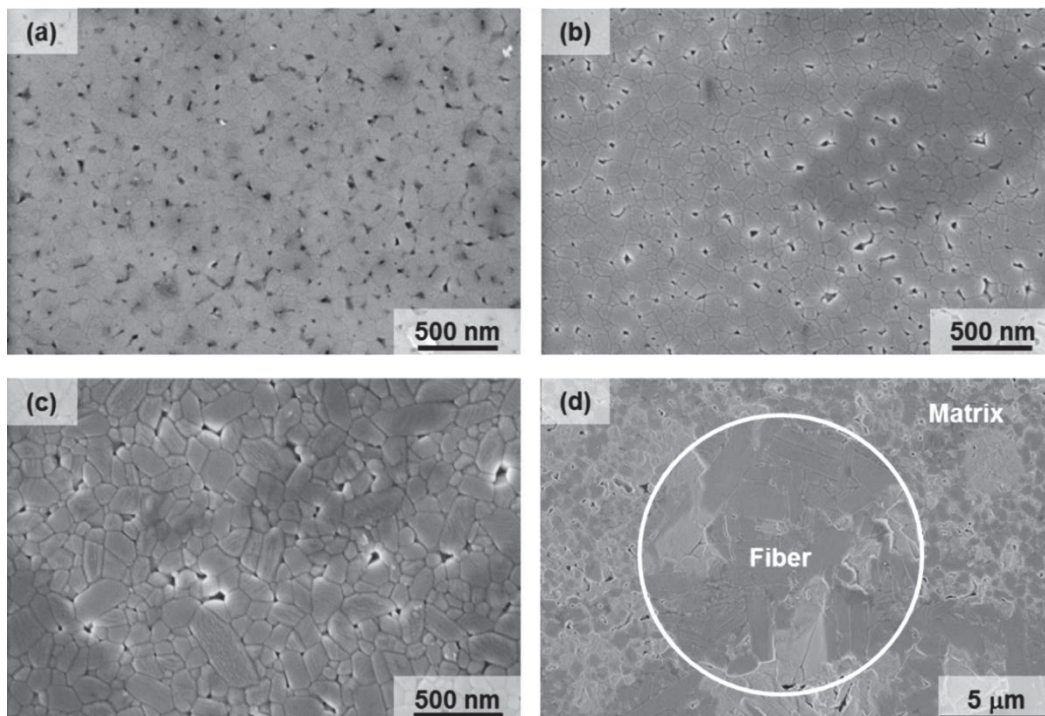


Figure 26: Grain structure of Nextel™ 610 alumina fibers in RBAO matrix samples sintered at (a) 1100°C (b) 1200°C, (c) 1300°C and (d) 1500°C for 30 min. Average grain sizes are 81 nm, 82 nm and 134 nm for the first 3 samples, respectively. Grains in the range of fiber radius or even larger are observed at 1500 °C. For the sake of clarity, the periphery of the fiber in the sample sintered at 1500°C is delineated.

Figure 27 depicts the microstructure of an aged sample previously sintered at 1300°C for 30 min. Qualitative observations show no evident change in the interface conditions in relation to the as-sintered sample: crack deflection still happens around the interface, with subsequent debonding (Figure 27(a)). Analysis of the fiber microstructure provides an average grain size of 132 ± 9 nm, similar to that of the fibers in the as-sintered condition.

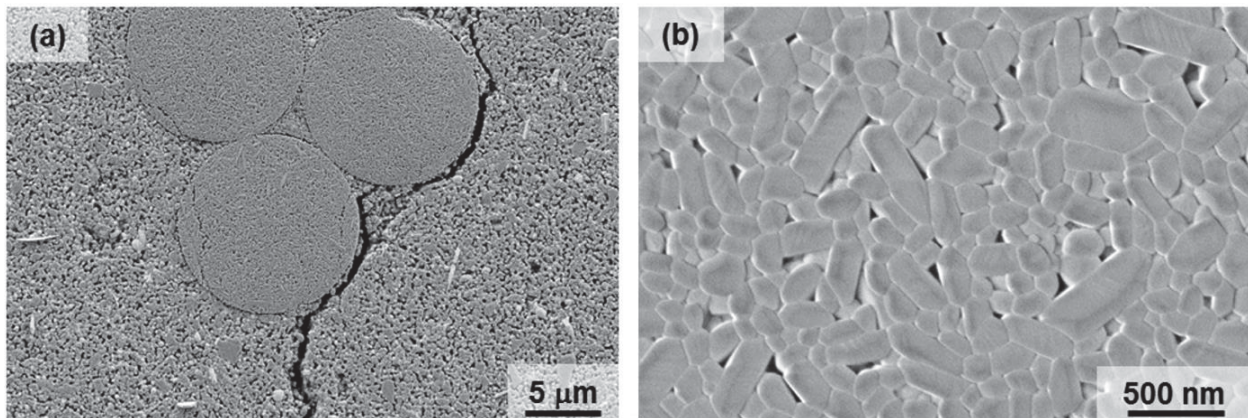


Figure 27: RBAO/Nextel™ 610 model composite sintered at 1300°C for 30 min and aged for 100 hours at 1200°C: (a) crack deflection behavior, and (b) microstructure of the fiber.

3.4.4 Prediction of crack deflection

Figure 28 shows the dependence of the calculated crack deflection parameter Σ on the matrix porosity, as predicted by Eq. 19. The experimental values were obtained using Eq. 16 with the measured RBAO values of E and K_{IC} , and using a fiber elastic modulus of $E_f = 380$ GPa [58] and $K_f = 3.68$ MPa \sqrt{m} [88]. The shaded area indicates the region where crack penetration is expected to occur, according to a conservative estimate in which the toughness of the interface is considered equal to the toughness of the matrix ($\omega = 1$). According to this conservative approach, a minimum matrix porosity of $\sim 33\%$ is necessary for cracks to be deflected into the RBAO/Nextel™610 interfaces. This is a larger value than the $\sim 25\%$ porosity experimentally determined for samples sintered at 1300°C, in which crack deflection was observed. This difference can be attributed to the lower packing efficiency of matrix particles around fibers, which leads to higher porosities in the interface regions than in the bulk matrix [56].

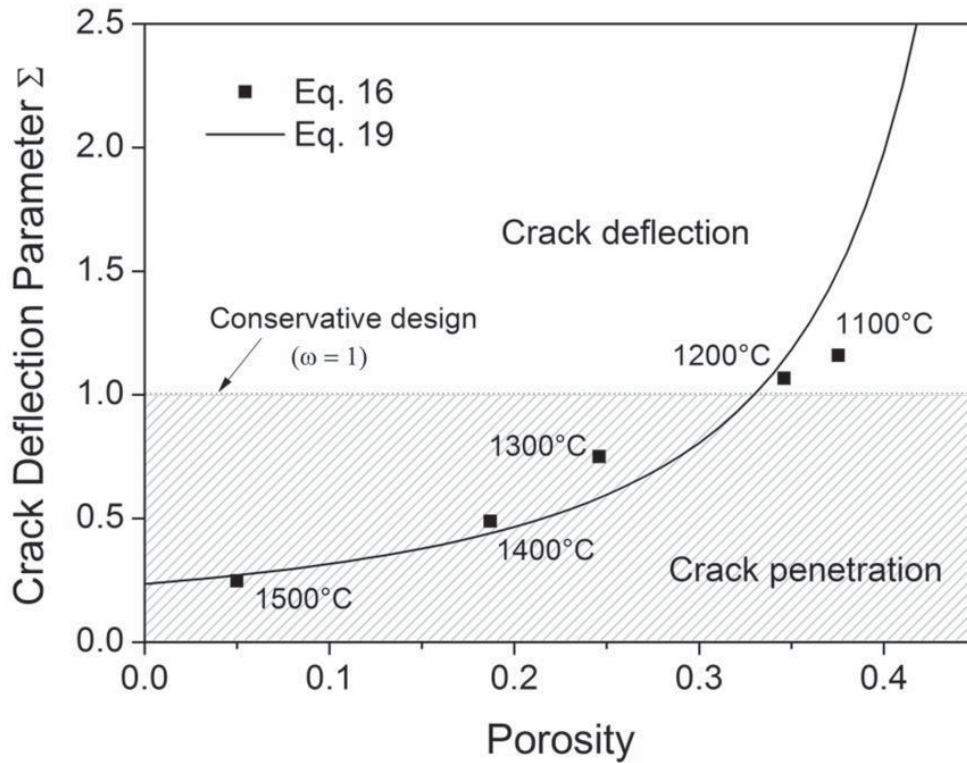


Figure 28: Dimensionless crack deflection parameter Σ calculated with Eq. 16 and Eq. 19, as a function of matrix porosity and sintering temperature. The shaded area indicates the region where crack penetration into fiber is expected to occur according to a conservative estimate in which $\omega = 1$. Fiber properties $E_f = 380$ GPa [58] and $K_f = 3.68$ MPa \sqrt{m} [88] were considered in the calculations.

3.5 Discussion

Due to the lower packing density of matrix particles around fibers [56], the interface properties, such as E and K_{IC} , are in fact lower than those of the bulk matrix, so that $\omega < 1$ (see Eq. 7). According to Eq. 8, the condition for crack deflection is found when $\Sigma > \omega$. Experimental observations shown in this chapter showed that crack deflection occurred for $\Sigma \geq \sim 0.75$, calculated for samples sintered at 1300°C using Eq. 16. A value of $\Sigma = \sim 0.5$ was calculated using Eq. 16 for samples sintered at 1400°C, for which crack penetration was experimentally observed. This means that the proportionality constant ω between the toughness of the RBAO/Nextel™ 610 interfaces and that of the RBAO matrices has an actual value that lies between 0.5 and 0.75. Consequently, composites of this system can be produced with bulk matrix porosities lower than the value estimated with the conservative approach (~ 33 vol%), since the larger local porosity in the interface regions will still guarantee the desired crack deflection behavior. By performing

additional experiments on samples sintered at temperatures between 1300°C and 1400°C, a more precise value of ω could be determined, and a new critical value for the bulk matrix porosity could be estimated. Nevertheless, based on the current state of this research, it has been shown that RBAO/Nextel™ 610 composites with matrices containing a bulk porosity of ~25 vol% (as obtained at 1300°C) present toughening mechanisms such as crack deflection and fiber pullout. In addition to damage tolerance, composites produced with such a matrix porosity would present the promising advantage of showing improved off-axis properties, due to the higher matrix density, in comparison to composites produced following the conservative porosity estimate.

However, it should still be investigated if such low porosity values (~25 vol%) could be achieved in full-scale composites produced by infiltration techniques. The model composites analyzed here were produced by pressing, which leads to the plastic deformation of aluminum particles and, consequently, to higher green densities [70,72]. This is, however, not expected for materials produced via RBAO suspensions. In addition, a sintering temperature of 1300°C leads to a considerable grain growth of the alumina fibers, even for short sintering periods of 30 min. The high-temperature stability of the polycrystalline alumina fibers, thus, remains as the major limiting factor for the maximum processing and service temperatures of RBAO-matrix CMCs.

The abnormal grain growth of alumina fibers has been previously explained by Schmücker and Mechnich [82] in terms of outwards diffusion of traces of SiO₂ present in the fibers, which normally act as grain growth inhibitors. Their investigation showed that grain coarsening of Nextel™ 610 can be strongly reduced, even at temperatures as high as 1400°C, by adding 1 wt% SiO₂ to the alumina matrix, thereby decreasing the driving force for outwards SiO₂ diffusion [90]. Considering the fact that a weak interface is maintained in the RBAO model composites up to 1300°C and the possibility of hindering the fiber grain growth by adding a small amount of SiO₂ to the matrix, it is possible to increase the processing temperature of the RBAO/Nextel™ 610 system to 1300°C, without considerably damaging the fiber mechanical strength and still getting toughness mechanisms active, even at only 25 vol% matrix porosity. Although very promising, this approach was not analyzed in this work. It appears, however, to deserve further investigation and remains here as a suggestion for future works.



Finally, Figure 27(a) and (b) shows no evidence of significant changes in the interface properties or microstructure of fibers by ageing samples up to 100 h at 1200°C (100°C below the sintering temperature). Though, more investigation is performed later on full-scale composites to analyze the effect of ageing on the microstructure and mechanical properties at longer time scales (see Chapters 5 and 7).

3.6 Conclusion

The qualitative study of RBAO-Nextel™ 610 model composites has pointed out that very strong and dense interfaces are achieved above 1300°C, leading to crack penetration into fibers and brittle fracture of the model composite samples. Therefore, a processing temperature $\leq 1300^\circ\text{C}$ is required to take advantage of the weak matrix concept and to enable damage tolerance in the investigated CMC system. Nevertheless, analysis of fiber microstructures revealed a pronounced grain coarsening at 1300°C, which may decrease the mechanical strength of composites.

Based on these results, a sintering temperature of 1200°C was selected for the processing of full-scale, all-oxide CMCs in this work. However, tests will also be performed on composites sintered at 1300°C (see Chapters 5 and 7) to evaluate the effect of this sintering temperature on the microstructure and mechanical properties of full-scale CMCs. In addition, it was observed that slow heating rates of 0.5°C/min to 1°C/min are necessary up to 1000°C, in order to avoid bloating or cracking of the RBAO matrix during the heat treatment.



4 Development of the novel processing route

4.1 Introduction

Because of the high reactivity of aluminum particles with water, aqueous slurries cannot be used and the use of organic carriers is fundamental for the processing of ceramic composites with RBAO matrix. In this work, a binder system based on paraffin-wax is used. This system was primarily developed at TUHH to produce RBAO components by low pressure injection molding and extrusion [77,78,91].

This paraffin binder system has a thermoplastic behavior: it is solid at room temperature and softens when heated above $\sim 60^\circ\text{C}$. Because of the high viscosity⁵ of the softened paraffin-based suspensions used in this work in relation to the liquid slurries⁶ usually used in the production of all-oxide composites, a direct adaptation of the liquid infiltration routes presented in section 2.2.3 is not possible. Instead, techniques available from the polymer science for the processing and handling of thermoplastic prepregs are used here.

In order to produce thermoplastic prepregs, melt impregnation techniques that combine the application of heat and pressure are normally used [93,94]. Heating is needed to soften the organics, whereas pressure is necessary to force the high viscous thermoplastics through the reinforcement and, therefore, obtain an effective impregnation [93]. In the novel route developed in this work, prepregs are produced in a way similar to the melt impregnation via double-belt press (DBP) [93]. In this technique, fiber fabrics are sandwiched between two polymer films and pressed between two steel belts containing a heating and a cooling zone.

⁵ According to measurements conducted by Coronel [77] on paraffin-based suspensions very similar to those used in this work, the viscosity of a 58 vol% loaded RBAO suspension heated at 80°C varies from ~ 40 to ~ 2 Pa.s, in the shear rate range of 1 to 50 s^{-1} , respectively. This viscosity range is very similar to that of mayonnaise in the same shear rate range [92].

⁶ As an example, the aqueous slurry (47 vol% mullite) used by Simon [6] for the impregnation of fiber textiles has a viscosity of ~ 0.5 Pa.s.



According to Åström [93], even highly viscous thermoplastics can be impregnated into fiber fabrics using this technique. The resulting thermoplastic prepregs are normally laid up by hand and consolidated by techniques such as compression molding (hot stamping) and DBP [93–95].

In this work, these concepts of the prepreg technology are combined with powder metallurgy techniques typical for ceramics, in order to develop a novel route to manufacture oxide matrix composites reinforced with two-directional (2D), oxide fiber fabrics. The development of this route is presented in detail in this chapter⁷. Besides being feasible for RBAO, the route should deliver composites with:

- homogenous microstructures;
- absence of delamination;
- reasonable fiber volume fractions ($v_f > 35$ vol%)

Additionally, the thermoplastic nature of the prepregs used in this novel route should give thermoformability to the green composites, allowing shaping and joining of different CMC parts. As briefly mentioned at the end of section 2.2.3, such operations are still a challenge for conventional liquid infiltration routes.

The development of the processing route was done empirically, by trial and error, until composites with the above listed microstructural features were produced. This procedure is shown schematically in Figure 29.

In the next section, materials and experimental procedures used in all concepts analyzed in this work are described. Sections 4.3 to 4.5 present the development steps performed until the novel prepreg processing route was established. The latter is then presented in its final form in section 4.6.

⁷ Parts of this chapter have been published in the articles “Production of oxide ceramic matrix composites by a prepreg technique” in the periodical *Materials Science Forum* [96] and “Multilayered fiber-reinforced oxide composites produced by the lamination of thermoplastic prepregs” in the periodical *Advances in Science and Technology* [97]. Both periodicals are published by Trans Tech Publications. Authors from these periodicals retain the right to reuse the published material, as is done in this thesis.

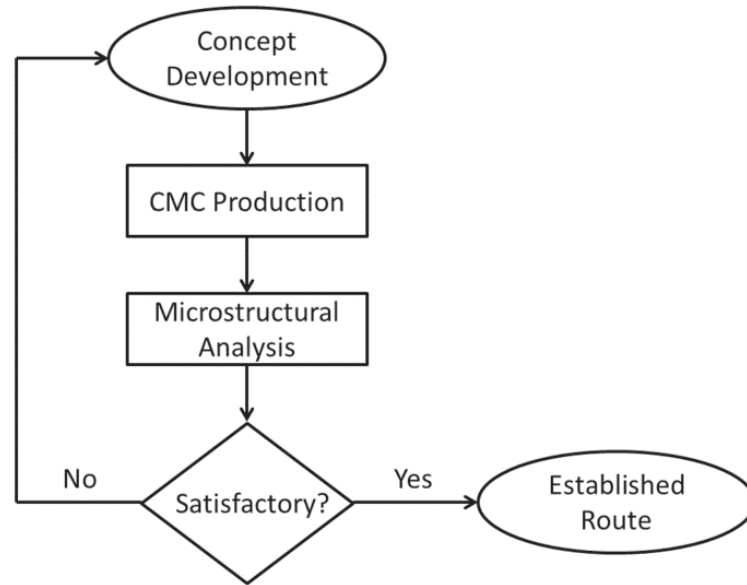


Figure 29: Flowchart showing the empirical procedure adopted for the development of the novel processing route presented in this work.

4.2 Materials and methods

4.2.1 Matrices and fibers

In order to facilitate the development process, only purely oxide matrix systems were used until the novel route was established. The introduction of RBAO matrix is very challenging and requires additional development steps, which are presented in Chapter 6. Preliminary tests of prepreg fabrication and consolidation of composite laminates were conducted using a pure alumina matrix (Ceralox HPA 0.5, average particle size of 0.4 μm , RWE-DEA, Hamburg, Germany). After proving the feasibility of the processing route, a powder mixture consisting of 80 vol% alumina (Ceralox HPA 0.5) and 20 vol% yttria-stabilized zirconia (TZ-3Y, 28 nm average crystallite size; Tosoh, Toyama, Japan) was used for further optimization. This powder mixture, hereafter designated by A8Z2, was selected as a reference material, since it has the same composition as the RBAO matrices after the full oxidation of the Al particles⁸.

⁸ As will be shown in Chapter 6, the composition of the RBAO precursor powders used in the manufacture of RBAO-matrix composites differs only in the amount of aluminum powder used in the starting milling composition. After full oxidation of the aluminum particles, all RBAO matrices contain ~80 vol% alumina and ~20 vol% yttria stabilized zirconia.



For the preparation of the A8Z2 powder, batches of 120 g of the alumina-zirconia mixture were homogenized at 500 rpm for 30 min in an attrition mill (Netzsch PE 075, Netzsch Feinmahltechnik, Germany). A 500 cm³ alumina crucible was used, together with 1300 g of 3 mm zirconia balls (YTZ grinding media, Tosoh, Japan) and 200 ml ethanol as the wetting media. The powder mixture was subsequently dried at room temperature in a drying cupboard and sieved (200 µm opening sieve) in a vibratory sieve shaker (AS 200 digit, Retsch, Germany) for deagglomeration.

Nextel™ 610 woven fabrics (DF-11, 8 harness satin, 1500 denier, 3M, Neuss, Germany) were used as reinforcement in all composites produced in this work. For the manufacture of prepregs, the fiber textile was cut into pieces of the desired composite dimensions and desized according to the procedure described in section 3.2.2.

4.2.2 Preparation of paraffin-based suspensions

The binder system used in this work was selected after the investigation from Coronel [77], who optimized the suspension composition developed by Leverköhne *et al.* [78] in order to achieve the lowest viscosity in a 58 vol% loaded RBAO suspension. The binder system is composed of a paraffin wax medium, together with different polar surfactants used to achieve appropriate rheological properties. These additives contain polar carboxylic or amine end-groups that physisorb or chemisorb on the oxide or Al particle surfaces, while their lipophilic polymeric chains extend into the nonpolar paraffin medium. This promotes the sterical stabilization of the suspension [78]. More details on the development of this binder system are presented elsewhere [77,78]. The optimized composition, as well as the materials used in this work for the production of paraffin-based suspensions, is shown in Table 3.

For the suspension preparation, all organic ingredients were melted in a glass beaker placed onto a hot plate at 100°C. The matrix powder was then gradually added, while manually mixing the suspension with a glass stirrer. After all matrix powder was incorporated, the suspension was homogenized on a three roller mill (EXAKT 120S, EXAKT, Norderstedt, Germany), whose rolls were preheated at 95°C. After solidification, the suspension was granulated using mortar and pestle,

so as to facilitate its handling during the subsequent processing steps. Figure 30(a) shows a picture of an RBAO suspension after granulation.

Table 3: Composition of the paraffin-based suspensions used in this work for the production of all-oxide composites with pure oxide matrices.

	Material	Supplier	Density (g/cm ³)	Content ^b (%)
Matrix	Alumina (HPA 0.5)	RWE-DEA	3.97	58.00
	– or – A8Z2	(produced in this work)	4.13 ^a	
Organic binder	Paraffin KX1313	Zschimmer & Schwarz	0.90	35.44
	Octadecylamine (ODA)	Sigma-Aldrich	0.90	2.96
	Licowax OP	Clariant	1.01	2.52
	Solsperse 3000	Zeneca	0.91	1.08

^aMeasured by gas pycnometry (AccuPyc II 1340, Micromeritics, Aachen, Germany) after drying and sieving the powder mixture.

^bComposition developed by Coronel [77].

4.2.3 Fabrication of thermoplastic prepregs

In a lab-scale, the production of thermoplastic prepregs via DBP was manually reproduced as follows: first, granules of the paraffin-based suspension were sprinkled onto an aluminum foil using a lab spoon to form a homogenous layer; then, a piece of the desized fiber fabric was placed onto this layer and another layer of the granulated paraffin-based suspension was sprinkled onto the fiber textile. A picture of the resulting textile-suspension sandwich is shown in Figure 30(b). This sandwich was then covered with another aluminum foil and subsequently placed onto a heating plate at ~115°C for the softening of the suspension. The aluminum foils were used as backing papers, to prevent the molten suspension from adhering to the heating plate or to the laminating roll.

To achieve a better temperature distribution, a flat stainless steel plate, previously heated at 115°C, was placed onto the textile-suspension sandwich, together with 2 metallic blocks used as weights (Figure 30(c)). After 10 min, the metallic plate and the weights were removed and the impregnation was manually performed by rolling a 2.5 cm diameter stainless steel roll onto the textile-suspension sandwich, as shown in Figure 30(d). After this procedure, the single prepreg layers, still



wrapped with the aluminum foils, were let cool down between 2 metallic plates at room temperature, in order to avoid warping. This procedure resulted in 2D thermoplastic prepregs that were stable and easy to handle at room temperature, after solidification of the organic binder. The produced prepregs could be either stored at normal labor conditions or be directly laid up and joined to consolidate CMC green bodies. Prepreg layup was always conducted by hand.

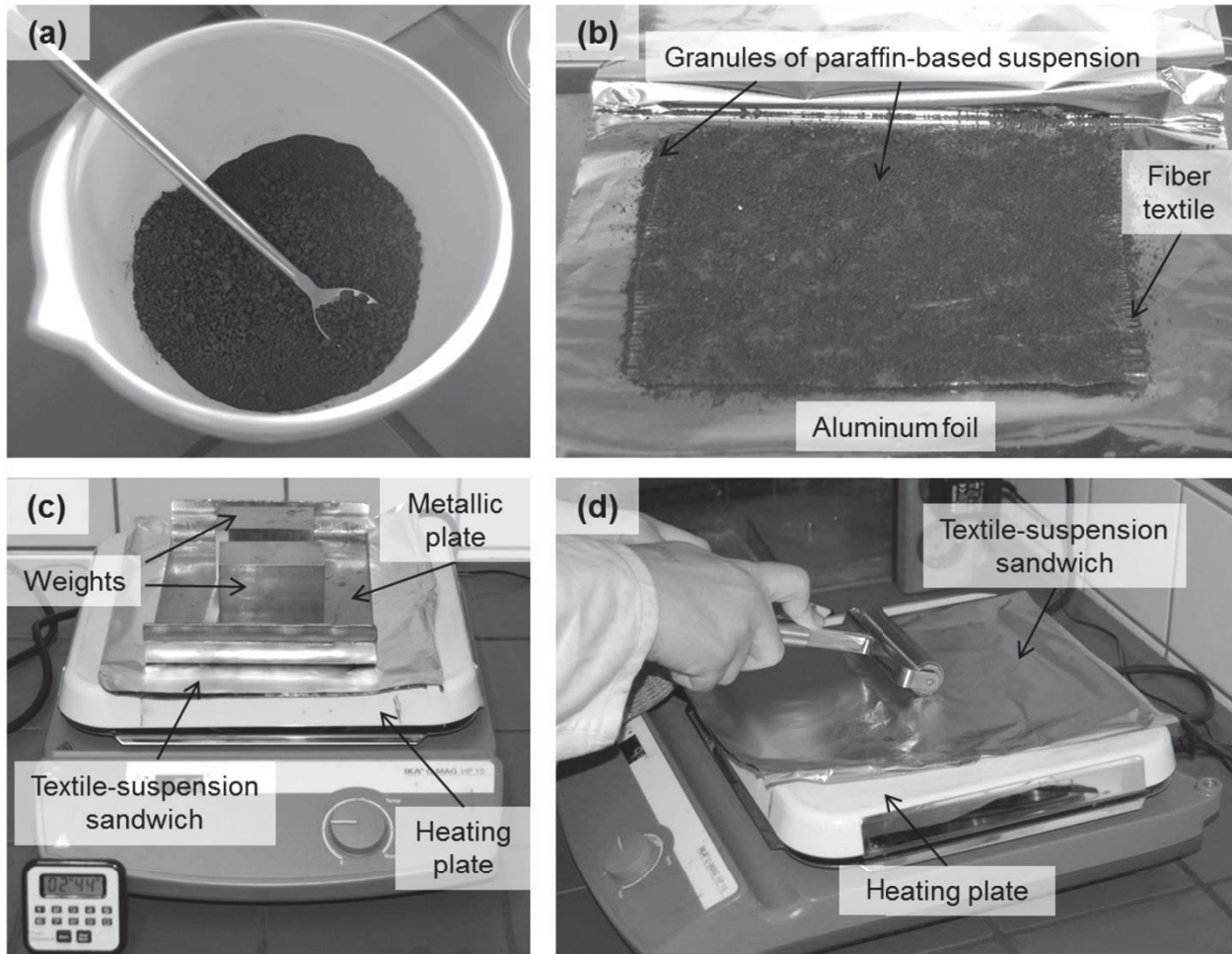


Figure 30: Pictures showing some steps of the prepreg manufacture: (a) granulated paraffin-based suspension; (b) fiber woven fabric sandwiched between two layers of the granulated paraffin-based suspension; (c) pre-heating of the textile-suspension sandwich; (d) manual melt impregnation using a stainless steel roll.

4.2.4 Warm pressing

Warm pressing was used in this work for two purposes: (i) for the consolidation of prepreg stacks in preliminary development phases and (ii) for the shaping

(thermoforming) of consolidated green composites into plan-parallel plates, in order to obtain appropriate samples for mechanical testing.

For this purpose, either prepreg stacks or pre-consolidated green composites were wrapped with aluminum foils and placed between two flat stainless steel plates, which subsequently served as pressing molds. The system was heated in a drying oven (Function Line T12, Thermo Scientific Heraeus, Germany) at 115°C for 15 min to soften the paraffin suspension and thereby allow the joining of adjacent prepregs during pressing. After heating, the system was quickly transferred to a uniaxial press (WCH 10, P/O/Weber, Remshalden, Germany), where it was consolidated (or shaped) at low pressures (~0.5 to ~1 MPa). The green composites were allowed to cool in the mold, before handling them to the subsequent debinding procedure.

4.2.5 Debinding and Sintering

Debinding was performed thermally, according to a procedure developed by Coronel [77] for the binder system used in this work. In this procedure, the organic components of the paraffin suspension are eliminated by a combining effect of capillarity and pyrolysis, in a three-step heating cycle (Figure 31). Capillary forces are achieved by embedding the green composite samples in an alumina powder bed (average particle size of 200 μm) used in the first and second debinding steps. The samples are then heated in a muffle furnace placed in a fume hood. The powder bed is changed between these two heating cycles, in order to avoid the saturation of the powder with the extracted organics.

According to a thermogravimetric analysis performed by Leverkusöhne *et al.* [78], the volatilization of the organic components starts at about 190°C. Nevertheless, the first debinding step is performed at 100°C, in order to remove organics by capillary forces and create an open porosity necessary for the flow of decomposition gases in the following higher temperature steps. The second step is performed at 190°C, in which the extraction of binders occurs both by capillarity and evaporation. In the last step, the green CMC bodies were removed from the powder bed and debinded in air at 330°C for 10 h, for the burnout of organics that still remained in the samples.



Sintering was performed in a box furnace at 1200°C for 30 min, following the RBAO heating cycle shown in Figure 18.

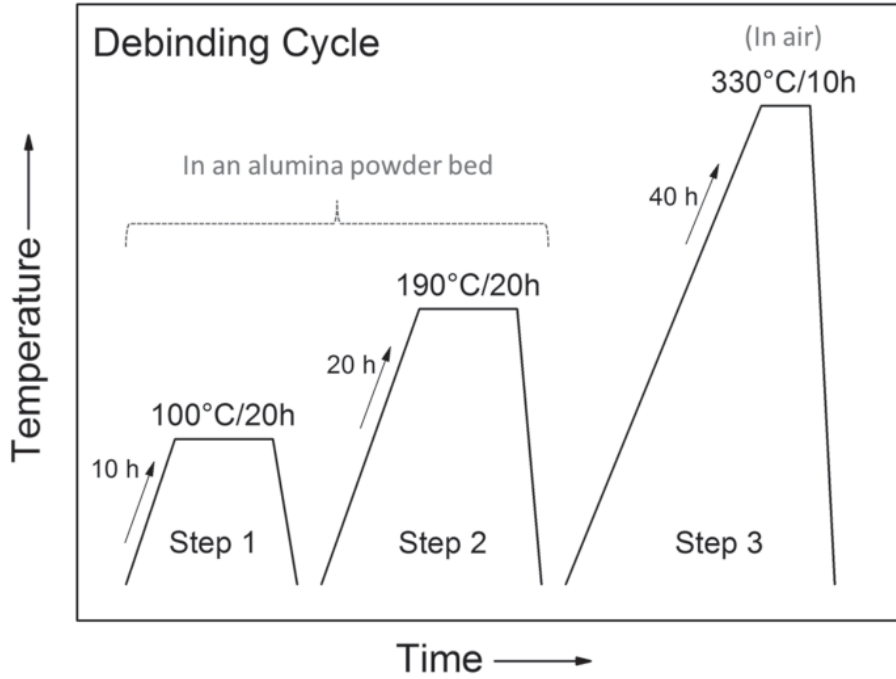


Figure 31: Debinding cycle used in this work.

4.2.6 Fiber volume fraction calculation

Fiber volume fraction of the sintered composites was calculated geometrically, according to:

$$v_f = \frac{m_{tex}^* A_{tex}}{\rho_f V_c} \quad \text{Eq. 20}$$

where m_{tex}^* is the mass per unit area of textile, A_{tex} is the total area of textile used in the composite, ρ_f is the density of the fibers and V_c is the volume of the sintered composite. For a composite plate with length l , width b and thickness h , $V_c = l b h$ and $A_{tex} = n l b$, where n is the total number of textile layers used. Hence, Eq. 20 can be simplified to:

$$v_f = \frac{n m_{tex}^*}{h \rho_f} \quad \text{Eq. 21}$$

A value of $m_{tex}^* = 0.0359 \text{ g/cm}^2$ was measured for the desized Nextel™ 610 woven fabric used in this work. The fiber density is $\rho_f = 3.9 \text{ g/cm}^3$, as provided by the supplier.

4.2.7 Sample preparation for microstructural analysis

For microstructural investigation, cross sections of the sintered composites were cut using a precision cut-off machine (Brillant 220, ATM, Mammelzen, Germany), equipped with a 150 μm thick diamond disk. In order to preserve the fibers and porous matrices during grinding and polishing, the samples were embedded in a cold-setting epoxy resin (Epofix, Struers, Willich, Germany) using a vacuum impregnation apparatus (Epovac, Struers, Willich, Germany). After curing the resin, the samples were ground and polished using a semi-automatic polishing machine (Saphir 550, ATM, Mammelzen, Germany). Grinding was performed using 800 to 1200 grit SiC papers. Polishing was subsequently conducted using diamond suspensions varying from 15 μm to 1 μm grain sizes. In most of the cases, the epoxy resin was thermally removed after sample preparation. This was done by heating the embedded samples in a muffle furnace at 800°C for 2 h. Microstructural analysis was conducted by SEM (ZEISS Supra VP 55, Carl Zeiss, Oberkochen, Germany) on gold-sputtered cross-sections.

4.3 Concept 1: Direct impregnation of fiber fabrics with the paraffin-based suspension

In preliminary experiments, the direct impregnation of fiber fabrics with paraffin-based suspensions was investigated. For that, a pure alumina matrix was used and the processing steps described from section 4.2.2 to 4.2.5 were followed, as schematically shown in Figure 32. The composite sample was 3 mm long and 3 mm wide. Four prepreg layers, stacked in a 0°/90° configuration, were used for its manufacture.

Figure 33 shows the microstructure of this composite.

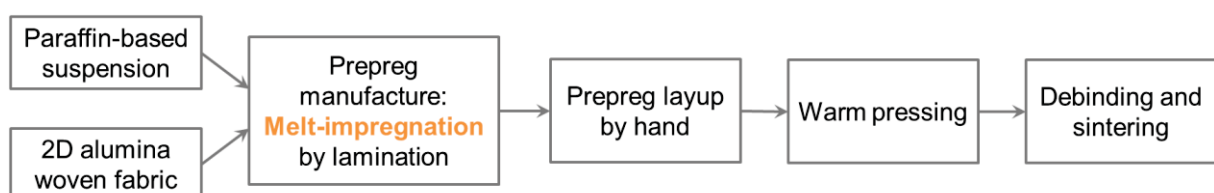


Figure 32: Flowchart of the first concept investigated for composite manufacture: direct impregnation of fiber fabrics with the paraffin-based suspension.

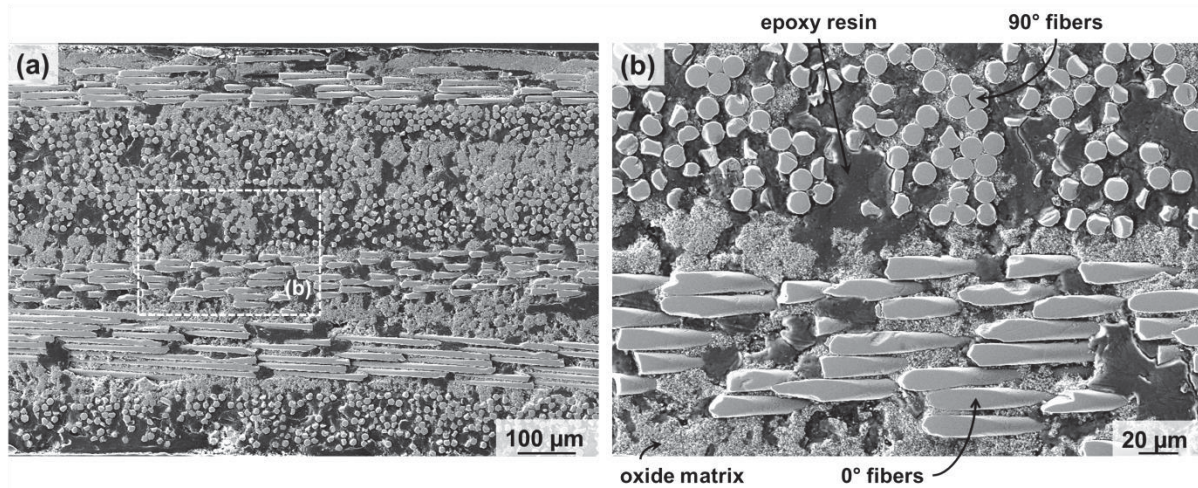


Figure 33: Composites produced via melt-impregnation of alumina fiber fabrics with an alumina-loaded, paraffin-based suspension. (b) is a higher magnification picture from the region indicated in (a). Composites were sintered at 1200°C for 30 min. The black regions are the epoxy resin used for microstructural preparation.

This first impregnation test showed that the manual lamination procedure used in this work (Figure 30(d)) does not allow for a good impregnation of oxide fiber textiles with the paraffin-based suspension. The black regions in

Figure 33(a) and (b) are the resin used to prepare the sintered sample for microstructural analysis and indicate the poor impregnation of the fiber bundles with ceramic matrix particles. Although the fiber volume content of this sample is high, the oxide matrix is not homogeneously distributed inside the fiber tows. This is also evident in Figure 34(a), which shows a Nextel™ 610 fiber fabric impregnated with a paraffin-based suspension loaded with 58 vol% alumina. Although the alumina fibers are covered with alumina particles to some extent, no complete bundle impregnation was achieved.

It appears, therefore, that the high viscous paraffin-based suspension used in this work requires higher impregnation pressures, which cannot be achieved by the manual procedure used here. In order to circumvent this difficulty, an additional impregnation step was included in the processing route, which is explained in the next section.

4.4 Concept 2: Introduction of a liquid slurry for the impregnation of fiber tows

An alternative to decrease the viscosity of the paraffin-based suspension, so that it can completely percolate the fiber bundles and fill them with matrix particles, is to decrease the solid content. This is, however, not interesting, since it would lead to lower matrix green densities, leading to larger shrinkages and crack formation during debinding and sintering.

Instead of that, a pre-impregnation step using less viscous slurries based on organic liquids was introduced in the processing route. In this step, desized fiber fabrics are immersed into liquid slurries of the matrix particles (usually ethanol-based), in order to impregnate the fiber tows prior to prepreg manufacture by lamination. The feasibility of this immersion process was qualitatively investigated by SEM on a Nextel™ 610 fiber fabric impregnated with an ethanol-based slurry containing 37 vol% RBAO and 0.6 wt% Dolacol D 1001 (Zschimmer und Schwarz, Lahnstein, Germany) as a deflocculant. As can be seen from Figure 34(b), the liquid infiltration resulted in a much better impregnation of fiber bundles than the direct melt impregnation with the paraffin-based suspension, shown in Figure 34(a).

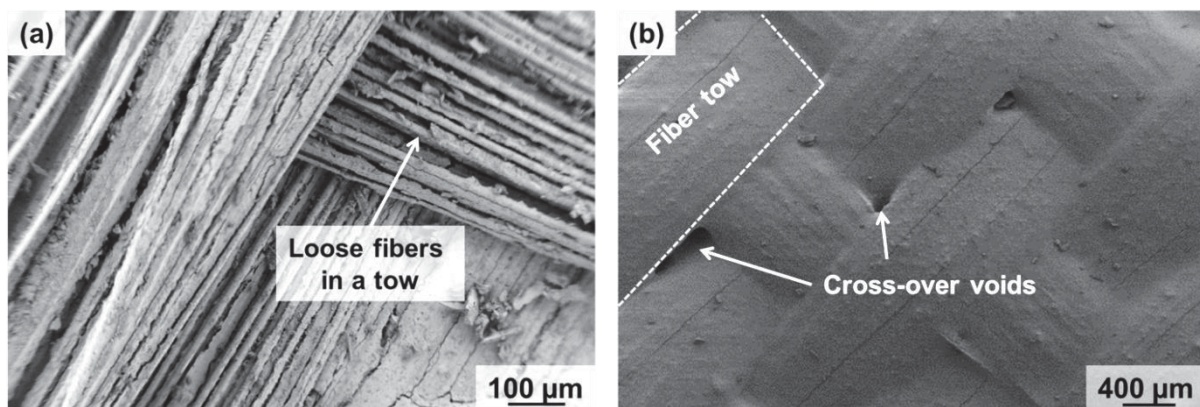


Figure 34: Surfaces of Nextel™ 610 fiber woven fabrics after different impregnation tests: (a) impregnation with an alumina-loaded, paraffin-based suspension via lamination; (b) impregnation with an ethanol-based RBAO slurry via immersion.

The liquid infiltration was then combined with the melt impregnation procedure, shown in Figure 30, to manufacture well impregnated, thermoplastic prepreps, as will be discussed in section 4.4.2. More details on the preparation of liquid slurries,



as well as on the resulting prepreg manufacturing procedure are presented in the next sections.

4.4.1 Preparation of liquid slurries

For pure oxide matrices, both water and ethanol can be used as the slurry media. In case of RBAO, only organics such as ethanol or acetone are allowed. The liquid slurries were prepared by attrition milling (PE 075, Netzsch Feinmahltechnik, Germany) using a 500 cm³ alumina crucible containing 1300 g of 3 mm zirconia balls (YTZ grinding media, Tosoh, Japan). All slurry components were homogenized for 15 min at 500 rpm. After mixing, the slurry was poured in a glass beaker for the subsequent infiltration of fiber textiles.

In case of alumina matrix, a 45 vol% concentrated aqueous slurry was prepared using 0.6 wt% Dolapix CE 64 (Zschimmer und Schwarz, Lahnstein, Germany) as a deflocculant. Additionally, ammonium hydroxide (NH₄OH) was used to adjust the pH of the slurry to ~10, which allowed repulsive interaction forces to act between the alumina particles, providing an adequate viscosity for the infiltration of fiber bundles.

The A8Z2 slurries were prepared by direct attrition milling the starting alumina and zirconia powders. Ethanol-based slurries containing 32 vol% solids were prepared using 0.6 wt% Dolacol D 1001 (Zschimmer & Schwarz GmbH & Co KG, Lahnstein, Germany) as a deflocculant. Ethanol was used in this case, in order to produce composites with the same processing parameters as those used for RBAO.

4.4.2 Prepreg manufacture by a two-step impregnation process

A two-step impregnation process was then adopted for the manufacture of thermoplastic prepreps, as follows:

- (i) First, a liquid infiltration is conducted by immersing the desized fiber textiles into a liquid slurry of the matrix particles for 20 min. This impregnation step is conducted at room temperature, without any assistance of vacuum or ultrasound. After removing the pre-impregnated fiber fabrics from the liquid slurry, they are placed on a flat, Teflon[®]-coated baking tray and dried for 2 h in a drying cupboard at room temperature.

- (ii) Thermoplastic prepregs are then fabricated by laminating a layer of pre-impregnated fiber textile between two layers of the paraffin based suspension, according to the procedure shown in Figure 30.

The advantage of this two-step impregnation process is that it allows for an enhanced filling of void spaces within the fiber textiles, leading to a more homogeneous matrix distribution within the composite. While the liquid slurry guarantees a good infiltration of the fiber bundles, the paraffin based suspension leads to a better filling of the inter-tow spaces and the crossover voids indicated in Figure 34(b). This enhanced impregnation of fiber fabrics with matrix particles may help reduce the formation of matrix cracks by reducing the matrix shrinkage during debinding and sintering. As mentioned in section 2.2.3, the filling of matrix pockets between fiber tows in order to mitigate the formation of matrix cracks has already been suggested elsewhere [7,13].

In order to prove this two-step impregnation process, an all-alumina composite was produced using an 45 vol% aqueous alumina slurry for the liquid infiltration and a 58 vol% alumina-loaded, paraffin-based suspension for the melt impregnation. Nextel™ 610 fiber woven fabrics were used as reinforcement. Eight prepreg layers were prepared and consolidated by warm pressing as described in section 4.2.4. Debinding and sintering were performed according to the procedure presented in section 4.2.5. Figure 35 shows these processing steps schematically. The microstructure of this composite is shown in Figure 36.

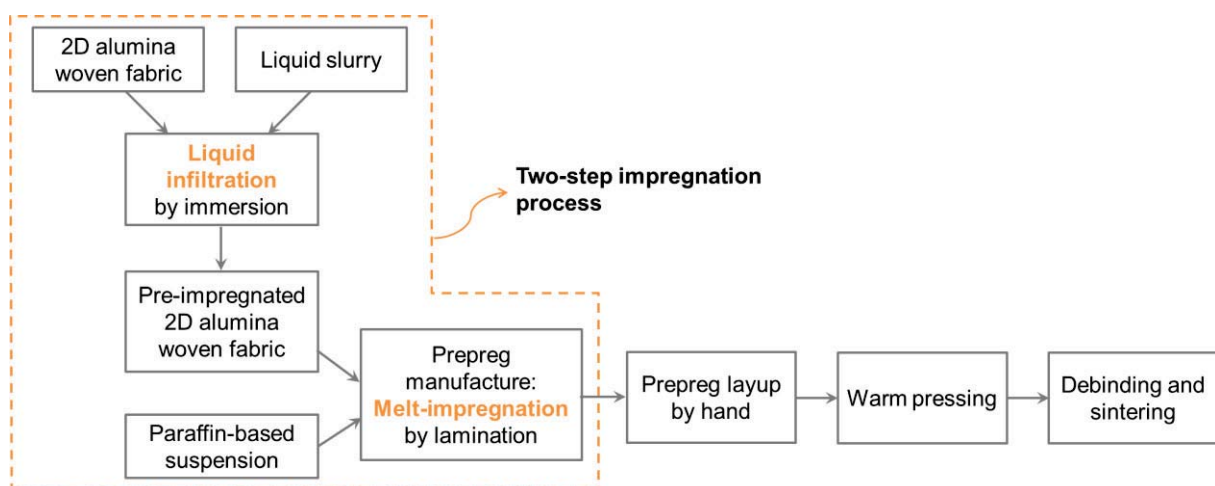


Figure 35: Flowchart of the second concept investigated for composite manufacture: two-step impregnation process.

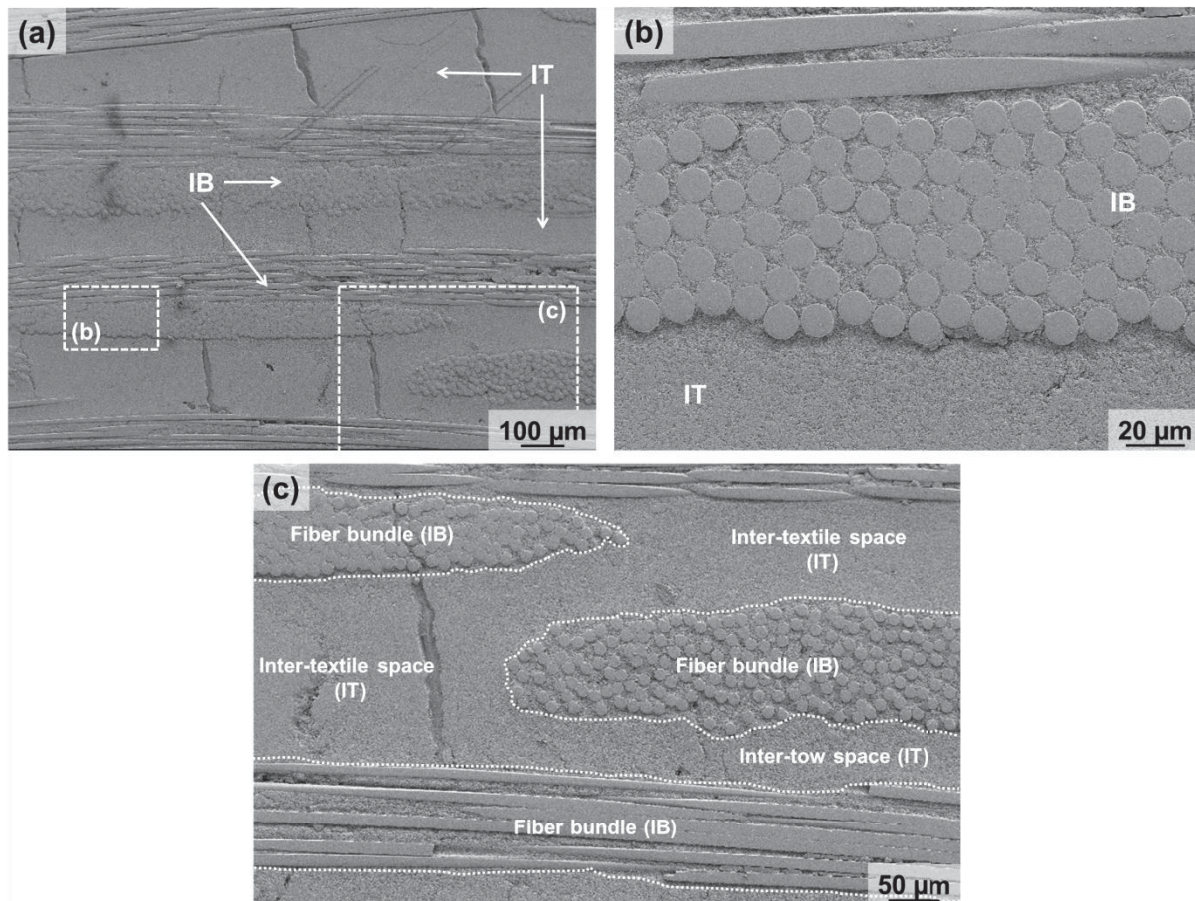


Figure 36: Microstructure of an all-alumina composite manufactured by the two-step impregnation process. The intra-bundle and inter-textile matrices are indicated in the pictures by IB and IT, respectively. Sintering was performed at 1200°C for 30 min.

As indicated in Figure 36, the use of two different suspensions for the manufacture of preregs leads to the formation of two different matrices after composite sintering: an *Intra-Bundle* matrix (IB) resulting from the liquid slurry infiltration and an *Inter-Textile* matrix (IT) originated from the melt impregnation with the paraffin-based suspension. Figure 36(b) clearly shows the boundary between these two composite matrices. Figure 36(c) shows that the IT matrix is not only present between fiber textiles, but also in the inter-tow spaces within a layer of fiber fabric. A better analysis of these two matrices and the possible influence they have on the composite mechanical properties will be presented in Chapter 5 for the reference A8Z2-matrix composites.

The micrographs shown in Figure 36 prove, once again, the good impregnation of fiber bundles achieved by the liquid infiltration process. Moreover, no delamination occurred in this sample, what indicates a good adhesion between the

pre-infiltrated textiles and the paraffin suspension used for prepreg lamination. In addition, the absence of delamination or joining lines also indicates a very effective adhesion between adjacent prepregs during the consolidation of the green body by warm pressing. The matrix cracks observed in this composite are typical for all-oxide CMCs reinforced with 2D woven fabrics and are formed due to the constrained shrinkage of the matrix during processing, as discussed in section 2.2.3. The shrinkage behavior of the alumina matrix used in this composite as a function of temperature will be discussed in more detail in section 5.3.1.

The novel two-step impregnation route presented here is, therefore, suitable for the manufacture of all-oxide ceramic matrix composites. Nevertheless, the IT matrix layers of the composite shown in Figure 36 were still very thick, which resulted in a low fiber volume content of ~ 22 vol%. The next challenge was, then, to increase this value.

4.5 Concept 3: Modification of the consolidation process to achieve higher fiber contents

4.5.1 Increasing pressure during hot pressing

In a first attempt, the increase in the consolidation pressure during warm pressing was investigated as a means to decrease the thickness of the IT matrix layers and, consequently, to increase the fiber volume content of the composites.

For this analysis, three A8Z2-matrix composites containing 8 prepreg layers in a cross-ply configuration were produced according to the procedure schematically shown in Figure 35. Nextel™ 610 woven fabric, cut into 10 cm x 11 cm pieces, was used as reinforcement. The two-step impregnation was conducted using an ethanol-based slurry containing 37 vol% A8Z2 and a paraffin-based suspension containing 58 vol% A8Z2. Prepregs were laid up by hand and consolidated by warm pressing at 1, 2 or 3 MPa. Debinding and sintering were conducted according to section 4.2.5. The fiber volume content of the sintered composites was measured using Eq. 21.

Results showed that this approach was not successful in increasing the fiber volume content of the composites. Fiber volume fractions of ~ 17 , ~ 16 and ~ 17 vol% were obtained for samples consolidated at 1, 2 and 3 MPa, respectively.

Therefore, the consolidation pressure did not have a significant influence on the fiber volume content achieved in these composites. In fact, this is in agreement with Åström [93], who mentioned that pressures higher than 1 MPa do not improve the consolidation of stacks of melt-impregnated prepregs. Additionally, it was observed, in this work, that pressures in excess of 1 MPa tend to radially bow the fiber bundles in a direction perpendicular to the force application, detrimentally affecting fiber orientation.

4.5.2 Consolidation of prepreg stacks by lamination

An alternative presented in the literature for the consolidation of melt-impregnated prepreg stacks is the use of a DBP [93–95]. Again, this was reproduced in a lab scale by the lamination procedure shown in Figure 30(c) and (d). For that, pairs of prepregs were stacked in a cross-ply configuration and consolidated by lamination. These prepreg pairs were then laminated together, until the desired number of prepregs was achieved.

In order to prove this concept, an A8Z2-matrix composite was manufactured according to the procedure schematically shown in Figure 37. Again, 8 prepreg layers were used in a cross-ply configuration. Prepreg manufacture, debinding and sintering were carried out as described in section 4.5.1. Warm pressing at 0.5 MPa was used in this case for shaping the consolidated composite laminate to a flat, plan-parallel plate.

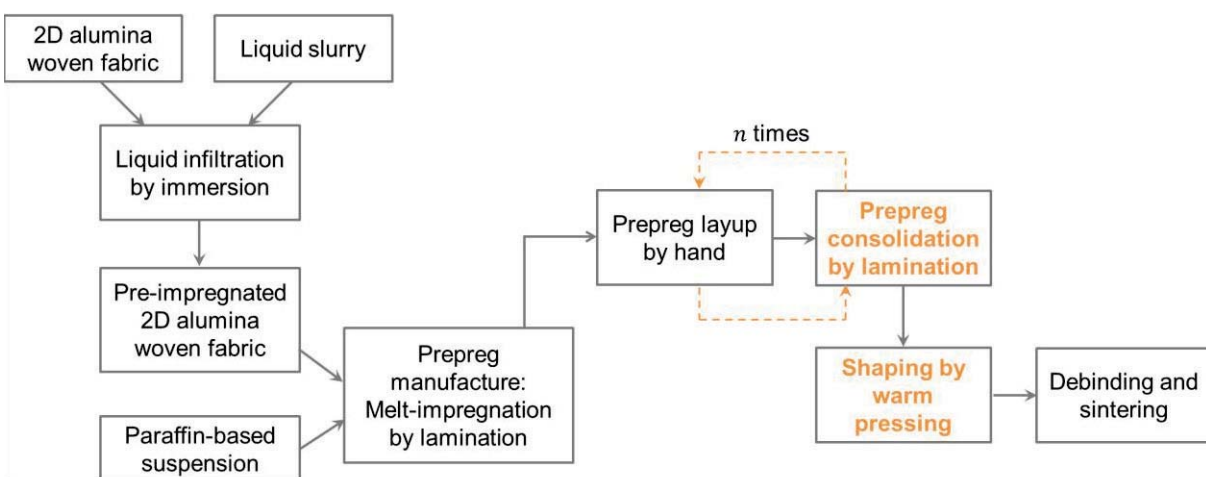


Figure 37: Flowchart of the third concept investigated for composite manufacture: prepreg consolidation by lamination to increase composite fiber volume fraction.

This lamination procedure was successful in increasing the fiber volume content of the composite to ~37 vol%, a twofold increase in relation to those consolidated by warm pressing. A comparison between the microstructures of the composite consolidated by warm pressing at 2 MPa and that consolidated by lamination is shown in Figure 38. This increase in the fiber volume content was possible because, during the consecutive lamination steps used for the consolidation of the composites shown in Figure 38(b), the excess of paraffin-based suspension in single prepregs could be squeezed out of the laminate (see Figure 39), thereby decreasing the thickness of the IT matrix layers between the fiber fabrics. The microstructure of the A8Z2-matrix composite shown in Figure 38(b) will be discussed in more detail in Chapter 5.

The fiber volume content achieved by lamination (~37 vol%) is in the range of those reported in the literature (see Table 2) and is considered reasonable for the all-oxide composites produced in this work. Although this value can vary slightly among different composite plates due to the manual lamination procedure, the present form of the processing route is considered suitable to manufacture all-oxide composites for subsequent characterizations. In the next section, the established processing route is summarized and compared to other state of the art routes available for all-oxide CMCs.

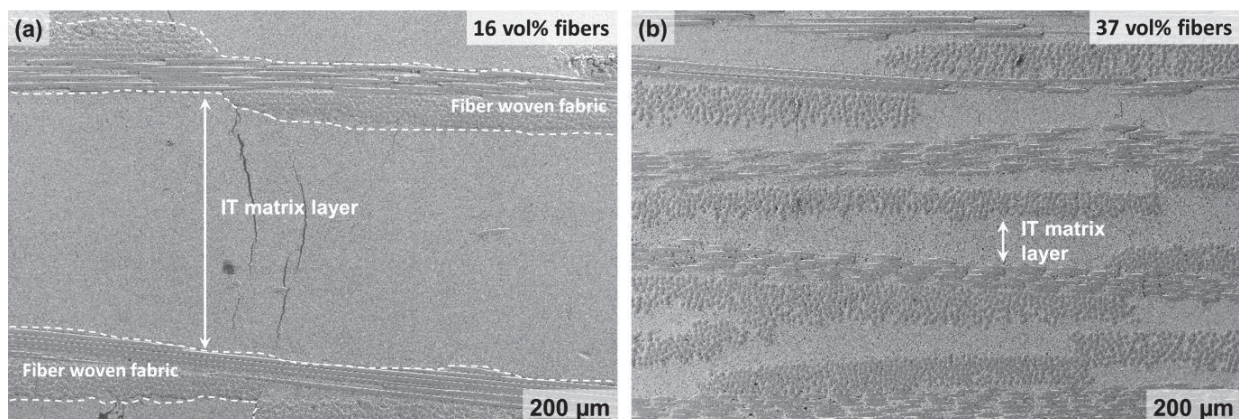


Figure 38: Microstructure of two A8Z2-matrix composites: (a) consolidated by warm pressing at 2 MPa; (b) consolidated by lamination. Composites were sintered at 1200°C for 30 min. Both pictures were taken with the same magnification.

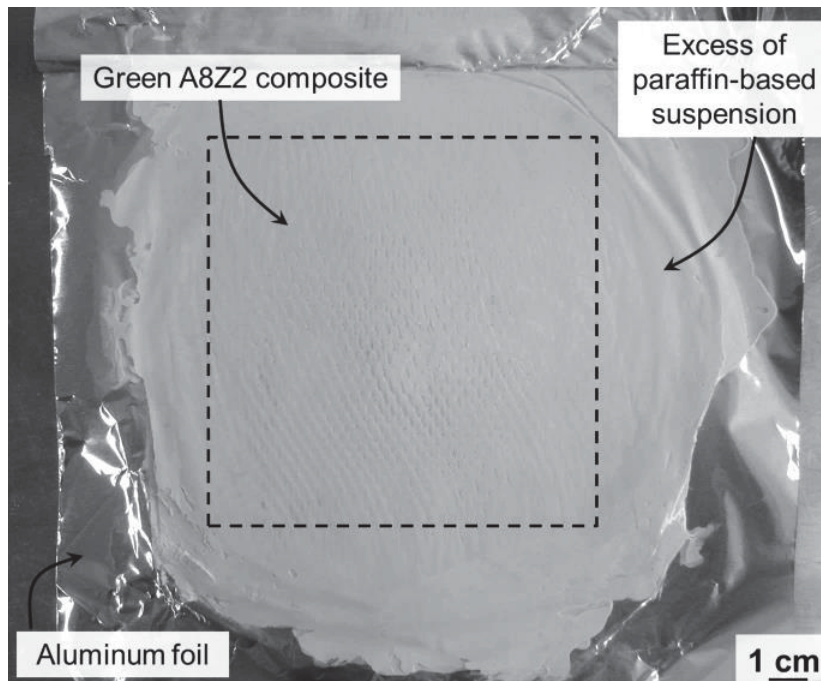


Figure 39: Green A8Z2-matrix composite showing the excess of paraffin-based suspension which is squeezed out during the consecutive lamination steps.

4.6 Established Processing Route

The novel processing route established in this work to manufacture all-oxide CMCs is presented in Figure 40.

This route is basically a combination of conventional powder metallurgy techniques and concepts of the prepreg technology, typically used for the production of polymer matrix composites. Briefly, it comprises the following steps:

- (i) *Liquid infiltration*: infiltration of commercial alumina fiber fabrics (2D Nextel™ 610) with an ethanol-based slurry of the matrix material;
- (ii) *Melt-impregnation*: lamination of the pre-infiltrated fiber fabrics with a paraffin-based suspension for the fabrication of thermoplastic prepregs;
- (iii) *Layup* of prepregs by hand;
- (iv) *Consolidation* of the prepreg stack by lamination;
- (v) *Thermoforming*: if applicable, shaping by warm pressing;
- (vi) *Debinding and sintering* for the consolidation of the ceramic matrix.

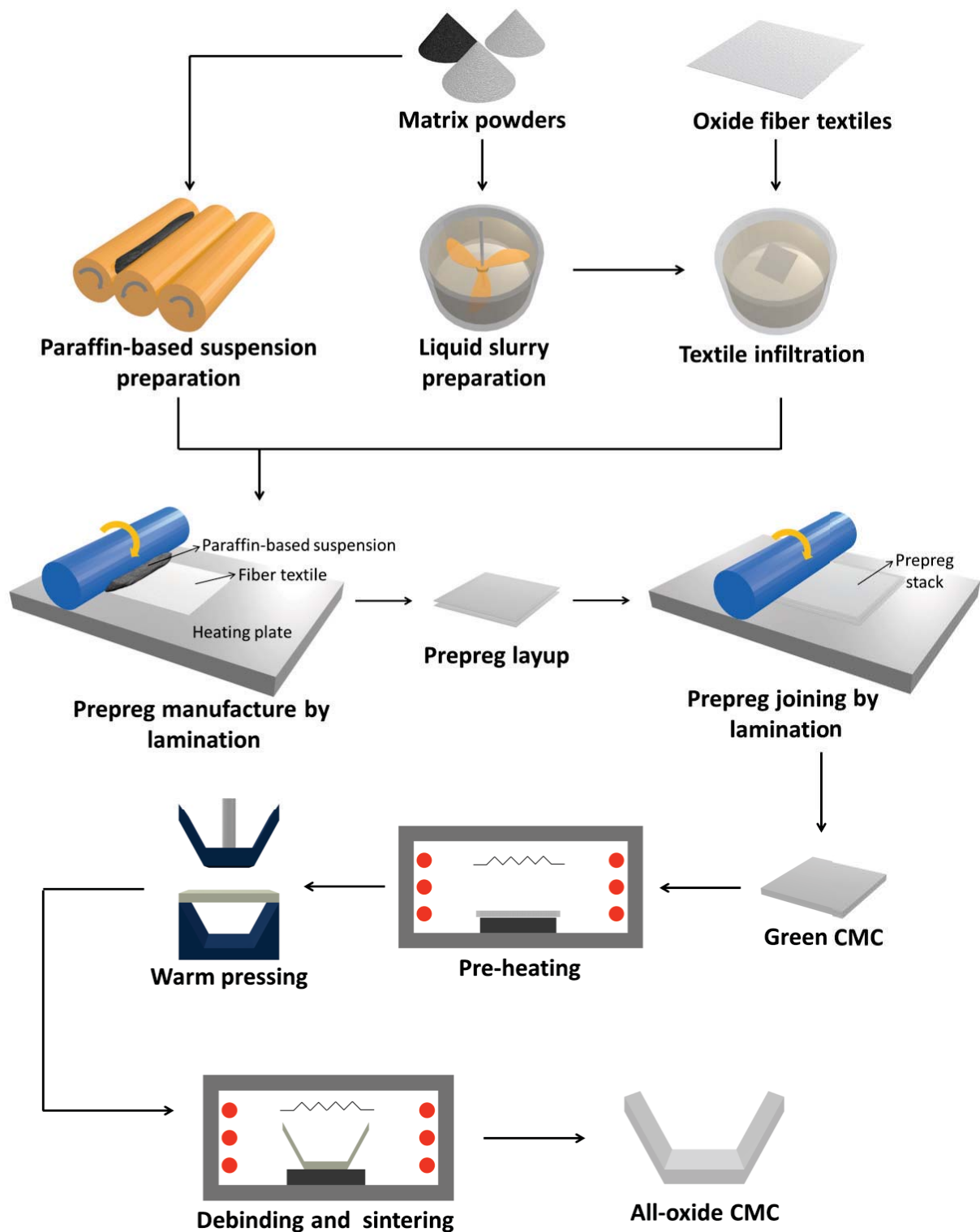


Figure 40: Novel processing route developed in this work for the manufacture of all-oxide composites.

The two-step impregnation process used in this novel route allows for an enhanced filling of the available void spaces in the fiber textiles, resulting in a more homogenous particle distribution and higher matrix green densities in comparison to those attained by conventional liquid infiltration routes. This has at least two

consequences: (i) unlike other processing routes [7,98], no reinfiltration cycles are needed here for the strengthening of the matrix, and (ii) the better filling of fabric free spaces may help reduce the formation of matrix cracks due to the lower shrinkages associated with higher matrix green densities. The latter will be discussed in more detail in Chapter 5.

Since both suspensions used in this two-step impregnation process are based on organic media (ethanol and paraffin), the processing route shown in Figure 40 is suitable for reactive RBAO matrices. Additionally, the resulting thermoplastic prepregs are stable and easy to handle at room temperature, besides presenting post-processing thermoformability, which makes it possible to shape or even weld different CMC parts together. This was proved by preliminary tests of shaping and joining, whose results are shown in Figure 41. The sintered all-oxide composite parts shown in Figure 41(a) and (b) were both produced out of flat prepregs or consolidated green laminates.

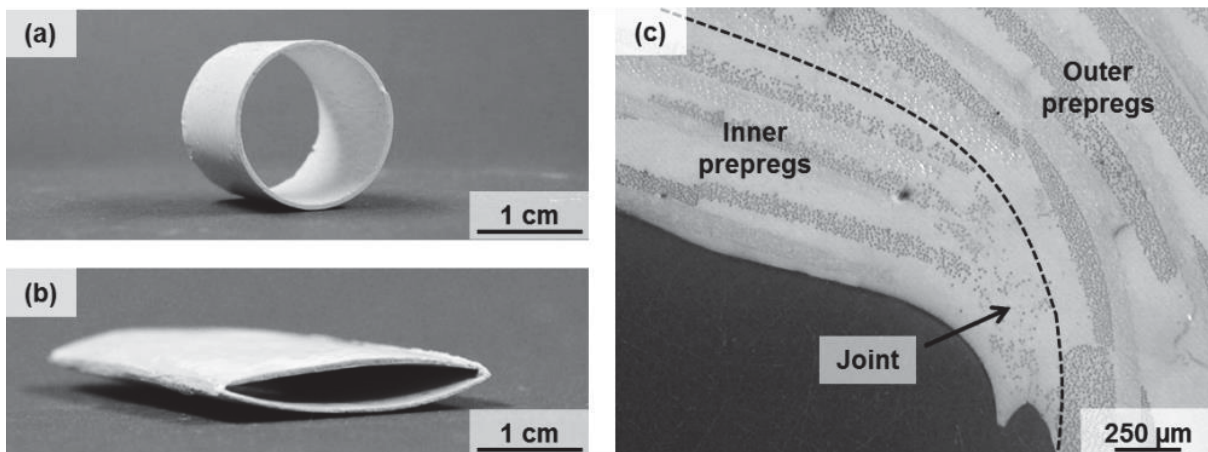


Figure 41: Preliminary tests of shaping and joining: (a) cylinder produced by a tape-laying technique according to [93]; (b) CMC part produced by the compression molding of two flat consolidated laminates, with subsequent joining by fusion bonding; (c) cross section of a joint (optical microscopy).

4.7 Conclusion

A novel route based on the lamination of thermoplastic prepregs was developed and successfully applied to produce multilayered all-oxide composites, reinforced with 2D fiber woven fabrics. Besides being suitable for the RBAO matrix, this route offers the possibility of shaping and joining different CMC parts in the green state, due to the thermoplastic behavior of the prepregs used. This novel route



enables the production of composites with homogenous microstructures and a reasonable fiber volume fraction (>30 vol%). No delamination was observed after debinding or sintering, which indicates the effective joining of the different prepreg layers during the consolidation of the composites. A more detailed analysis of the microstructure and mechanical behavior of all-oxide composites produced via this novel route is presented in the next chapters.





5 A8Z2-matrix CMCs: matrix characterization and predictions of crack deflection

5.1 Introduction

Before investigating the use of RBAO matrix on full-scale composites, a more detailed microstructural analysis of reference all-oxide CMCs produced by the novel lamination route is presented in this chapter⁹. A8Z2-matrix composites are produced and investigated after three different heat treatments:

- (i) as-sintered at 1200°C (AZ-12AS);
- (ii) as-sintered at 1300°C (AZ-13AS);
- (iii) sintered at 1200°C, with subsequent ageing at 1100°C for 500 h (AZ-12AG).

These heat treatments were selected according to results shown in Chapter 3 for the model RBAO-matrix composites: 1200°C is the standard sintering temperature when working with Nextel™ 610 fibers; 1300°C causes fiber grain coarsening, but the weak fiber-matrix interfaces still enable toughening mechanisms; ageing is performed to assess the influence of long-term temperature exposure on the resulting microstructure and mechanical properties of the composites.

All-oxide composites manufactured by the novel lamination route shown in Figure 40 may be interpreted as multilayered ceramics. The two-step impregnation process used for the manufacture of thermoplastic prepregs leads not just to the formation of fiber-matrix interfaces, but also to the formation of interfaces between the two different composite matrices, IB and IT. As will be shown in this chapter, these matrices differ slightly in their porosity, which leads to different properties,

⁹ The results presented in this chapter have been published to a great extent in the journal article “Microstructure and flexural properties of multilayered fiber-reinforced oxide composites fabricated by a novel lamination route” in the journal *Ceramics International* [99]. Copyright 2015 by Elsevier. The material from this article is reused in this thesis with permission.



even though they have the same chemical composition. Considering this, it may be possible that matrix cracks not only deflect at fiber-matrix interfaces, but also at the interfaces between the IB and IT matrices. This possibility is evaluated here according to the He and Hutchinson diagram [40] for the prediction of crack deflection or penetration at the interface between dissimilar elastic materials (Figure 3). Three different situations are analyzed in this study for composites of each heat-treatment condition:

- (i) cracks propagating from the IT to the IB matrix;
- (ii) cracks propagating from the IB to the IT matrix;
- (iii) cracks propagating from the IB matrix to the fibers (F).

For this purpose, the porosity of the IB and IT composite matrices are measured via image analysis after each heat treatment, and the results are used to estimate their elastic modulus E and fracture toughness K_{IC} , according to property-porosity relationships obtained for monolithic A8Z2 matrix samples. The obtained values of E and K_{IC} are then used to calculate the toughness ratio and elastic mismatch parameter for the different situations described above. These values are plotted together with the He and Hutchinson diagram, so that crack deflection/penetration can be predicted for each situation. These predictions help to better understand the mechanical properties of these composites, which will be presented in Chapter 7.

5.2 Methods

5.2.1 Preparation and characterization of A8Z2 monolithic samples

Bar-shaped (40 mm × 5 mm × 4 mm), monolithic samples were prepared by uniaxially pressing (WCH 10, P/O/Weber, Germany) 3 g of the A8Z2 powder at 15 MPa for 30 s, with subsequent cold isostatic pressing (KIPP 200ES, P/O/Weber, Germany) at 300 MPa for 2 min. Samples were sintered according to the heating cycle shown in Figure 18 at different temperatures from 1100°C to 1500°C, with a 100°C interval. The sintered samples were then ground to a cross-section of approximately 3 mm × 4 mm using a flat bed grinding machine (HFS204, Blohm, Hamburg, Germany), so that plan-parallel faces were obtained. Specimens were polished to 1 μm finish on one of the 40 mm × 3 mm faces for subsequent characterizations.

The density ρ_s of the monolithic A8Z2 samples sintered at different temperatures was measured geometrically. Porosity was then calculated by Eq. 12, using a value of $\rho_t = 4.50 \pm 0.01 \text{ g/cm}^3$, measured for the sintered A8Z2 loose powder by He-pycnometry (AccuPyc II 1340, Micromeritics, Aachen, Germany).

Fracture toughness K_{IC} and elastic modulus E of the monolithic A8Z2 samples were characterized by the SEVNB and nanoindentation techniques, respectively, according to the procedure described in section 3.2.5 for the monolithic RBAO samples. The K_{IC} and E data were fitted using Eq. 17 and Eq. 18, respectively, so as to estimate these two properties as a function of A8Z2 matrix porosity.

In order to investigate the shrinkage of the A8Z2 matrix as a function of temperature, a green monolithic sample was ground to smaller dimensions (12 mm x 4 mm x 4 mm) and analyzed by dilatometry (DIL 402 PC, Netzsch, Selb, Germany). For the sake of comparison, a pure alumina matrix sample (Ceralox HPA 0.5, RWE-DEA, Hamburg, Germany) was investigated under the same conditions. Samples were heated to 1500°C following the heating rates presented in Figure 18, and held at this temperature for 2 h. Cooling was performed at 10°C/min.

5.2.2 Composite production and characterization

A8Z2-matrix composites were produced using the novel lamination route presented in section 4.6. Nextel™ 610 woven fabric, cut into 10 cm × 11 cm pieces, was used as reinforcement. An ethanol-based slurry, containing 32 vol% solids, was used for the liquid infiltration of fiber bundles, while a paraffin-based suspension, containing 58 vol% solids, was used for the manufacture of prepregs by lamination. After consolidating a cross-ply laminate containing eight prepregs, debinding was conducted according to the heating cycle shown in Figure 31. Sintering was performed in air, in a box furnace, following the heating rates shown in Figure 18. Composites AZ-12AS and AZ-13AS were sintered for 30 min at 1200°C and 1300°C, respectively. Composite AZ-12AG was aged in a box furnace at 1100°C for 500 h, after sintering at 1200°C for 30 min.

After sintering, samples were prepared for SEM investigation, according to the procedure described in section 4.2.7. Fiber volume fraction of the different composites was determined using Eq. 21. Porosity of the IB and IT matrices was



determined by image analysis of SEM micrographs using the softwares GIMP (Version 2.8, GNU Image Manipulation Program) [100] and ImageJ (Version 1.47v, Image Processing and Analysis in Java) [101]. GIMP was used to convert the SEM image into 8-bit and to cut the SEM legend bar off the picture. The image was then binarized using ImageJ and porosity was calculated as the ratio between the area of pores and the total area of the image. At least three pictures (at 35000× magnification) of each matrix were analyzed.

5.2.3 Theoretical prediction of crack deflection/penetration

The He and Hutchinson diagram, shown in Figure 3, is not only valid for fiber-reinforced ceramics, but can be used in any situation in which a crack is propagating through two dissimilar elastic materials, such as in multilayered ceramics [51]. Considering two dissimilar elastic materials, 1 and 2, and a crack propagating in material 1 and impinging on the interface between material 1 and material 2, the elastic mismatch parameter presented in Eq. 5 can be rewritten in a more generalized form as follows:

$$\alpha' = \frac{(E_2 - E_1)}{(E_2 + E_1)} \quad \text{Eq. 22}$$

where E_1 and E_2 are the elastic moduli of material 1 and 2, respectively. Crack deflection at the interface between materials 1 and 2 is expected to occur when $\Gamma_i/\Gamma_2 < G_d/G_p$, where Γ_i is the toughness of the interface and Γ_2 is the toughness of material 2, on which the crack is impinging.

As mentioned previously, three different crack propagation situations are analyzed in this work for the different A8Z2-matrix composites produced here: (i) cracks propagating from IT to IB, (ii) from IB to IT and (iii) from IB to the fibers (F). Consequently, material 1 can be, in this case, either the IB or the IT matrix, while material 2 can be one of these matrices or a fiber (see schematics in Figure 47). In a conservative estimate, the toughness of the interface Γ_i can be considered equal to the toughness of material 1, in which the crack is propagating, so that $\Gamma_i/\Gamma_2 = \Gamma_1/\Gamma_2$. Therefore, crack deflection is expected when $\Gamma_1/\Gamma_2 < G_d/G_p$.

Based on the porosity values measured by image analysis, E and K_{IC} of the IB and IT matrices were estimated using the property-porosity relationships obtained for

the monolithic A8Z2 matrix samples (using Eq. 18 and Eq. 17). Values of E and K_{IC} of the alumina fiber are taken from the literature to be 380 GPa [58] and $3.68 \text{ MPa}\sqrt{m}$ [88], as discussed in section 3.3. Toughness of fiber and matrices are calculated according to Eq. 15. The values obtained for the elastic mismatch parameter α' and the toughness ratio Γ_1/Γ_2 for each crack propagation condition analyzed here are, then, plotted together with the He and Hutchinson diagram, so that crack deflection or penetration into the interfaces of the different composites can be predicted. Changes in the fiber properties due to processing and thermal treatments were not considered in this analysis.

5.3 Results

5.3.1 A8Z2 matrix properties

The variation of E and K_{IC} as a function of porosity for the monolithic A8Z2 matrix samples are presented in Figure 42 and Figure 43 respectively.

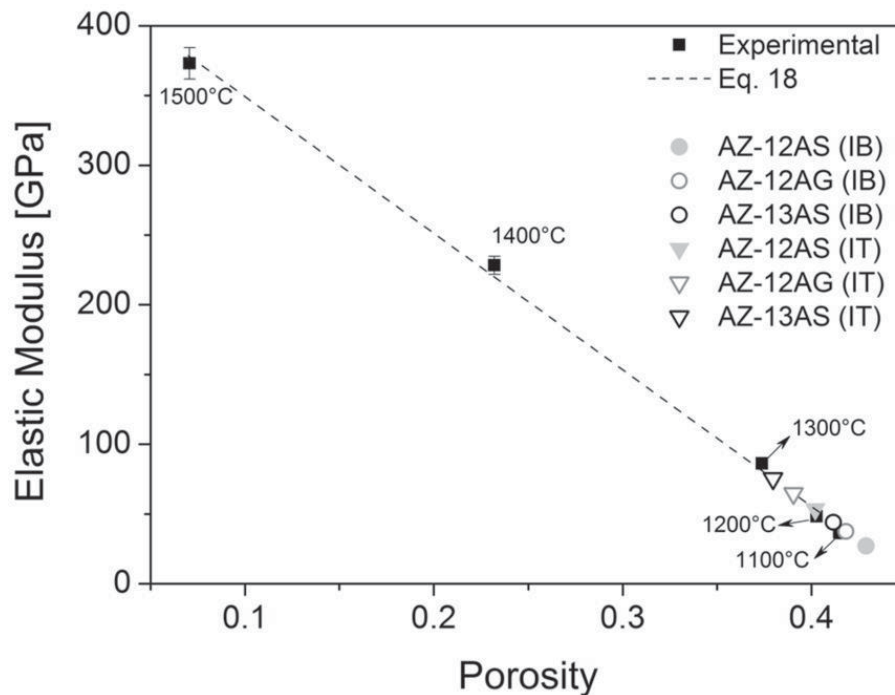


Figure 42: Elastic modulus E as a function of porosity for monolithic A8Z2 matrix samples sintered at different temperatures, as indicated. Experimental values (squares) were obtained by nanoindentation. Values of E estimated for the different composite matrices using Eq. 18 with $E_0 = 447.17 \text{ GPa}$ and $\kappa = 2.19$ are also presented (circles and triangles).

Porosity values varied from $41.5 \pm 0.3\%$ to $37.4 \pm 0.3\%$ for sintering temperatures between 1100°C and 1300°C , respectively. At higher temperatures, porosity decreases considerably, achieving values of $23.2 \pm 0.7\%$ at 1400°C and $7.1 \pm 0.1\%$ at 1500°C . Elastic modulus varied from 36.9 ± 4.8 GPa to 373.02 ± 11.32 GPa for sintering temperatures of 1100°C and 1500°C , respectively. The linear fitting according to Eq. 18 resulted in $E_0 = 447.17$ GPa and $\kappa = 2.19$.

K_{IC} increased from 0.3 ± 0.03 $\text{MPa}\sqrt{\text{m}}$ to 4.3 ± 0.1 $\text{MPa}\sqrt{\text{m}}$ for sintering temperatures of 1100°C and 1500°C , respectively. The linear fitting, according to Eq. 17, resulted in $K_0 = 5.05$ $\text{MPa}\sqrt{\text{m}}$ and $a = 2.24$.

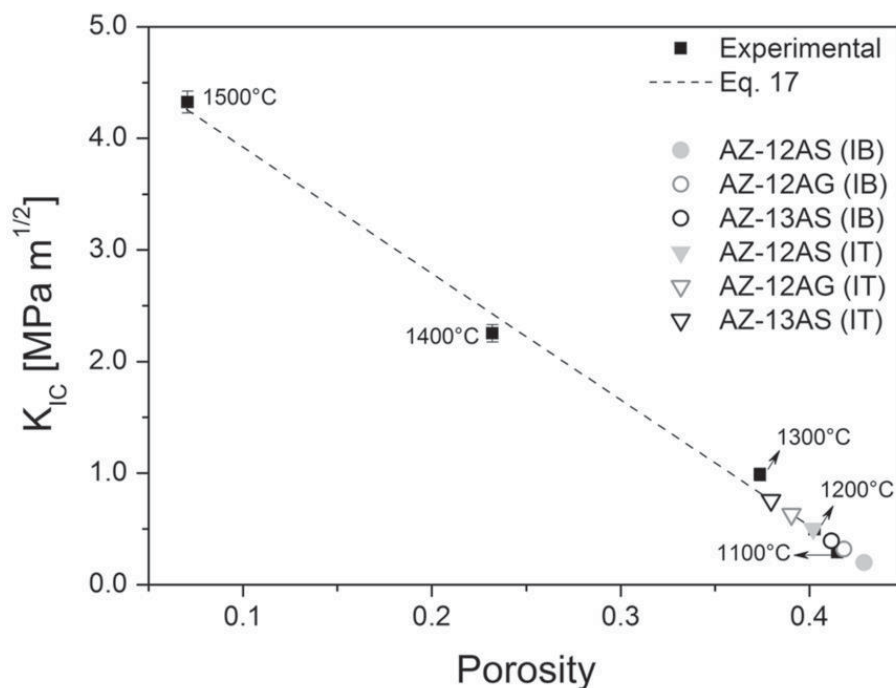


Figure 43: Fracture toughness K_{IC} as a function of porosity for A8Z2 monolithic matrix samples sintered at different temperatures, as indicated. Experimental values (squares) were obtained by the SEVNB technique. Values of K_{IC} estimated for the different composite matrices using Eq. 17 with $K_0 = 5.05$ $\text{MPa}\sqrt{\text{m}}$ and $a = 2.24$ are also presented (circles and triangles).

The variation of linear shrinkage (LS) and linear shrinkage rate (LSR) as a function of temperature for the A8Z2 and pure alumina matrices is shown in Figure 44. The pure alumina matrix starts to shrink $\sim 200^\circ\text{C}$ earlier than the A8Z2 matrix. While the LSR starts to increase at $\sim 906^\circ\text{C}$ for pure alumina, the onset of densification of the A8Z2 matrix occurs at $\sim 1100^\circ\text{C}$ (Figure 44(b)).

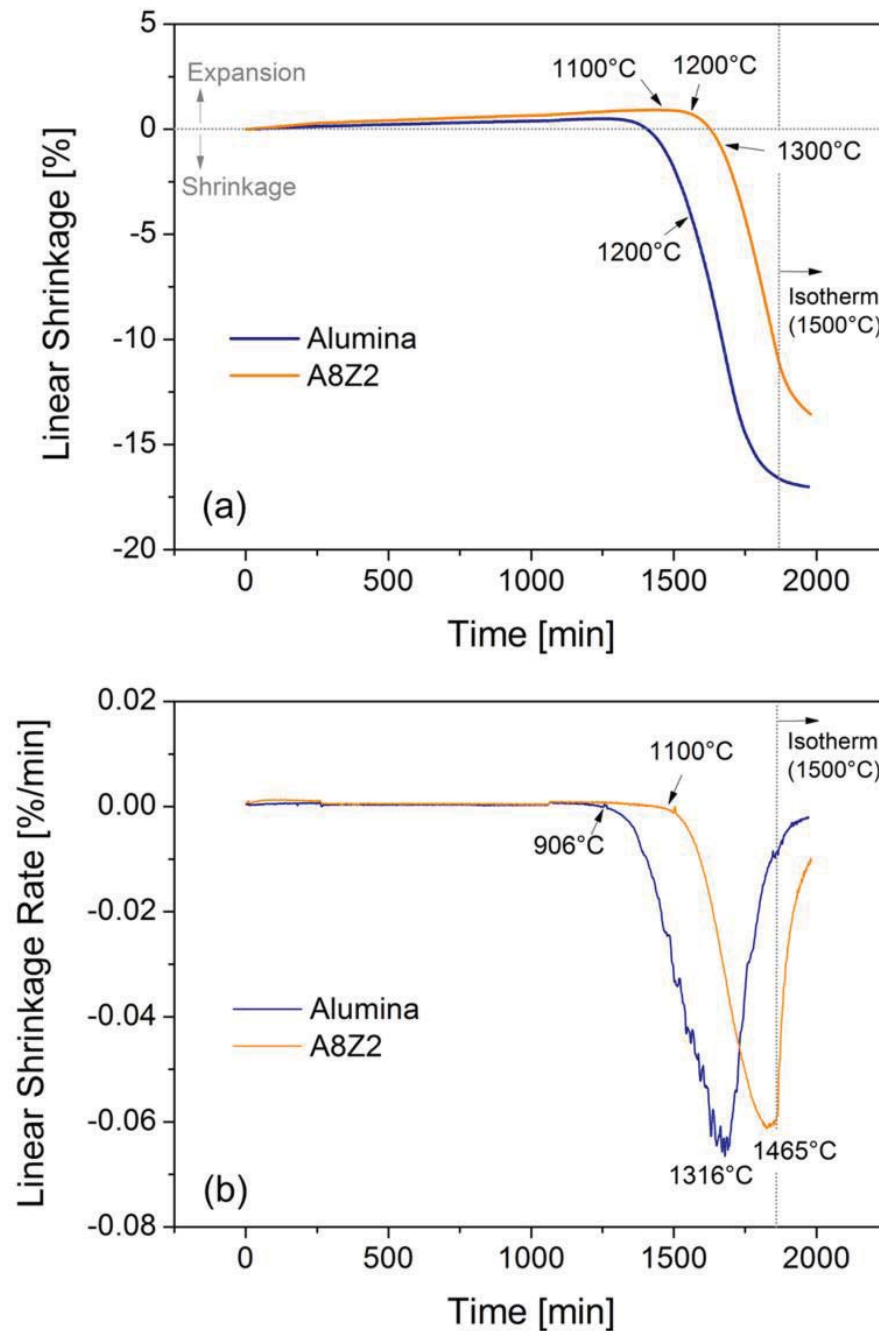


Figure 44: Dilatometric investigation of the A8Z2 matrix, compared with a pure alumina sample: (a) linear shrinkage (LS) and (b) linear shrinkage rate (LSR). Data acquisition started at 35°C.

At 1200°C, LS is ~4.3% for pure alumina (Figure 44(a)), while the A8Z2 matrix has still an apparent expansion of +0.7%. This means that, at this temperature, the shrinkage endured by the A8Z2 matrix did not completely compensate for its thermal expansion. A value of $9.84 \times 10^{-6} \text{ } ^\circ\text{C}^{-1}$ was measured for the linear coefficient of thermal expansion (CTE) of the A8Z2 matrix using the cooling data from 1400°C to 200°C. Considering this value as a constant over the whole temperature range, shrinkage values of ~0.4% and ~2% can be estimated for the



A8Z2 matrix after cooling from 1200°C and 1300°C, respectively, to room temperature. These values are very low in comparison to the pure alumina, which shrinks ~10% at 1300°C. Pure alumina has a maximum LSR at 1316°C. Above this temperature, LSR starts to decrease, which indicates the beginning of the final sintering stage. The maximum LSR of the A8Z2 matrix occurs at 1465°C for the sintering cycle used in this dilatometric analysis. It appears, however, that this value could be higher if the sample had been heated to higher temperatures. The decrease in LSR of the A8Z2 matrix seems to be more related here with the beginning of the temperature plateau at 1500°C than with the initiation of the final sintering stage. After two hours at 1500°C, LS values of approximately 17% and 13% were measured for the alumina and A8Z2 matrices, respectively.

5.3.2 Microstructural analysis of A8Z2-matrix composites

Microstructures of composites submitted to the different heat-treatments analyzed in this work are presented in Figure 45. The matrices resulting from the two suspensions used in the composite production (ethanol and paraffin-based) are indicated by IB and IT, respectively. All composites present homogeneous microstructures with only a few shrinkage-related, through-thickness cracks. Again, no delamination was detected, indicating a very effective adhesion between adjacent prepregs during the manufacturing process. A fiber volume fraction of approximately 37 vol% was measured for the composite AZ-12AS, whereas a value of ~40 vol% was measured for both AZ-13AS and AZ-12AG.

In most of the cases, the bonding between the IB and IT matrices exhibits a visible interface, as indicated in Figure 46(a). Figure 46 (b) and (c) show higher magnification pictures of both matrices. They differ slightly in their porosities, being the IB matrix more porous than the IT.

Table 4 presents the porosity values measured for the different matrices by image analysis. A slight decrease in porosity was observed in both IB and IT matrices of the aged sample (AZ-12AG) in relation to its as-sintered counterpart (AZ-12AS), indicating matrix densification during ageing. Values of E and K_{IC} estimated for these matrices using Eq. 18 and Eq. 17 are shown in Figure 42 and Figure 43, respectively.

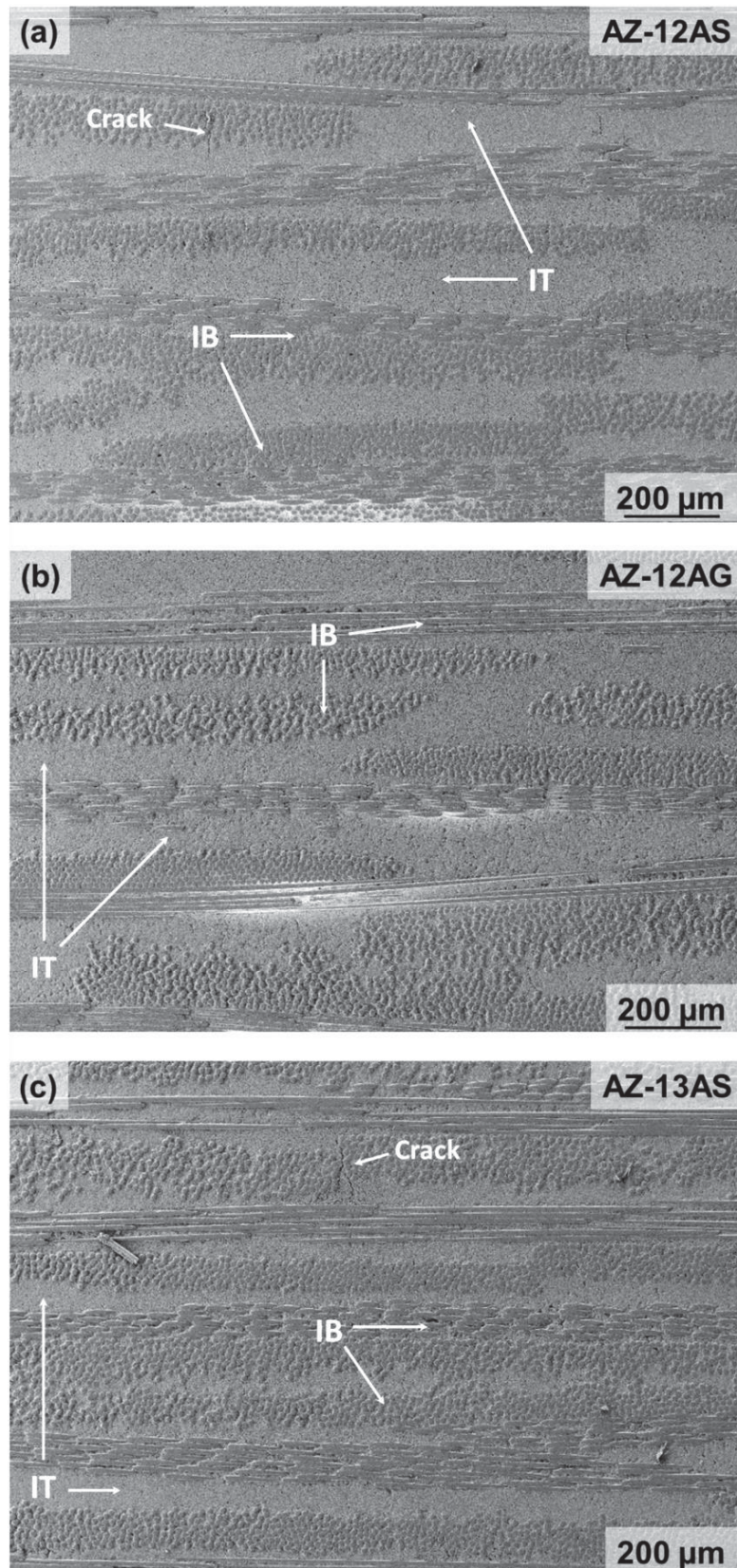


Figure 45: Microstructures of A8Z2-matrix CMCs produced by the novel lamination route: (a) sintered at 1200°C; (b) sintered at 1200°C and aged at 1100°C for 500 h; (c) sintered at 1300°C. IB and IT indicate the intra-bundle and inter-textile matrices, respectively.

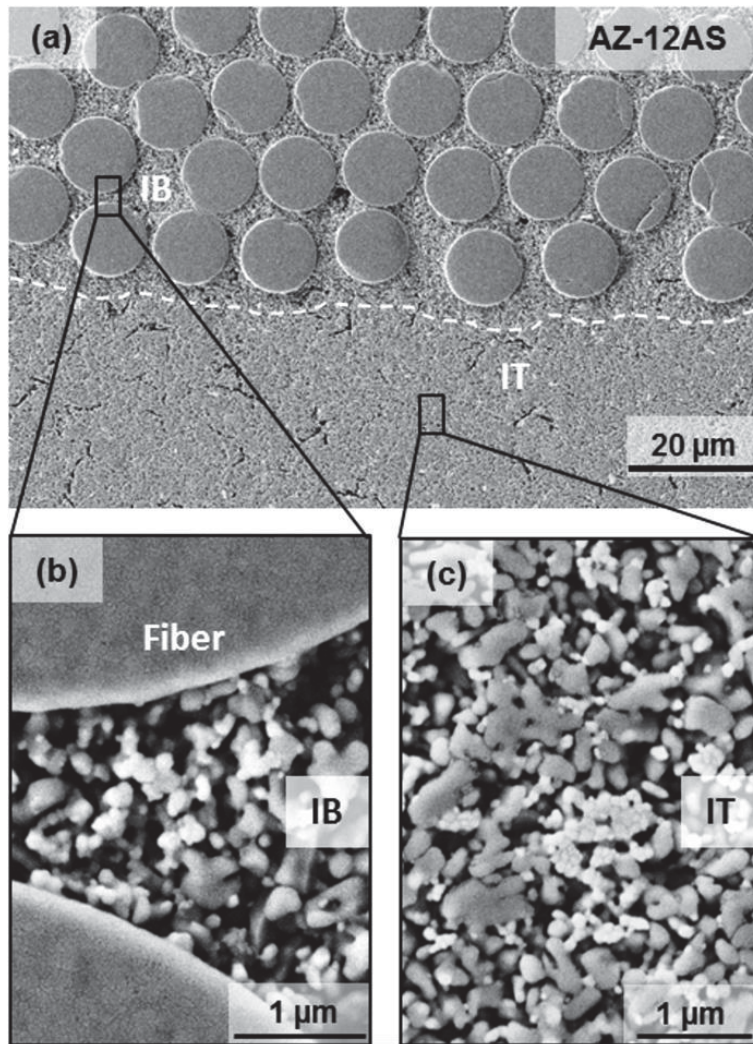


Figure 46: Microstructure of a composite sintered at 1200°C and its respective porous matrices: (b) intra-bundle (IB) and (c) inter-textile (IT). The dashed line in (a) indicates the location of the interface between IB and IT. The black areas in (b) and (c) are pores in the matrices.

Table 4: Porosity of the IB and IT matrices of the different A8Z2-matrix composites

Composite	Porosity	
	IB matrix	IT matrix
AZ-12AS	42.9 ± 1.1	40.2 ± 0.3
AZ-13AS	41.2 ± 0.2	37.9 ± 2.3
AZ-12AG	41.8 ± 2.2	39.1 ± 0.3

5.3.3 Theoretical predictions of crack deflection/penetration

Figure 47 shows the prediction for deflection/penetration of cracks propagating in the IB or IT matrices and impinging on different interfaces of the A8Z2-matrix composites. The indexes 1 and 2 designate, respectively, the matrix in which the crack is propagating and the material on which the crack is impinging, as schematically shown in the insets in Figure 47.

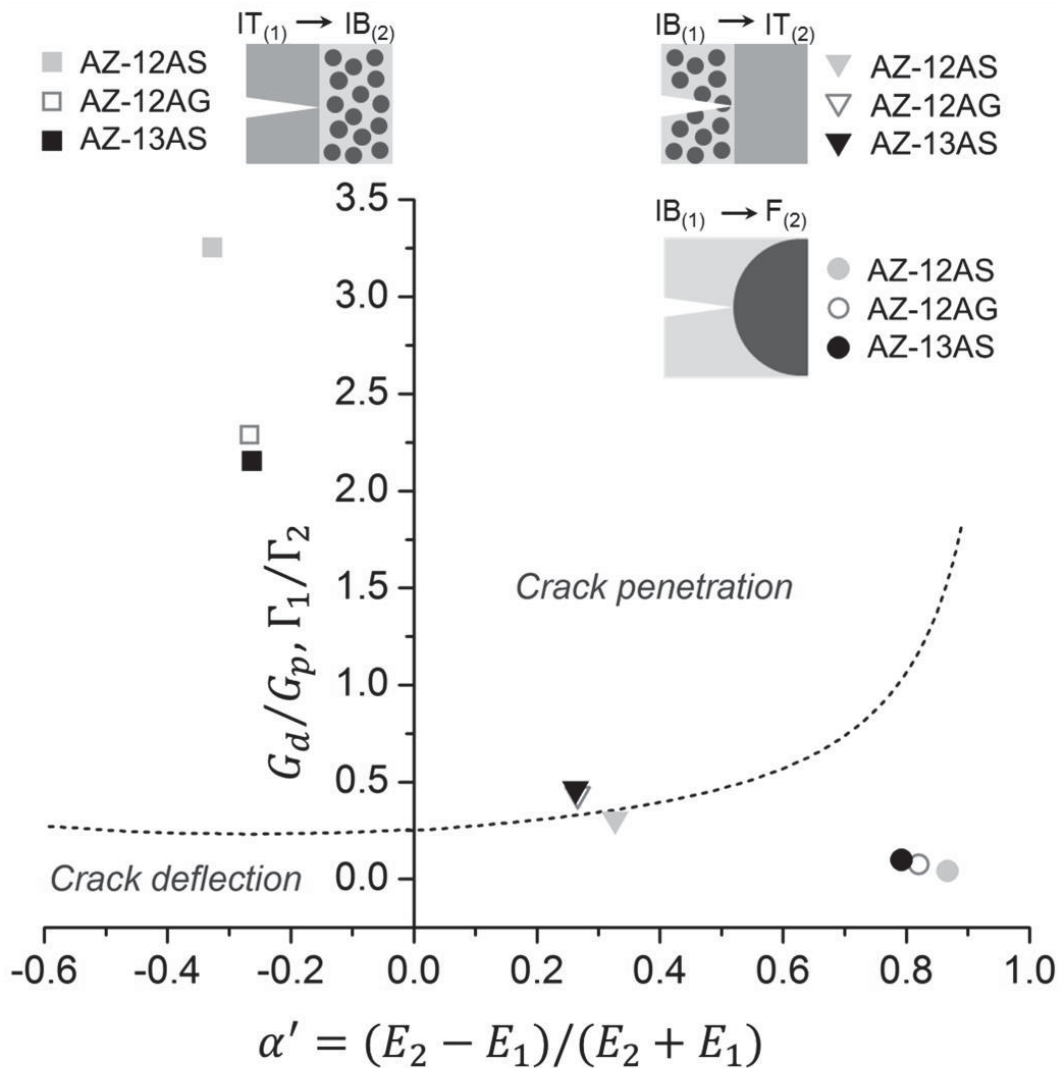


Figure 47: Ratio of energy release rates G_d/G_p associated with crack deflection and penetration at the interface between two dissimilar elastic materials, according to He and Hutchinson [40] (dotted line). Experimental data obtained in this work for α' and Γ_1/Γ_2 is superimposed in this diagram (symbols). Different situations are considered, for cracks propagating either in the IB or IT matrix and impinging on different interfaces of the A8Z2-matrix composites, as schematically shown in the insets. The indexes 1 and 2 indicate the material in which the crack is propagating and the material on which the crack is impinging, respectively. Experimental data is obtained considering $\Gamma_i = \Gamma_1$.



The results shown in this diagram suggest that:

- (i) Cracks propagating from the IB matrix to the fibers (circles in Figure 47) are expected to deflect at the fiber-matrix interfaces in all cases;
- (ii) Cracks propagating in the IT matrix will always penetrate in the IB matrix (squares in the left-hand side of Figure 47);
- (iii) The elastic mismatch (α') between the IB matrices and fibers decreases in the direction of AZ-12AS \rightarrow AZ-12AG \rightarrow AZ-13AS. This indicates a strengthening of the matrices and consequently of the interfaces in the same direction;
- (iv) Analyzing cracks propagating from IB \rightarrow IT and from IB \rightarrow F (right-hand side of the diagram), an embrittlement is expected in the direction AZ-12AS \rightarrow AZ-12AG \rightarrow AZ-13AS, since matrix densification leads to lower values of α' and higher values of toughness ratio;
- (v) In the AZ-12AS composite, a crack propagating in the IB matrix may be deflected at the interface with the IT matrix, which is not the case for the other heat treatment conditions. This is, however, a critical affirmation, since the data points presented in Figure 47 may not be precise enough to distinguish between deflection and penetration of cracks propagating from IB to IT in the different composites. Nevertheless, this prediction will be further considered and the occurrence of such deflection/penetration will be verified in Chapter 7, where the fracture surfaces of these composites are investigated.

5.4 Discussion

Although presenting the same chemical composition after sintering (80 vol% Al_2O_3 and 20 vol% tetragonal ZrO_2), the porosity values of the monolithic A8Z2 matrix samples, shown in Figure 42 and Figure 43, are higher than those of monolithic RBAO samples (see Figure 22) sintered at the same temperatures. This is caused by the higher green densities achieved in pressed RBAO samples, due to the plastic deformation of Al [72]. Additionally, the expansion associated with the oxidation of Al particles during heat treatment may also lead to an enhanced densification [18].

The significant decrease in porosity of the monolithic A8Z2 samples sintered at 1400°C and 1500°C, in comparison to those sintered up to 1300°C, is explained by the larger densification rates (LSR, Figure 44(b)) at temperatures higher than 1300°C.

The porosity of the IB and IT composite matrices are normally higher than their cold isostatic pressed counterparts. On the one hand, this indicates that the green densities achieved by the infiltration or melt impregnation processes are lower than those obtained by pressing. On the other hand, the higher porosities can also be a result of the constrained shrinkage of the matrix due to the non-shrinking network of fibers [23]. Therefore, theoretical analyses of crack deflection based on porosity values of pressed matrix samples, as that presented in Chapter 3, can be considered very conservative, since they assume lower porosity values than those obtained on full-scale CMCs produced via infiltration routes. Nevertheless, as mentioned in section 3.2.3, it offers a good preliminary evaluation for material development.

The small amount of matrix cracks in the A8Z2-matrix composites investigated here (Figure 45) can be attributed to the combination of two effects: (i) the better filling of textile void spaces enabled by the two-step impregnation process used in the novel route and (ii) the low shrinkage endured by the A8Z2 matrix at the composite sintering temperatures. As mentioned previously, in order to mitigate matrix cracks in ceramic matrix composites, both drying and sintering shrinkages should be avoided [10]. It appears, therefore, that both are mitigated in this work, by combining the novel lamination route with the A8Z2 oxide matrix. As shown in Figure 36(c), the paraffin-based suspension fills not only the inter-textile spaces, but also the available inter-tow spaces of the fiber fabrics, which could not be impregnated with the liquid slurry. This guarantees a more homogenous distribution of matrix particles throughout the green composites and, consequently, reduces shrinkage both in the green state and during sintering. Moreover, the alumina-zirconia matrix used presents very low shrinkages up to 1300°C (~2%), which also avoid crack formation during sintering.

The effect of zirconia additions on the sinterability of alumina was investigated by Lange *et al.* [102] and Wang and Raj [103]. Lange *et al.* [102] showed that additions of 10 vol% zirconia delay the onset of densification of alumina by ~100°C. Nevertheless, the reason for this delay was still unknown at that time. Some years



later, Wang and Raj [103] suggested that this delay is caused by an increase in the activation energy of sintering resulting from the addition of zirconia. According to their measurements, pure alumina sinters with an activation energy of 440 ± 45 kJ/mol, while mixtures of alumina and zirconia in the range of 5 to 95 vol% sinter with an activation energy of 700 ± 100 kJ/mol. In this work, a delay of $\sim 200^\circ\text{C}$ was observed for the onset of densification of the A8Z2 matrix in comparison to pure alumina. At 1200°C , alumina shrinks $\sim 4\%$, while A8Z2 shrinks only $\sim 0.4\%$. This larger shrinkage of alumina at 1200°C may explain the larger amount of matrix cracks in the all-alumina matrix composite shown in Figure 36 with respect to the A8Z2-matrix composites shown in Figure 45.

The fact that matrix cracks can be mitigated up to 1300°C using the A8Z2 matrix does not depress the interest in developing RBAO-matrix composites. With the development of new generation, high temperature ($>1300^\circ\text{C}$) oxide fibers in the future, the A8Z2 matrix will not suffice to reduce the formation of sintering-related matrix cracks anymore. As shown in Figure 44, the linear shrinkage of this matrix increases considerably above 1300°C , which will certainly lead to crack formation if composites are to be sintered at these higher temperatures. Therefore, although the A8Z2 matrix can considerably reduce matrix cracking at the maximum sintering temperatures allowed for the currently available Nextel™ fibers, the development of RBAO-matrix composites is still promising. As mentioned previously, the shrinkage of this reactive sintering matrix can, in principle, be tailored to zero for any given sintering temperature. The introduction of RBAO matrix in the novel lamination route is presented in Chapter 6.

Predictions of crack deflection according to the He and Hutchinson diagram suggest that, in addition to crack deflection at fiber-matrix interfaces, matrix cracks may be also deflected at the IB-IT interfaces of the AZ-12AS composite. This could lead to a combination of fracture mechanisms from both fiber-reinforced composites and layered ceramics [50,51], increasing the energy absorption during fracture, thereby increasing the toughness of this material.

In contrast to the theoretical prediction shown in Chapter 3, crack deflection at fiber-matrix interfaces is predicted here also for composites sintered at 1300°C . This is probably a consequence of the higher matrix porosities resulting from the infiltration techniques, in comparison to those obtained by pressing. The

predictions shown in section 5.3.3 are used in Chapter 7, where the mechanical properties of full-scale composites produced with the novel prepreg lamination route are presented.

5.5 Conclusion

Microstructural analysis of the A8Z2-matrix composites produced by the novel prepreg lamination route shows that the different suspensions used in the prepreg manufacture lead to the formation of two different matrices. Porosity of the intra-bundle matrices (IB) is slightly higher than that of inter-textile matrices (IT).

The combination of the two-step impregnation process used in the novel route with the A8Z2 matrix leads to the mitigation of matrix cracks by reducing the shrinkage up to a sintering temperature of 1300°C.

Analysis according to the He and Hutchinson model predict crack deflection at fiber-matrix interfaces for composites submitted to all heat treatments investigated here. In addition, crack deflection is predicted between the IB and IT matrices of the composite sintered at 1200°C.





6 RBAO-matrix CMCs: processing and microstructural features

6.1 Introduction

Reducing the formation of sintering-related matrix cracks in CMCs by using reactive sintering routes is only possible if the composition of the matrix precursor powder is tailored to present low-to-zero shrinkage after sintering at the temperatures of interest. As for the RBAO matrices used in this study, this is done by adjusting the amount of metallic aluminum, so that the shrinkage is compensated by the increase in volume associated with aluminum oxidation.

Initially, it was expected that this compositional adjustment was the only development step missing for the successful production of full-scale, defect-free RBAO-matrix composites. However, as will be reported in this chapter, the introduction of RBAO powder in the novel lamination route originated a new processing challenge, which was not existent in the manufacture of composites with pure oxide matrices: the formation of large voids in the inter-textile (IT) matrix. Therefore, apart from the compositional tailoring to achieve zero shrinkage after sintering, a means to mitigate the formation of these voids should be found.

In this chapter, the additional development steps for the production of full-scale RBAO-matrix composites are presented and discussed. In order to improve the reading comprehension, this chapter is divided into three main sections, each one containing its own experiments, results and discussion segments. These sections are presented in such an order that the results of one section lead to the analyses performed in the subsequent one. Section 6.2 shows the investigation of low-to-zero shrinkage RBAO compositions and presents the problem of void formation. In section 6.3, the possible causes for the void formation are investigated by different characterization methods and the most likely cause is identified. A solution is then proposed, which is used in section 6.4 to manufacture void-free, RBAO-matrix composites.



6.2 Production of low-to-zero shrinkage RBAO-matrix composites

The composite matrices, originated from the different suspensions used in the processing route developed in this work, may present different sintering shrinkages due to different starting green densities. Therefore, the amount of aluminum necessary for shrinkage compensation must be tailored for each suspension separately. Moreover, this should be done for each sintering temperature of interest, i.e., 1200°C and 1300°C in case of this work. The next section presents how the compositional tailoring was performed, exemplified by calculations performed for RBAO matrices to be sintered at 1200°C. Values obtained from similar calculations for 1300°C are only briefly presented.

6.2.1 Experiments and results: Determination of low-to-zero shrinkage compositions

(i) Intra-bundle matrix (IB)

To estimate the amount of aluminum necessary for compensating the shrinkage of the IB matrix (originated from the ethanol-based slurry), the linear dimensional change (LDC) of RBAO samples containing different amounts of aluminum was investigated by dilatometry. RBAO precursor powders were produced according to the procedure described in section 3.2.1, varying the aluminum amount from 10 to 30 vol% in a 10 vol% interval. These powders are designated RB10, RB20 and RB30, respectively. All compositions were milled with 10 vol% coarse alumina powder and 20 vol% yttria-stabilized zirconia. The amount of fine alumina powder was adjusted according to the aluminum content. Green RBAO matrix samples were prepared by pressing, according to the procedure described in section 3.2.3. Samples were ground to the dimensions of 12 mm × 4 mm × 4 mm and heated to 1200°C in a dilatometer (DIL 402 PC, Netzsch, Selb, Germany), following the heating and cooling rates shown in Figure 18. Samples were held at 1200°C for 5 hours.

The results of the dilatometric analyses are shown in Figure 48. The larger the aluminum content, the larger the expansion due to the oxidation of aluminum particles and the smaller the resulting shrinkage after cooling. The major expansion

occurs up to 600°C. Beyond this temperature, the LDC remains nearly constant, until the melting temperature of aluminum (T_{Al}) is achieved, leading to a slight contraction of the sample. Oxidation proceeds, then, by liquid/gas reaction, although no significant expansion is observed anymore. At ~1050°C, all samples start to shrink due to sintering.

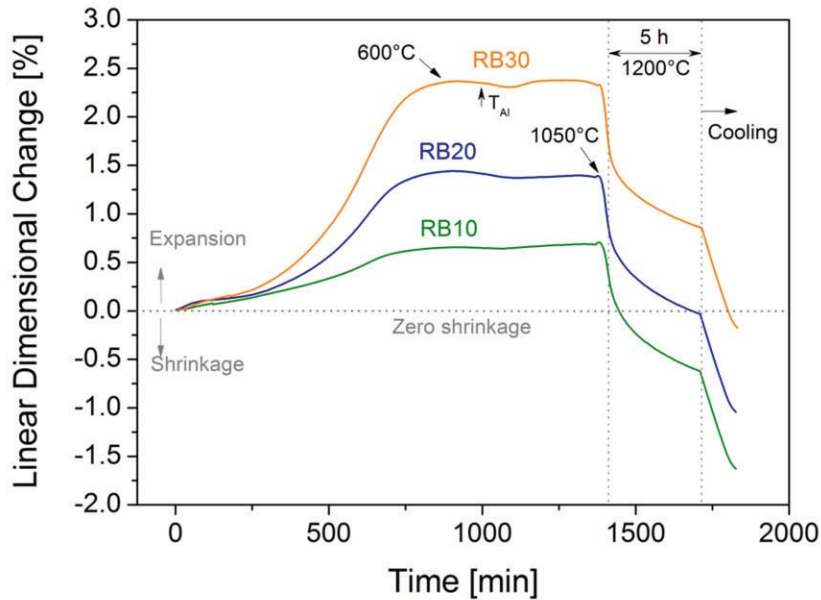


Figure 48: Dilatometry curves of RBAO samples containing different amounts of aluminum. T_{Al} indicates the melting temperature of aluminum. Samples were produced by cold isostatic pressing.

Based on this dilatometry data, it was possible to calculate the linear dimensional change of each RBAO composition after sintering at 1200°C for 30 min. This was done by taking the value of LDC obtained after 30 min at 1200°C and subtracting the shrinkage endured by the sample during cooling to 25°C, which is associated with its thermal expansion. The values obtained are called here LDC_{IB} , and were fitted to a linear function of the aluminum volume fraction, v_{Al} , according to:

$$LDC_{IB} = LDC_o(\eta v_{Al} - 1) \quad \text{Eq. 23}$$

where LDC_o is the linear dimensional change for $v_{Al} = 0$. Results are shown in Figure 49. Values of $LDC_o = 1.78\%$ and $\eta = 3.8$ were found for the experimental data obtained. Using this equation, the aluminum content necessary to achieve zero shrinkage in the IB matrix of composites sintered at 1200°C could be calculated. A value of $v_{Al} \cong 0.26$ was obtained. This RBAO powder, designated here RB26, was

then used in the preparation of ethanol-based suspensions to manufacture RBAO-matrix composites to be sintered at 1200°C.

A similar analysis was performed to estimate the aluminum content necessary to obtain zero shrinkage on RBAO matrices sintered at 1300°C for 30 min. A value of $v_{Al} \cong 0.61$ was calculated and this composition is hereafter designated by RB61.

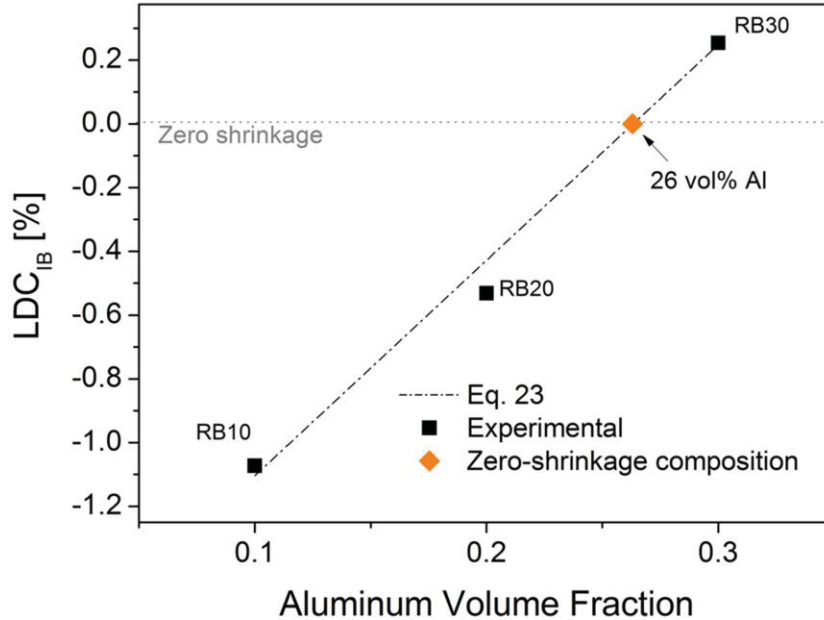


Figure 49: Linear dimensional change calculated from dilatometry data for cold isostatic pressed RBAO samples containing different amounts of aluminum, considering a 30 min sintering at 1200°C. The experimental data was fitted to Eq. 23, with $LDC_0 = 1.78\%$ and $\eta = 3.8$.

(ii) Inter-textile matrix (IT)

To achieve low-to-zero shrinkage in the IT matrix, the aluminum amount in the RBAO powder should not only compensate for the shrinkage due to sintering, but also for the shrinkage due to pyrolysis of the organic binder system. In order to determine the most appropriate combination of aluminum amount in the RBAO powder and the solid content of the paraffin-based suspension, a total of 6 suspensions were produced using powders containing either 20 or 30 vol% aluminum (RB20 and RB30, respectively) and varying the solid content from 50 to 58 vol%, with a 4 vol% increment.

Suspensions were prepared according to the procedure described in section 4.2.2 and molded to discs by softening them at 115°C into cylindrical aluminum forms with a diameter of ~ 38.5 mm. Debinding and sintering were conducted according to the thermal cycles shown in Figure 31 and Figure 18, respectively. Sintering

was performed at 1200°C for 30 min. The linear dimensional change (LDC_{IT}) was measured geometrically, by comparing the diameter of the samples before and after the debinding/sintering procedure. Results are shown in Figure 50.

The shrinkage of the monolithic IT matrix samples decreased by increasing the solid content of the paraffin-based suspensions. Additionally, samples produced with the RB30 powder presented lower shrinkages than those produced with the RB20. According to the results presented in Figure 50, the sample which most approaches zero shrinkage is that produced with an RB30-loaded suspension containing 58 vol% solids. However, empirical observations showed that the rheology of this suspension was not adequate for the manufacture of preregs. Poor adhesion between this paraffin-based suspension and the pre-impregnated fiber textiles, as well as difficulties in obtaining thin preregs are some of the problems observed. Decreasing the solid content to 56 vol% helped solve these problems and enabled a successful prepreg manufacture by lamination. As indicated in Figure 50, this composition was selected to be used in the production of RBAO-matrix CMCs sintered at 1200°C for 30 min. Although the associated shrinkage is not zero, it is very low ($\sim 1\%$) and should suffice to reduce the formation of shrinkage-related cracks in the oxide composites.

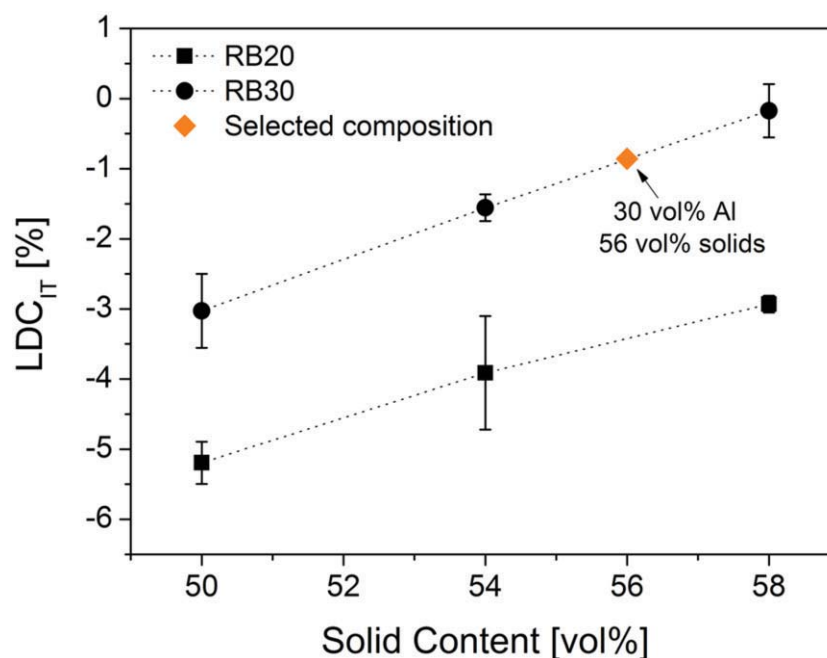


Figure 50: Linear dimensional change of RBAO samples produced with paraffin-based suspensions with different solid contents and sintered at 1200°C for 30 min. The suspensions were loaded with powders containing 20 and 30 vol% aluminum. Dotted lines were drawn to help guide the eye.



In a similar way, the most suitable paraffin-based suspension to manufacture composites sintered at 1300°C for 30 min was determined. The result is a combination of 56 vol% solids and an RBAO powder containing 50 vol% Al (RB50), which leads to a low shrinkage of ~1.5%.

6.2.2 Experiments and results: Composite manufacture and characterization

(i) Experiments

RBAO powders containing the aluminum amounts defined in the previous section were prepared by attrition milling, according to the procedure described in section 3.2.1. The particle size distributions of all RBAO compositions were analyzed after 7 h milling, following the procedure described in section 3.2.4.

Paraffin-based suspensions containing 56 vol% solids were prepared using the powders RB30 and RB50, for composites to be sintered at 1200°C and 1300°C, respectively. Ethanol-based slurries containing 32 vol% solids were produced using the powders RB26, for 1200°C, and RB61, for 1300°C. The procedures used for the preparation of these suspensions are described in sections 4.2.2 and 4.4.1.

Composites were manufactured by the novel processing route using Nextel™ 610 woven fabric, cut into 100 cm × 110 cm pieces, as reinforcement. Eight prepregs were consolidated for each composite. Debinding and sintering were conducted according to the heating cycles shown in Figure 31 and Figure 18, respectively. The composite sintered at 1200°C for 30 min is designated RB-12AS and the one sintered at 1300°C for 30 min is called RB-13AS, where RB stands for RBAO, 12 or 13 are related to the sintering temperature and AS means as-sintered.

Microstructural investigation by SEM was conducted on cross sections prepared according to the procedure described in section 4.2.7. Fiber volume content was calculated by Eq. 21.

(ii) Results

Figure 51(a) shows the particle size distributions of the RBAO matrix powders after milling. Powders with higher aluminum contents (RB50 and RB61) presented larger particle sizes than those containing less aluminum (RB26 and RB30). Figure 51(b) shows the parameters D10, D50 and D90 of the distributions presented in

Figure 51(a). These parameters are calculated based on the total volume of the sample and represent the maximum particle diameter below which 10 vol%, 50 vol% or 90 vol% of the particles exist.

Powders RB26 and RB30 present narrow particle size distributions with a median size, D50, of $\sim 1.3 \mu\text{m}$, which is in the range recommended for a successful oxidation process. Powders RB50 and RB61 present $D50 > 3.5 \mu\text{m}$ and a broader particle size distribution than RB26 and RB30. The values of D90 of RB50 and RB61 are larger than $16 \mu\text{m}$, indicating the presence of oversized particles that were not successfully comminuted, even after 7 h of intensive milling.

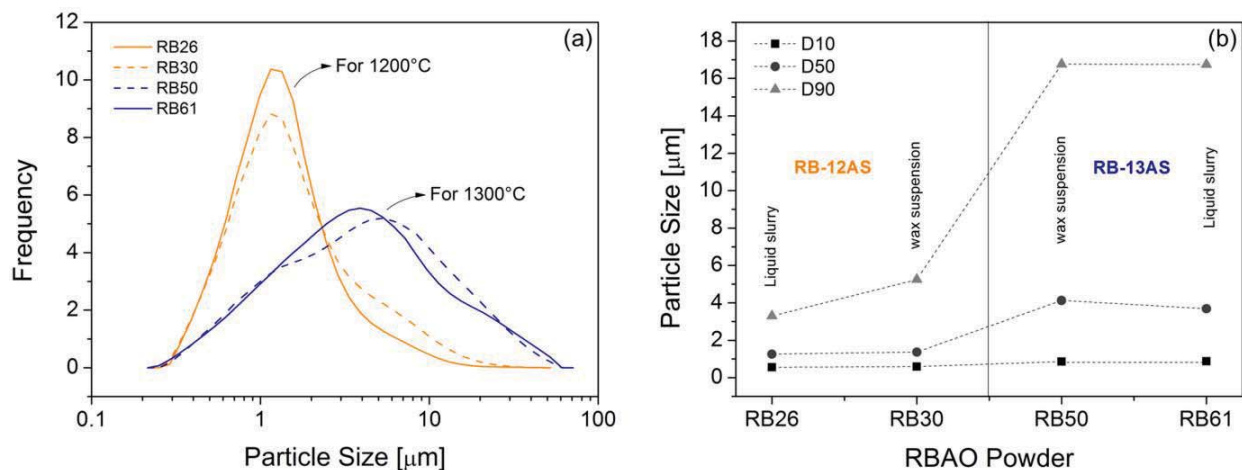


Figure 51: (a) Particle size distribution of the different RBAO matrix powder compositions; (b) Comparison of Parameters D10, D50 and D90 of the different RBAO powders: in the left-hand side, powders used for RB-12AS; in the right-hand side, powders used for RB-13AS. The dotted lines in (b) were drawn to help guide the eye.

The microstructure of the RB-12AS is shown in Figure 52. Tailoring the RBAO matrix composition was effective to achieve low-to-zero shrinkage and fabricate a crack-free composite containing $\sim 36 \text{ vol}\%$ fibers.

Nevertheless, as shown in Figure 52, the use of RBAO matrix originated a new processing challenge: the formation of large voids in the IT matrix regions. These voids vary from tens to hundreds of micrometers in size, being some of them spherical and others elongated in the lamination direction. Image analysis of microstructures such as those presented in Figure 52 indicated a void volume fraction of $6.27 \pm 3.20 \text{ vol}\%$. A total of 6 micrographs at magnifications between

75 \times and 300 \times were analyzed. The large scatter of this data is due to the irregular distribution of voids in the samples.

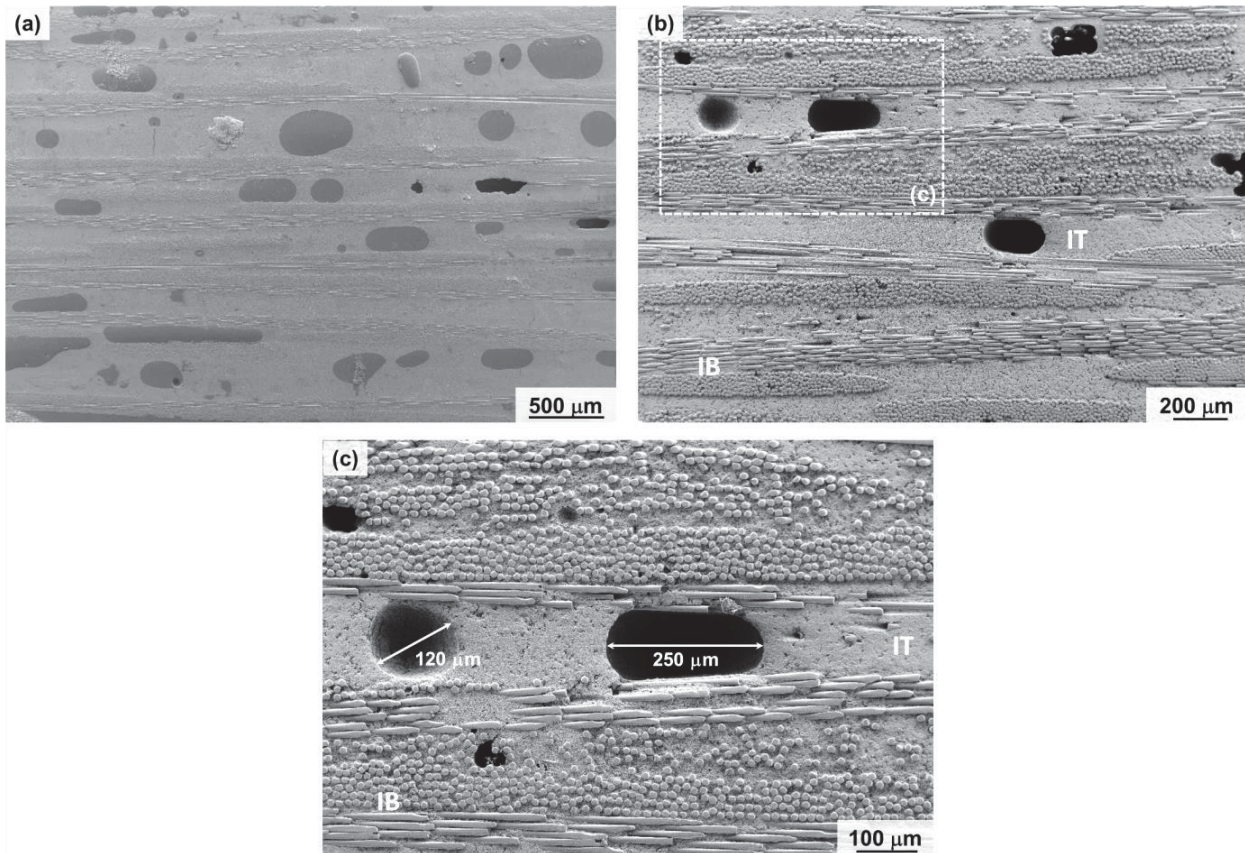


Figure 52: Microstructure of the RBAO-matrix composite sintered at 1200°C for 30 min (RB-12AS).

Whereas voids appeared in composites sintered at 1200°C, the production of an RBAO-matrix CMC sintered at 1300°C for 30 min was not successful. Figure 53 shows pictures of this composite after sintering. Up to the debinding procedure, this sample was intact. Nevertheless, it delaminated completely during the oxidation/sintering treatment. The IT matrix has cracked and broken into pieces. The presence of gray-colored areas and fragments indicates an incomplete oxidation of the aluminum particles, which can be associated with the large particle sizes of the precursor powders used in this composite.

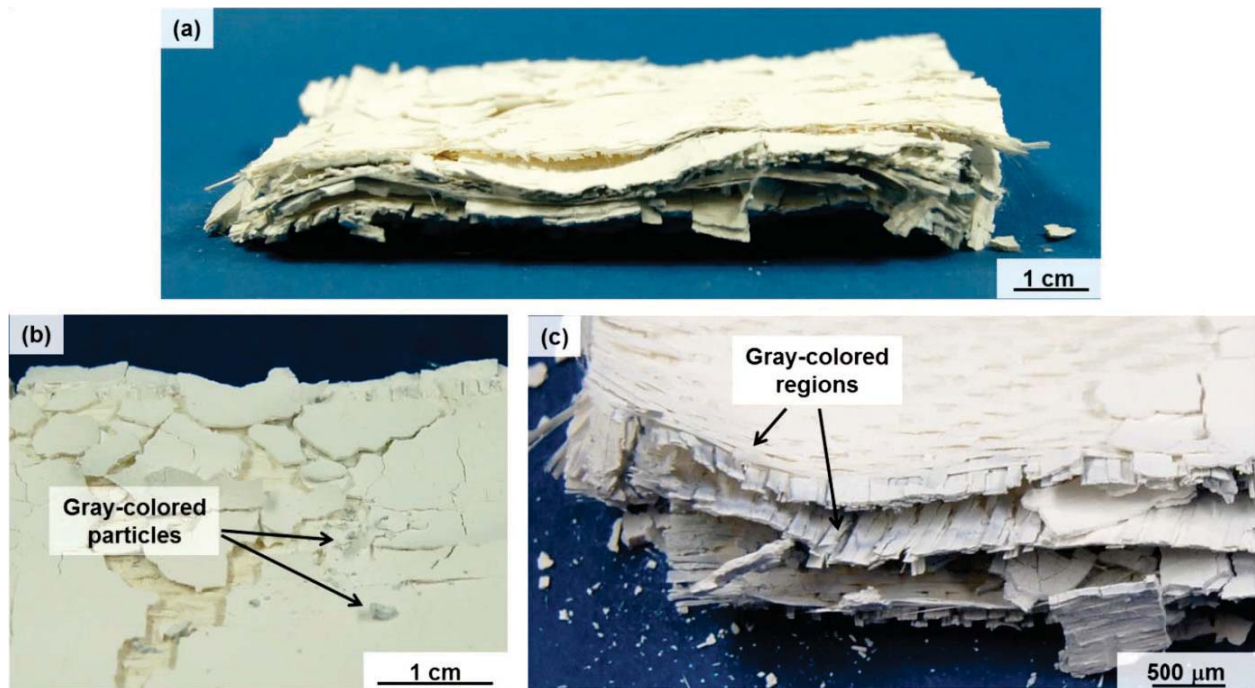


Figure 53: RBAO-matrix composite sintered at 1300°C for 30 min. (a) picture showing delamination in multiple layers. (b) and (c) gray-colored particles and regions indicating incomplete Al oxidation.

6.2.3 Discussion

Results presented here prove the possibility of tailoring RBAO compositions to achieve low-to-zero shrinkages after sintering. The absence of cracks in sample RB-12AS confirms the successful adjustment of RBAO compositions for sintering at 1200°C.

However, when larger sintering shrinkages such as those obtained at 1300°C are to be compensated, large amounts of aluminum are needed in the precursor powders and the milling efficiency of the aluminum particles decreases. This is evidenced by the values of D90 measured for the RB50 and RB61 powders (>16 μm), which are in the range of the starting aluminum particle size (~20 μm). The decrease in the milling efficiency of RBAO powders containing larger amounts of aluminum particles can be attributed to the lower relative amount of hard, oxide particles in their starting compositions. Such particles usually facilitate the comminution of the ductile aluminum during milling.

An alternative to achieve smaller particle sizes in RBAO powders containing large amounts of aluminum (>50 vol%) is the use of finer starting aluminum particles, which do not need to be further comminuted. Although this would increase the raw



materials price, the possibility it offers to consolidate defect-free matrices at higher sintering temperatures could justify it. This was however not analyzed in the present work and remains here as a suggestion for further investigation.

As for the large voids present in the RB-12AS composite, they may be detrimental to the mechanical properties of this material. This will be discussed in more detail in Chapter 7. The causes for this void formation and a possible solution for its mitigation are presented in the next section.

6.3 Void formation: investigation of causes and solutions for this processing problem

According to experimental observations, the voids existent in the RBAO-matrix composites produced in this work are originated from entrapped gas bubbles that evolve in the paraffin-based suspension during the lamination procedure. These bubbles are formed as soon as the suspension is softened at a temperature of $\sim 115^{\circ}\text{C}$ (see Figure 54).

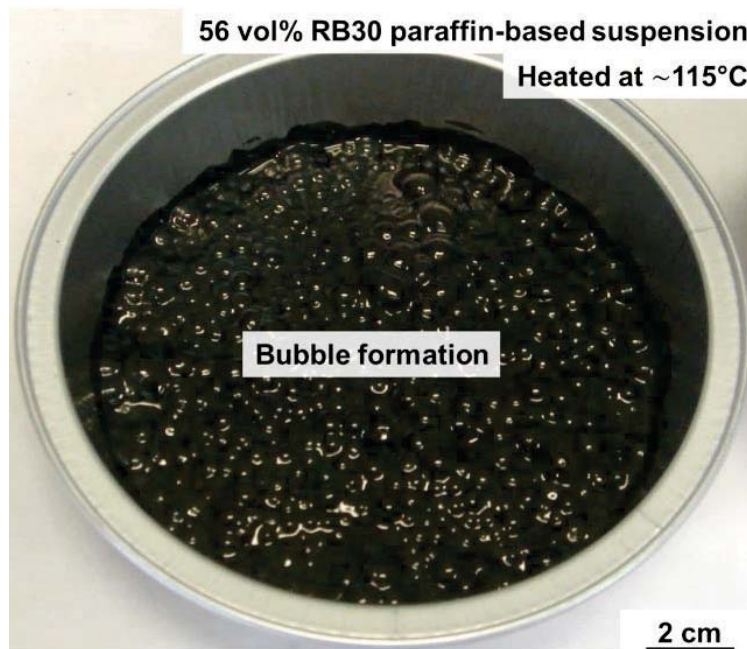


Figure 54: Bubble formation in an RBAO loaded paraffin-based suspension when heated to $\sim 115^{\circ}\text{C}$.



In order to investigate the cause of gas evolution and bubble formation, different hypotheses were considered and analyzed, which are presented as follows:

(i) Thermal decomposition of organics from the binder system:

A possible reason for the formation of gas bubbles is the thermal decomposition of organics from the binder system, provided their decomposition temperature lies below or around 115°C.

(ii) Decomposition of organics due to a catalytic effect of the RBAO powder:

It has been shown that oxide fillers may catalyze the decomposition of organic binders in polymeric-based suspensions, thereby shifting the onset of decomposition to lower temperatures [104,105]. Therefore, even if the decomposition of the neat binder system used in this work occurs at temperatures >115°C, the presence of such a catalytic effect could shift the onset of degradation to lower temperatures and thereby cause the formation of bubbles during the lamination procedure at ~115°C.

(iii) Evaporation and decomposition of adsorbed species from the RBAO powder surfaces:

As presented in Figure 16, mass spectroscopy analysis performed by Holz [75] indicated the liberation of H₂O, H₂ and C_xH_y species upon heating an RBAO powder up to 600°C. The detection of H₂O (up to ~230°C) was associated with the evaporation of physically adsorbed water, H₂ with the decomposition of hydroxides and C_xH_y was related to the desorption of molecules from the milling liquid (acetone, as used in this work). The evaporation of such species could also be the reason for the formation of gas bubbles.

(iv) H₂ gas evolution from aluminum-induced reactions:

It is well-known that metallic aluminum reacts with water to form aluminum oxide or hydroxides, thereby liberating H₂ [106]. Such reactions are used for different technical purposes, such as pore formation in the fabrication of cellular concrete [107,108] and hydrogen production for energy generation (via fuel cells) [106,109–111]. For both purposes, it is desirable that the aluminum-water reaction proceeds until aluminum is completely oxidized or hydrated. This is, however,

only possible if a method for continuously circumventing the typical oxide passivating layer¹⁰ on the aluminum surfaces is employed [106].

The most common way of sustaining the reaction between aluminum and water is to work with high pH (alkaline) solutions, such as those evolved during cement hydration in the production of cellular concrete [107]. Nevertheless, more recent investigation on materials for fuel cell applications showed a way to completely react aluminum at room temperature, using distilled [110] or tap water [109] (i.e., at neutral or close to neutral pH). For this purpose, aluminum must be intensively milled with aluminum oxide or hydroxide powders [109,110] and, in some cases, have its surface modified by a reaction with $\text{Al}(\text{OH})_3$ to form a loose γ -alumina layer onto the aluminum particles [110]. An explanation for the effect of oxides on the enhanced reactivity of aluminum with water was suggested by Deng *et al.* [111] and is schematically shown in Figure 55.

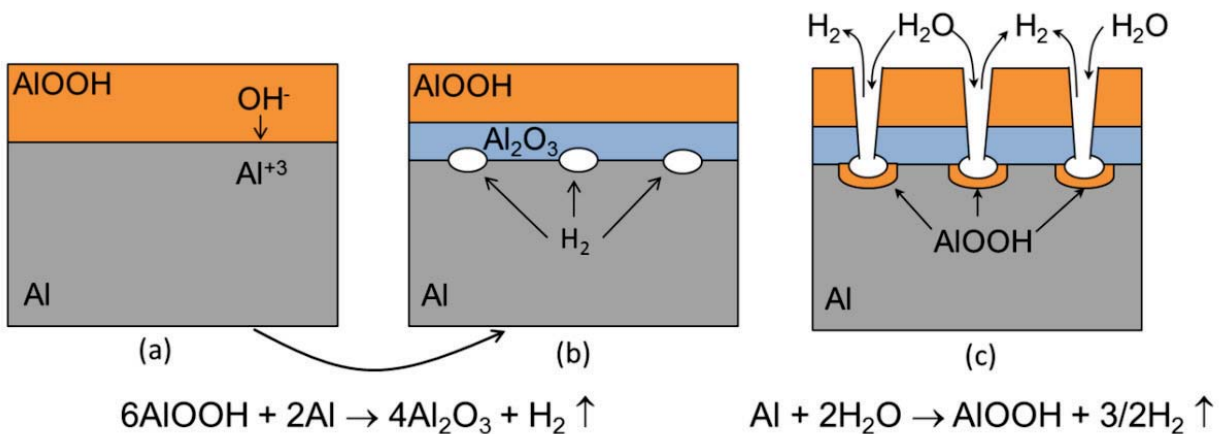


Figure 55: Schematic representation of the mechanisms of aluminum-boehmite and aluminum-water reactions. Adapted from Bunker *et al.* [112] and Deng *et al.* [111].

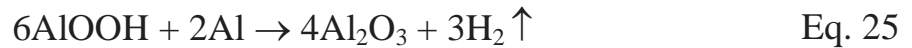
It was postulated that the alumina layer present on the aluminum particle surfaces may completely hydrate when in contact with water to form boehmite (AlOOH) [111]:



¹⁰ This dense, oxide passivating layer restricts the contact of the metallic aluminum with reactants present in the environment, such as water and oxygen. This results in the high corrosion resistance of aluminum, at least in environments which are not extremely acidic or alkaline [109].



The OH⁻ ions, which are suggested to be the mobile species in these hydrated films [112], may then diffuse to the aluminum-boehmite interface and react with the metallic aluminum to form alumina and H₂ molecules (reaction in the left-hand side of Figure 55) [111]:



Since the H₂ molecules do not easily diffuse through the alumina film, they accumulate and form gas bubbles in the aluminum-alumina interface [111]. Under certain favorable conditions, these bubbles can rupture the hydrated oxide film on the particle surface and expose the metallic aluminum to the surrounding water, as represented in the right-hand side of Figure 55. This will lead to the formation of boehmite, again liberating H₂, according to [111]:



Boehmite forms instead of alumina because it is more thermodynamically stable at low temperatures (<300°C) [111,113].

There are clear similarities between RBAO powders and these modified aluminum powders used for H₂ generation: (a) RBAO powder is also prepared by intensively milling aluminum and oxide particles; (b) it has been shown that the surfaces of aluminum particles in RBAO are modified during milling by the formation of amorphous alumina and aluminum hydroxides (boehmite and diaspore) [16,75]; (c) Holz [75] reported that RBAO powders completely hydrolyze to boehmite when heated in water up to 50°C; (d) H₂ molecules are released by heating RBAO powders over a large range of temperatures (see Figure 16) [75].

These facts suggest that a mechanism such as that presented in Figure 55 can also apply to RBAO powders. The gaseous H₂ molecules evolved during reactions between aluminum and water or aluminum and boehmite could therefore also contribute to bubble formation in the RBAO-loaded, paraffin-based suspensions.

(v) A combination of different effects:

There is certainly also the possibility that two or more causes discussed here are simultaneously responsible for the formation of gas bubbles in the RBAO loaded paraffin-based suspensions.



In the following section, the methods used to evaluate each of these hypotheses are presented.

6.3.1 Experiments: evaluation methods

Hypothesis (i): in order to investigate if the thermal decomposition of organics from the binder system could be the cause of bubble formation, the degradation of the different organic components was analyzed by thermogravimetry. Samples were heated from room temperature to 500°C at 1°C/min in a Netzsch simultaneous thermal analyzer (STA 409, Netzsch, Selb, Germany).

Hypothesis (ii): a possible catalytic effect of RBAO on the decomposition of the binder system was investigated by comparing the decomposition behavior of the neat organic system with that of a RB30-loaded suspension containing 56 vol% solids. The suspension was prepared according to the procedure described in section 4.2.2. The neat organic system was prepared by melting and homogenizing the organic components in a glass beaker at 100°C. Thermogravimetry was also used for this investigation. Samples were heated to 600°C at 5°C/min.

Hypothesis (iii): the effect of adsorbed species on the formation of bubbles was investigated by different methods as follows:

To evaluate the mass change and the presence of reactions as a function of temperature, RB20 and RB30 powders were investigated by simultaneous thermal analysis (DTA/TG). Samples were heated in a Netzsch STA 409 instrument to a temperature of 650°C, following the heating rates indicated in Figure 18.

Karl-Fischer titration (Aqua 40.00, Electrochemie GmbH, Halle, Germany) was used to measure the water content present on the surface of the RB30 powder (milled in acetone for 7 h and dried in a cupboard for 2 days). A total of four measurements were made on different samples of the same powder. Samples were heated to 150°C during the measurements.

Considering that adsorbed species can be thermally removed, tests were also performed on RBAO powders dried at 300°C for 10 h in a muffle furnace. True density of dried powders containing different aluminum amounts was measured by He-pycnometry (AccuPyc II 1340, Micromeritics, Aachen, Germany) and compared to the respective values measured in the as-milled condition (dried at



room temperature in a drying cupboard). A total of 10 measurements were conducted for each powder composition.

In addition, different paraffin-based suspensions were prepared using RB30 powders in different conditions: as-milled, and dried for 10 h at temperatures of 100, 200 and 300°C. A maximum temperature of 300°C was used to avoid extensive oxidation of the aluminum particles (see section 3.4.1). The RB30 composition was selected for this analysis because it was used in the manufacture of the RB-12AS composite. All suspensions contained 56 vol% solids and were prepared according to the procedure described in section 4.2.2. Monolithic matrix samples were prepared by softening the suspensions at ~115°C into cylindrical aluminum forms (as shown in Figure 54). After debinding, samples were sintered at 1200°C for 30 min, following the RBAO heating cycle (Figure 18). After sintering, samples were cut using a precision cut-off machine (Brillant 220, ATM, Mammelzen, Germany) equipped with a 150 µm diamond disk. The cross sections were then analyzed using a stereomicroscope (Olympus SZX10, Hamburg, Germany).

If bubble formation is purely caused by the evaporation of adsorbed species, no pores should be detected in samples produced with the dried RBAO powders.

Hypotheses (iv) and (v): these hypotheses could be evaluated with the results obtained for the previously described evaluation methods.

6.3.2 Results

The mass change of the different organic components used in the paraffin-based suspensions as a function of temperature is shown in Figure 56. The first component to decompose is the Octadecylamine (ODA) at ~145°C, followed by paraffin and Solsperse at ~170°C and ~260°C, respectively. The undulations in the Solsperse curve are attributed to an instability of the balance during the TG experiment. No component is therefore expected to decompose at the temperature used for prepreg lamination (115°C).

Figure 57 shows the thermogravimetric curves of the neat binder system and the 56 vol% concentrated, RB30-loaded suspension. The addition of RBAO powder shifted the decomposition of the binder system to a higher temperature. The RBAO suspension starts to considerably lose mass at ~244°C, while the neat binder

system at $\sim 215^{\circ}\text{C}$. This delay may be explained by restrictions imposed by the solid particles to the transport of decomposition products out of the sample. Because of the high solid content (which accounts for ~ 84 wt% of the whole suspension), the RBAO suspension loses only about 16 wt% up to 480°C , when the binder system is completely decomposed. The gain in weight above this temperature is related to the oxidation of the RBAO powder. Again, no loss in weight is detected at the temperature used for prepreg lamination (115°C).

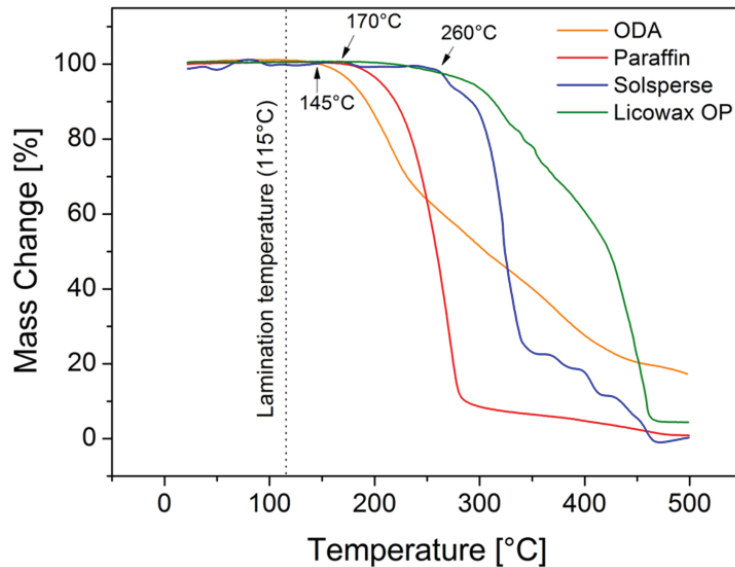


Figure 56: Thermogravimetric analysis of the organic components used in the paraffin-based suspensions. All curves were measured at $1^{\circ}\text{C}/\text{min}$.

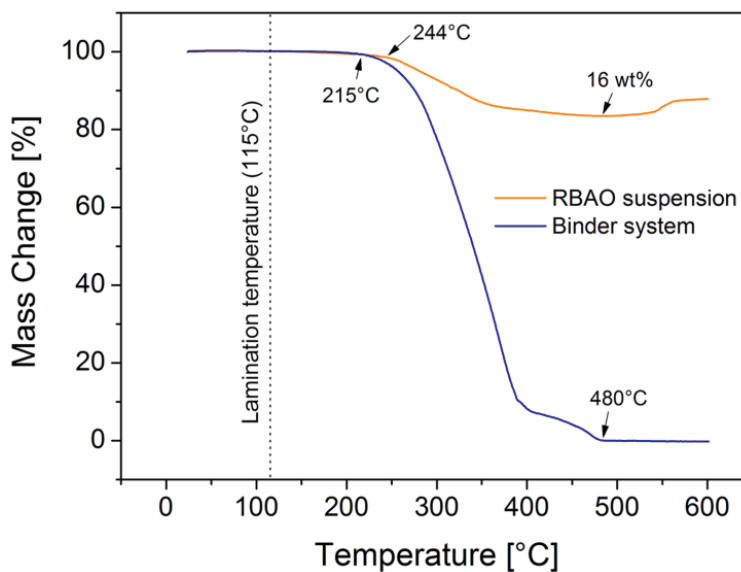


Figure 57: Comparison between the decomposition behavior of the neat organic system and that of a 56 vol% RB30 loaded suspension. Both curves were measured at $5^{\circ}\text{C}/\text{min}$.

Figure 58 shows the results of the simultaneous thermal analysis performed on the RB20 and RB30 green powders. Two exothermic peaks can be identified for each RBAO powder. The one at $\sim 507^\circ\text{C}$ is well-known and is attributed to the solid/gas oxidation of aluminum particles. Nevertheless, to the best author's knowledge, no publication so far has explained the origin of the broad exothermic peak between $\sim 112^\circ\text{C}$ and $\sim 315^\circ\text{C}$. Like the oxidation peak at $\sim 507^\circ\text{C}$, the intensity of this broad peak is influenced by the aluminum amount present in the powder. The larger the aluminum content, the more intense is the peak.

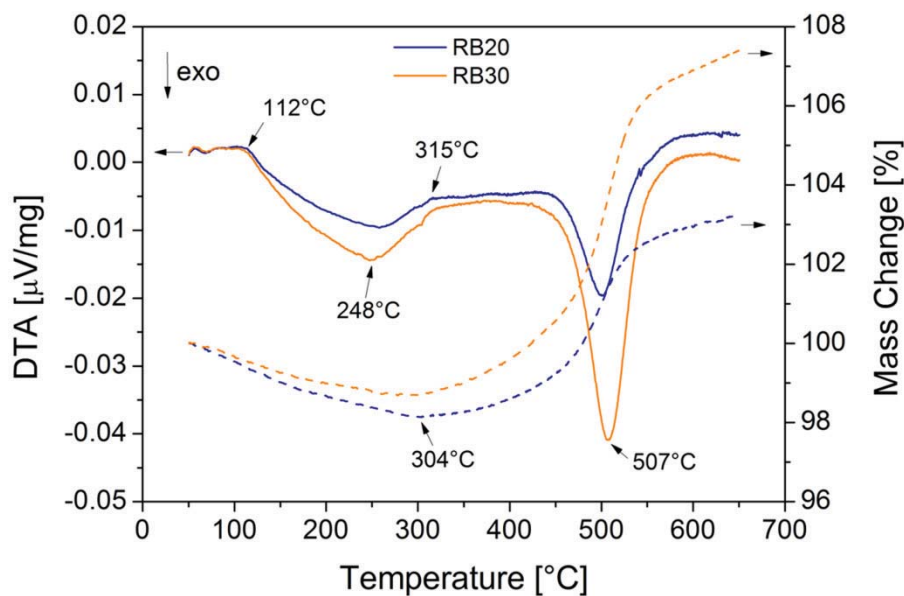


Figure 58: Simultaneous thermal analysis of RBAO powders containing 20 vol% and 30 vol% aluminum (RB20 and RB30, respectively).

The mass loss endured by RBAO powders up to 300°C is often associated with the desorption of physically bound water and molecules from the milling liquid, as well as to the decomposition of aluminum hydroxides [16,74,114]. Although this may be correct, none of these processes explain the exothermic peak up to $\sim 315^\circ\text{C}$, since both desorption and hydroxide decomposition are endothermic processes [115,116].

A plausible explanation suggested here for the origin of this exothermic peak is the reaction of aluminum with the hydroxide on its surface and, then, with the water released from the RBAO particle surfaces, according to the reactions shown in Figure 55. Supporting this idea are the results of mass spectroscopy conducted by Holz [75], which show that H_2 molecules start being released at $\sim 80^\circ\text{C}$, accompanying the desorption of water (see Figure 16). The maximum at $\sim 248^\circ\text{C}$

coincides with the liberation of C_xH_y species, also measured by mass spectroscopy (Figure 16). Nonetheless, the release of H_2 molecules at this temperature is much more intense, indicating that the contribution of aluminum-water reactions to the detected exothermic peak is more pronounced than the decomposition of adsorbed molecules from the milling liquid.

The presence of adsorbed water was also confirmed in this work by Karl-Fischer titration. Results indicate the presence of 4.8 ± 0.6 wt% water on the surface of the RB30 powder. This result is in good agreement with measurements conducted by Temuujin *et al.* [117] for a similar RBAO powder containing 30 vol% aluminum.

Figure 59 shows the true density of green RBAO powder in the as-milled and dried state. The theoretical values were calculated by the rule of mixtures, considering densities of 2.70 g/cm^3 , 6.09 g/cm^3 and 3.98 g/cm^3 for aluminum, tetragonal zirconia and alumina, respectively.

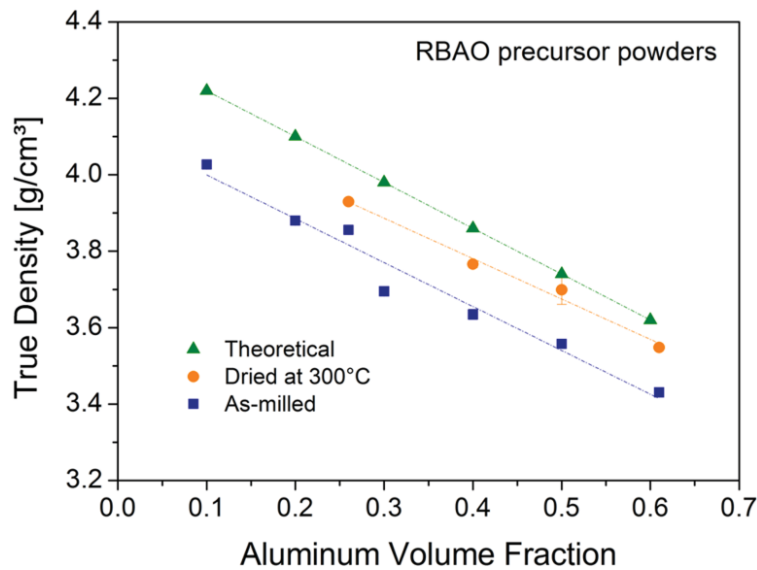


Figure 59: True density as a function of aluminum content of RBAO powders in the as-milled (dried at room temperature) and dried (at 300°C for 10 h) conditions. The theoretical values were calculated by the rule of mixtures. In most cases, the error bars are not visible due to the very low scatter of the data.

The densities of the as-milled powders are lower than those expected by the rule of mixtures. Different factors may have contributed to this difference, such as (a) only crystalline phases were taken into account for the calculation of the theoretical values, while it is known that milling can cause amorphization of the RBAO particle surfaces [75] and (b) the as-milled RBAO powders contain some amount of monoclinic zirconia [16], which has a lower density (5.83 g/cm^3) than its

tetragonal form. Drying the powders at 300°C for 10 h leads to an increase in the true densities in relation to the as-milled powders. This density increase is consistent with the idea that aluminum reacts with boehmite and water to form alumina (Eq. 25) and boehmite (Eq. 26), respectively. Alumina and boehmite have densities of 3.98 g/cm³ and 3.01 g/cm³, respectively, which are both higher than that of metallic aluminum (2.7 g/cm³).

Cross sections of sintered monolithic samples produced with paraffin-based suspensions of the RB30 powder in different drying conditions are shown in Figure 60.

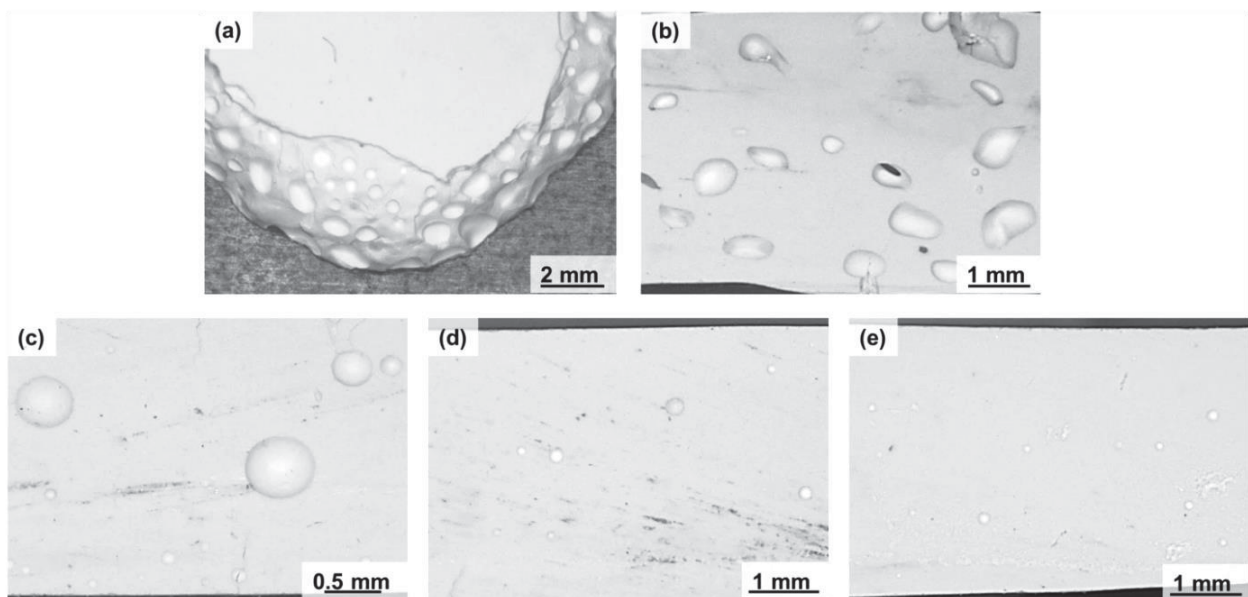


Figure 60: Monolithic IT matrix samples prepared with paraffin-based suspensions containing RB30 powders in different conditions: (a) and (b) as-milled (dried at room temperature); (c) dried at 100°C for 10 h; (d) dried at 200°C for 10 h; (e) dried at 300°C for 10 h. All suspensions contained 56 vol% solids. After debinding, sintering was performed at 1200°C for 30 min.

The sample produced with the as-milled powder (Figure 60(a) and (b)) presents the largest amount of voids, whose sizes are in the range of those presented by the RB-12AS composite (Figure 52). Drying the powder at 100°C for 10 h (Figure 60(c)) considerably decreases the amount of voids, although they are still very large. Drying temperatures of 200°C or 300°C (Figure 60(d) and (e), respectively) are much more effective than 100°C in reducing the formation of voids, although they are not completely eliminated. The best results were obtained for a drying temperature of 300°C (Figure 60(e)), since the voids present in this sample are



slightly smaller than those obtained after drying the powder at 200°C (Figure 60(d)).

6.3.3 Discussion

Results shown in Figure 56 and Figure 57 indicate it is unlikely that the formation of bubbles in the paraffin-based suspension during lamination is caused by the decomposition of organics from the binder system (hypotheses (i) and (ii)). Both the single organic components and the complete binder system decompose at temperatures higher than that used for lamination (115°C). Moreover, the addition of 56 vol% RBAO does not shift the decomposition of the binder system to lower temperatures and therefore has no catalytic effect on the decomposition of the organics.

Different results indicate that desorption of molecules (mainly H₂O) from the RBAO powder surfaces (hypothesis (iii)) may contribute to the bubble formation in the paraffin-based suspensions. Titration indicates the release of ~5 wt% water from the RB30 precursor powder when heated at 150°C. Thermogravimetry shows that RBAO powders lose weight when heated up to 300°C (Figure 58). Moreover, drying the RBAO powders up to 300°C, before preparing the paraffin-based suspension, considerably reduces the amount and size of the bubbles formed, although it does not eliminate them completely (Figure 60).

Mass spectroscopy conducted by Holz [75] (Figure 16) shows that physically adsorbed water evaporates between room temperature and ~250°C. If bubble formation was exclusively a result of the evolution of water vapor from the RBAO surfaces, no voids should be detected in the sample produced with the powder dried at 300°C for 10 h. Since this is not the case, there should be another factor contributing to the void formation in the RBAO-loaded paraffin-based suspensions.

Considering the lamination temperature used in this work (~115°C), it is unlikely that this additional cause is the decomposition of aluminum hydroxides. According to Sato [80], such hydroxides decompose in the temperature range of 200°C to 700°C.

Nevertheless, results presented here support the hypothesis that the additional factor contributing to bubble formation in the paraffin-based suspensions is the H₂



evolution from aluminum-boehmite or aluminum-water reactions, which may occur even at temperatures lower than 115°C.

The presence of hydroxides on the aluminum particle surfaces of RBAO has been previously shown elsewhere [16,75]. Therefore, the structure of these particles may be schematically represented as in Figure 55(a). By increasing the temperature during the lamination procedure, the reaction between aluminum and the mobile OH^- ions from the hydroxide layer is stimulated, forming alumina and liberating H_2 that remains entrapped at the aluminum-alumina interface (Figure 55(b)). When the coalesced H_2 bubbles rupture the hydroxide layer, the metallic aluminum is exposed and may react with the water desorbed from the surface of the RBAO powder. Thereby, more H_2 molecules are formed, according to the reaction described in Eq. 26. The released H_2 may, then, remain entrapped in the paraffin-based suspension, also contributing to the formation of voids in the sintered samples.

It seems, therefore, that the formation of bubbles in suspensions prepared with as-milled RBAO powders, such as that used in the manufacture of the RB-12AS composite (Figure 52), results from a combined effect of the evaporation of physically adsorbed water from the RBAO powder surfaces and the release of H_2 from aluminum-boehmite or aluminum-water reactions. While the contribution of physically adsorbed water to the bubble formation can be mitigated by drying the powder above 200°C, the reaction between aluminum and OH^- ions from the hydrated surface layers may still occur, leading to the formation of gas bubbles in the suspension. Nevertheless, the amount and size of these bubbles are much smaller than those of samples produced with suspensions loaded with as-milled RBAO powders (see Figure 60). Hence, drying the RBAO precursor powder at 300°C is considered here as the most appropriate solution for avoiding the excessive formation of voids in the IT matrix of RBAO composites. This procedure was adopted in the manufacture of a new RBAO-matrix composite, as will be presented in the next section.



6.4 Production of void-free RBAO-matrix composites

6.4.1 Experiments: Composite manufacture and characterization

A new RBAO-matrix composite was manufactured in a way similar to the RB-12AS sample presented in section 6.2.2. However, drying procedures were conducted to mitigate void formation in the inter-textile (IT) matrix. The RB30 powder, used for the paraffin-based suspension, was dried in a muffle furnace at 300°C for 5 h prior to suspension preparation. Likewise, the alumina fiber textiles infiltrated with the RB26-loaded, ethanol-based slurry were dried under the same conditions prior to prepreg lamination. Sintering was performed at 1200°C for 30 min. This composite is designated RB_d-12AS, where the subscript “d” stands for “dried”.

6.4.2 Results and Discussion

Figure 61 shows the microstructure of the RB_d-12AS composite. As expected, the drying procedure was effective in mitigating the formation of gas bubbles in the paraffin-based suspension. Only a few voids were detected in this composite sample, as indicated in Figure 61(a) and (b). Nevertheless, through-thickness, shrinkage-related cracks were observed. This can be attributed to the partial conversion of aluminum particles to boehmite and alumina during drying, which reduces the amount of metallic aluminum available in the RBAO precursor powder for the compensation of sintering shrinkage. It seems, therefore, that the procedure presented in section 6.2.1 should be repeated in order to select new low-to-zero shrinkage compositions for the RBAO powders in the dried state.

Additionally, the use of dried RBAO powders changed the rheology of the paraffin-based suspension in a way that the production of thin prepregs was no longer possible. It seemed that the viscosity of the paraffin-based suspension increased, which made the lamination procedure more difficult. This resulted in a composite with thick IT matrix layers and a low fiber volume content of about 21 vol%. Additionally, delamination between the IB and IT matrices was observed in some regions of the sample, as indicated in Figure 61(a) and (c). This suggests a poor adhesion between both composite matrices during processing. The reason for

this change in rheology is still unclear. This should be further investigated and remains here as a suggestion for future work.

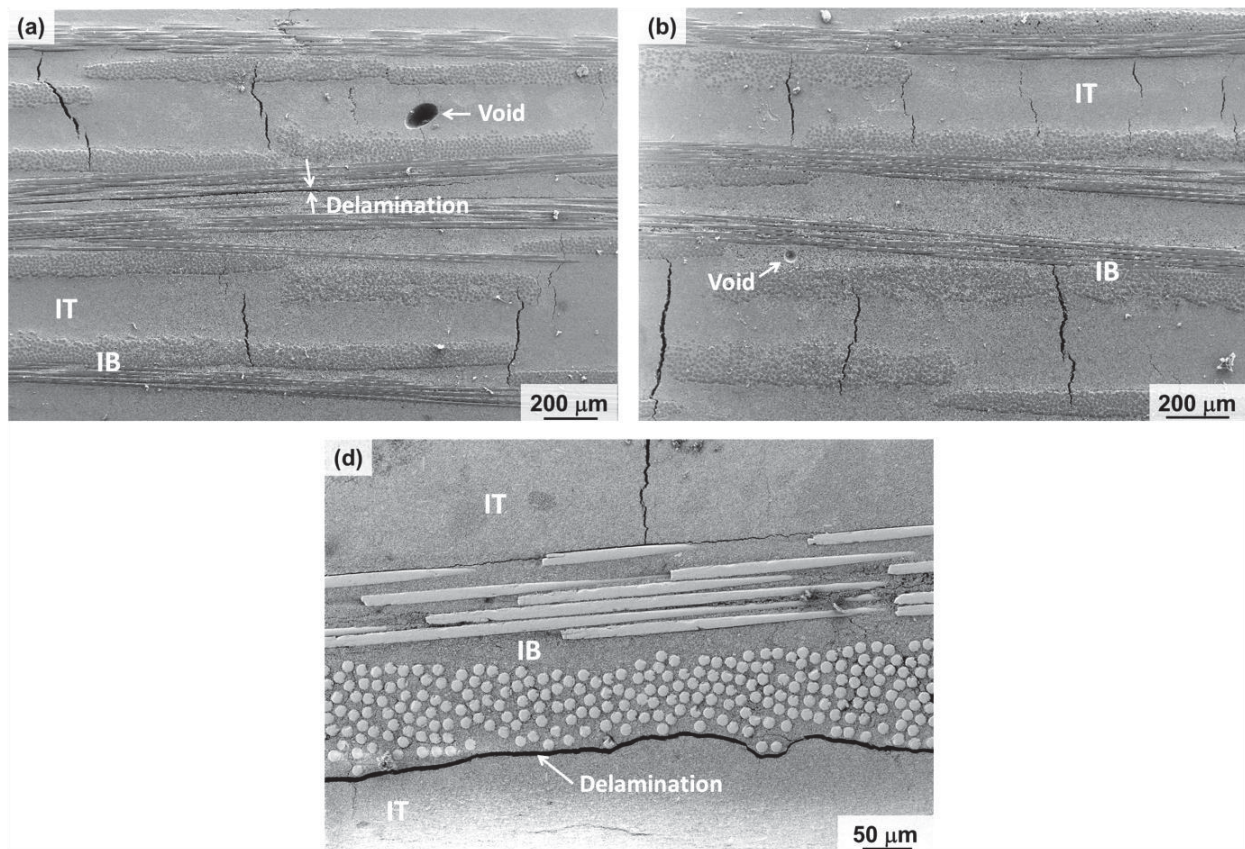


Figure 61: Microstructure of composite RB_d-12AS , produced with RBAO powders dried at 300°C for 5 h. Sintering was performed at 1200°C for 30 min. (a) and (b) show the presence of a few voids and matrix cracks. Delamination along the IB and IT interfaces are indicated in (a) and (c).

In summary, producing full-scale, RBAO-matrix composites with fine microstructures is not a straightforward task. Solving the problem of void formation resulted in other processing challenges, such as low fiber volume fraction and delamination, which must be overcome if RBAO matrix composites with a reduced amount of matrix defects are to be produced.

6.5 Conclusion

This work shows for the first time that the production of full-scale, RBAO-matrix composites is possible. However, it is not as straightforward as the composite manufacture using pure oxide matrices.



Challenges start already in the preparation of matrix powders. RBAO precursors must be intensively milled for several hours, in order to achieve small particle sizes that guarantee a successful oxidation process. The milling procedure leads, however, to the adsorption of a great amount of molecules (mainly water), which evolve as gas bubbles in the paraffin-based suspension used for prepreg manufacture, originating large voids in the inter-textile composite matrix (Figure 52).

In addition, when high amounts of aluminum are needed for compensating large shrinkages at high sintering temperatures, the milling efficiency decreases and the aluminum particles cannot be effectively milled. This was shown, in this work, by the RBAO-matrix composite treated at 1300°C, which could not be successfully sintered due to the incomplete oxidation of the large aluminum particles present in the matrix precursor powder (Figure 53).

The shrinkage of RBAO matrices can be successfully tailored by varying the amount of aluminum in the precursor powders. Nevertheless, it is very sensitive to chemical variations due to reactions such as aluminum hydration or oxidation, which can occur either during a drying procedure or during a long period of powder storage. Such reactions decrease the amount of aluminum available for shrinkage compensation and lead to the formation of matrix cracks in the composites, such as those presented in Figure 61 for the RB_d-12AS sample. Therefore, in order to profit from the zero-shrinkage tailorability of RBAO and produce crack-free, all-oxide CMCs, the procedure presented in section 6.2.1 must be performed any time the RBAO precursor powders endure some alteration.

In summary, several additional processing steps are needed in order to successfully introduce the RBAO matrix in CMCs. In the current state of this research, composites produced with a much simpler, pure oxide matrix (A8Z2, see Chapter 5) already present low shrinkages and the defect-free matrix aimed at when using RBAO. Microstructures obtained using the A8Z2 matrix are much more homogeneous and show much less defects than those of RBAO-matrix composites presented in this chapter. Therefore, for sintering temperatures of 1200°C or 1300°C, using the complex RBAO process to consolidate composite matrices is not justified. As mentioned in section 5.4, this will only be interesting when new generation oxide fibers are available and composites can be sintered at higher



temperatures ($>1300^{\circ}\text{C}$). For that, however, processing problems presented in this chapter, such as ineffective milling of RBAO powders with high aluminum contents and the unfavorable rheology of paraffin-based suspensions prepared with dried RBAO powders should be overcome.





7 Mechanical Properties of CMCs

7.1 Introduction

In the present chapter¹¹, the mechanical properties of the different all-oxide composites produced in this work are presented and discussed. The mechanical behavior of A8Z2-matrix composites is characterized after the different heat treatments discussed in Chapter 5 (see Figure 45). Additionally, RBAO-matrix composites with and without voids (Figure 52 and Figure 61, respectively) are analyzed in the as-sintered condition and results are compared to those of the reference A8Z2-matrix composites.

7.2 Materials and methods

The composites investigated in this chapter are listed in Table 5. Density and fiber volume fractions were measured geometrically and are also presented in this table. In-plane flexural properties were assessed using four-point bending (4PB) with large span-to-thickness ratios ($S/h > 28$), while interlaminar shear strength (ILSS) was measured using short beam shear (SBS) by three-point bending. Usually, eight prepregs were used to consolidate composites for 4PB, while ten prepregs were used for SBS samples. However, due to the larger thickness of the prepregs produced with RBAO powders dried at 300°C, less prepregs were used to manufacture the RB_d-12AS composites (six prepregs for 4PB samples and eight prepregs SBS specimens).

Four-point bending tests were conducted according to the German standard DIN EN 658-3 [69]. Loading was applied in a direction perpendicular to the laminate plane. Bending bars were cut from the sintered composite plates using a diamond

¹¹ Part of the results presented in this chapter have been published in the journal article “Microstructure and flexural properties of multilayered fiber-reinforced oxide composites fabricated by a novel lamination route” in the journal *Ceramics International* [99]. Copyright 2015 by Elsevier. The material from this article is reused in this thesis with permission.



cutting disk, so that fibers are oriented at 0° and 90° in relation to the bending stresses. Specimens were 90 mm long and 10 mm wide. Sample thicknesses varied between 1.8 and 2.1 mm for all samples, except for composite RB_d-12AS, which had a thickness of ~ 2.6 mm. Specimens were tested in a universal testing machine (Zwick 1474, 100 kN, Zwick, Ulm, Germany) with load and support spans of 25 and 75 mm, respectively. In order to minimize friction stresses, a thin polymer film was placed between the samples and the loading rollers during testing. Deflection was measured with an inductive displacement transducer placed at the tensile side of the specimens, at the middle of the load span. Samples were loaded at 1 mm/min. At least 8 samples were tested for each composite plate. Flexural stresses and outer fiber strains were calculated from the force-displacement data on the basis of linear elasticity according to [69,118]:

$$\sigma_{4PB} = \frac{3L(S - S_i)}{2bh^2} \quad \text{Eq. 27}$$

$$\varepsilon_{4PB} = 4.70 \frac{dh}{S^2} \quad \text{Eq. 28}$$

where L is the load acting on the sample, b is the sample width, h is the sample height, d is the deflection of the specimen at the middle of the load span and S_i and S are the inner and outer loading spans, respectively. Flexural strength σ_{4PB_u} is defined as the maximum attained stress at the point of first failure (first sudden change in the stress-strain curve) and strain at fracture ε_{4PB_u} is the strain corresponding to this stress.

Rigorously, equations from the elastic beam theory are only valid for materials with a purely linear elastic behavior up to failure and which endure small strains. Although this is not the case for the CMCs investigated here, it is assumed that the values calculated using Eq. 27 and Eq. 28 suffice for the comparison purposes of this work. According to the ASTM standard for flexural properties of CMCs [118], these equations are appropriate to obtain comparison data up to a fiber strain of 5%. Stresses calculated with Eq. 27 are called here *nominal stresses*, since they may deviate from the true stresses acting on the sample.

Composite flexural modulus E_c was calculated for each specimen within the initial linear-elastic region according to:

$$E_c = \frac{\Delta\sigma_{4PB}}{\Delta\varepsilon_{4PB}} \quad \text{Eq. 29}$$

Since the composites analyzed here present different fiber volume fractions, the flexural strength and flexural modulus data were normalized to a common fiber volume fraction, according to [119]:

$$X_o = X \frac{v_{f_o}}{v_f} \quad \text{Eq. 30}$$

where X is either σ_{4PB_u} or E_c and v_{f_o} is a specified common fiber volume fraction defined as 0.37 in this work.

Short beam shear tests were conducted according to the German standard DIN EN 658-5 [68]. Apparent ILSS values were calculated from the peak load and specimen dimensions according to:

$$ILSS = \frac{3L_{max}}{4bh} \quad \text{Eq. 31}$$

where L_{max} is the maximum load achieved in the test. Bending bars were 20 mm long and 10 mm wide, with thicknesses varying from 2.8 to 3.7 mm for the different composite plates. A support span of 14 mm was used for all samples, which were loaded at 1 mm/min in a materials testing machine (Zwick/Roell Z010, Zwick, Ulm, Germany). At least 14 samples were tested per composite plate, but only values from specimens that failed under shear were considered for the ILSS calculations.

Fracture surfaces of both 4PB and SBS samples were observed with a 3D Infinite Focus microscope (Alicona, Raaba, Austria-Graz) and by SEM. Selected SBS specimens from the A8Z2-matrix composites were completely delaminated by hand after testing, so that the crack plane could be analyzed perpendicular to the direction of crack propagation. This enabled the analysis of the fiber surfaces after the different heat treatments used in this work.



7.3 Results

Table 5 summarizes the flexural properties measured in this work.

Table 5: Properties of the all-oxide CMCs analyzed in this work

Composite ¹	AZ-12AS	AZ-12AG	AZ-13AS	RB-12AS ²	RB _d -12AS ³
------------------------	---------	---------	---------	----------------------	------------------------------------

4-Point Bending

Fiber volume fraction (vol%)	37	40	40	36	21
Density (g/cm ³)	2.98 ± 0.04	2.99 ± 0.04	3.08 ± 0.03	2.55 ± 0.09	2.74 ± 0.05
Flexural strength (MPa)	441 ± 18	392 ± 36	230 ± 47	243 ± 24	154 ± 16
Normalized flexural strength (MPa)	446	359	211	252	274
Flexural modulus (GPa)	104 ± 5	122 ± 5	140 ± 4	80 ± 5	57 ± 3
Normalized flexural modulus (GPa)	105	112	129	83	101
Strain at fracture (%)	0.49 ± 0.04	0.35 ± 0.03	0.17 ± 0.04	0.34 ± 0.04	0.37 ± 0.09

Short Beam Shear

Fiber volume fraction (vol%)	32.3	32.3	34.8	-	20.0
Apparent ILSS (MPa)	13.3 ± 1.6	23.8 ⁴	19.0 ± 4.6 ⁴	-	4.6 ± 1.5

¹All composites were produced using Nextel™ 610 2D woven fabric and were tested in a 0°/90° orientation

²This sample was only tested under 4PB

³This composite was produced with RBAO powders dried at 300°C for 5h

⁴Only one sample from the AZ-12AG condition and 40% from AZ-13AS failed under interlaminar shear

Representative stress-strain curves of the composites tested in 4-point bending are presented in Figure 62. The fiber volume contents of these composites are indicated in the diagrams. All samples sintered at 1200°C and analyzed in the as-sintered condition (AZ-12AS and both RBAO-matrix composites) present a

stepped stress-strain curve, comparable to those of layered ceramics with weak interfaces [50]. This indicates a high capacity of these materials to tolerate damage, avoiding a catastrophic failure. Lower flexural strengths were achieved for the RBAO-matrix composites (Figure 62(b)) in comparison to the AZ-12AS sample (Figure 62(a)).

The RBAO composite produced with matrix powders dried at room temperature (RB-12AS) presents higher flexural strength and modulus than composite RB_d-12AS, produced with RBAO powders dried at 300°C. This may be attributed to the lower fiber volume content of the latter. If normalized flexural strengths and flexural moduli are analyzed (see Table 5), higher values are obtained for the composite containing less matrix voids (RB_d-12AS).

Comparing the A8Z2-matrix composites (Figure 62(a)), an embrittlement occurs in samples AZ-12AG and AZ-13AS in relation to AZ-12AS, which is consistent with the analysis presented in section 5.3.3. This embrittlement is characterized by a lower strain at fracture, as well as by a reduction in the capability of carrying load after the first failure. While sample AZ-12AS loses only about 20% of its load bearing capacity after the peak stress, AZ-12AG loses approximately 50% and AZ-13AS about 60%. Additionally, in sample AZ-12AS, the first load drop is followed by a graceful, stepwise reduction in stress, whereas in samples AZ-12AG and AZ-13AS it is followed by a plateau, where the stress remains approximately constant in relation to strain.

Figure 63 shows the fracture surface of a representative 4PB sample of the AZ-12AS composite. Failure was accompanied by several interfacial delamination events in multiple layers, mainly at the interfaces between the fiber fabrics and the IB matrix. The same was observed in both RBAO-matrix composites sintered at 1200°C, as shown in Figure 64. In some cases, however, these delamination cracks propagated within the 0° oriented fiber bundles, which generated fiber bridging between adjacent delaminated layers, as indicated in Figure 63(d). After testing, all broken samples remained held together, evidencing the non-catastrophic fracture. For most composites, failure was concentrated in the tensile zone of the specimens, except for sample RB-12AS, which presents bundle buckling in the compressive zone.

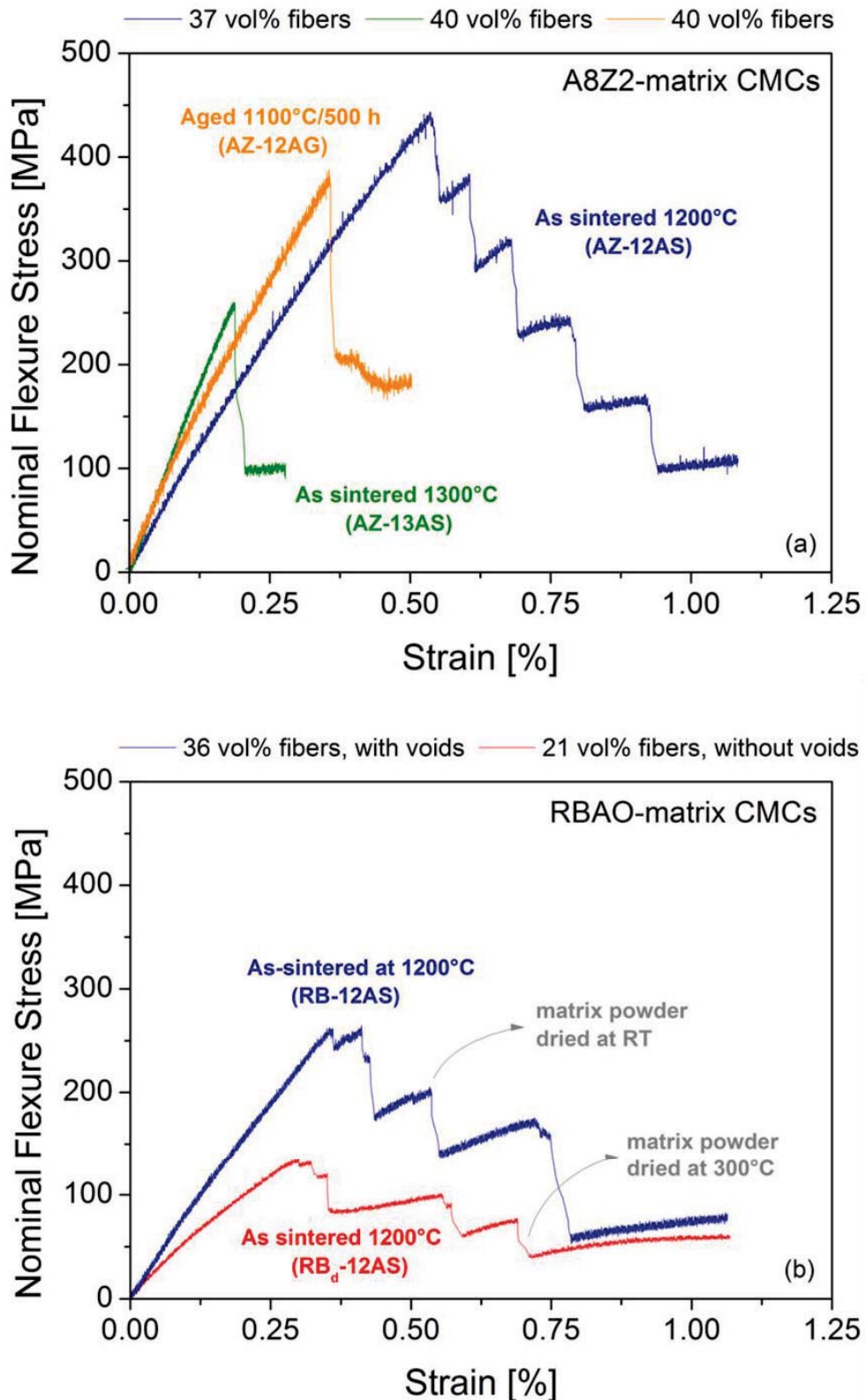


Figure 62: Mechanical behavior of CMCs tested in 4-point bending: (a) A8Z2-matrix composites submitted to different thermal treatments; (b) RBAO-matrix composites manufactured with RBAO powders dried at room temperature (containing matrix voids) and at 300°C (without matrix voids).

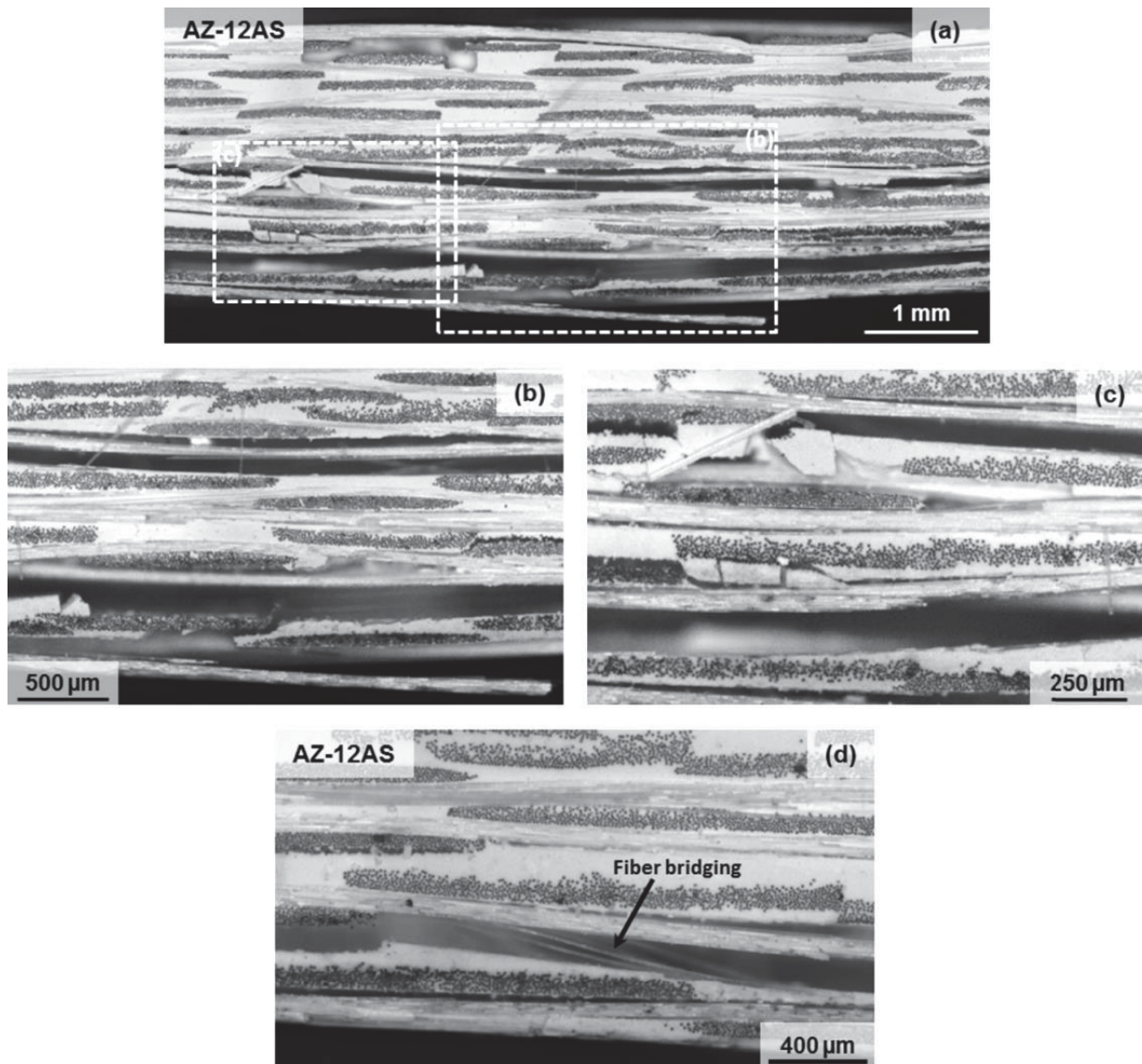


Figure 63: Fracture surface of an A8Z2-matrix composite sintered at 1200°C and tested in 4PB. (b) and (c) show higher magnification pictures of selected areas of (a). Figure (d) shows fibers bridging a delamination crack.

With regard to samples AZ-12AG and AZ-13AS, fracture was dominated by one single crack propagating through two or more layers of the material, followed by one main delamination event, as indicated by the dashed arrows in Figure 65. Again, interfacial delamination occurred predominantly at the interfaces between the fiber fabrics and the IB matrix. All AZ-12AG samples remained held together after testing. Three out of eight AZ-13AS samples broke into two pieces, with minor fiber pullout. Nevertheless, crack deflection was observed at interfaces between matrix and 90° oriented fibers, as predicted by the He and Hutchinson model shown in Figure 47. This can be seen in Figure 65(c), which shows a higher magnification image of the edge crack path in sample AZ-13AS.

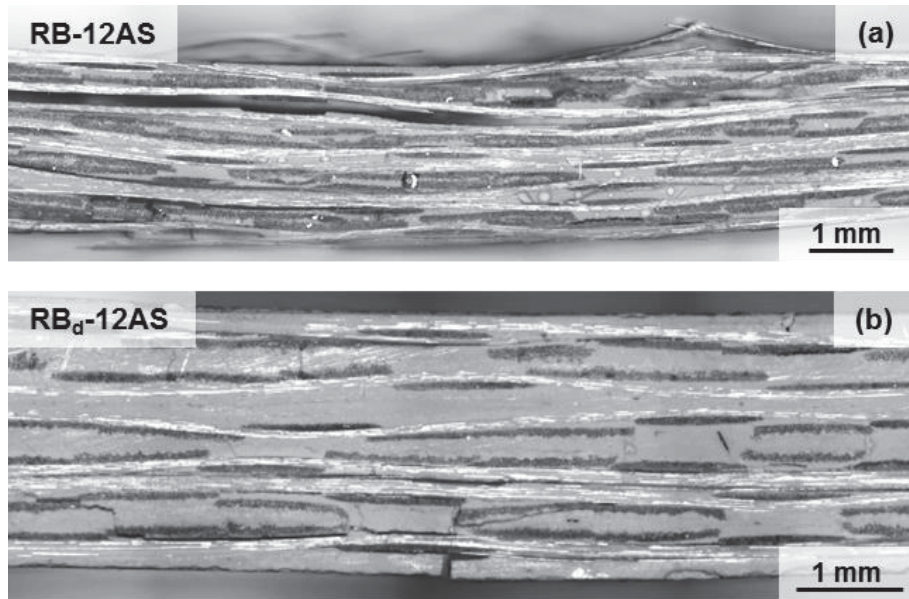


Figure 64: Fracture surfaces of RBAO-matrix composites sintered at 1200°C and tested in 4PB.

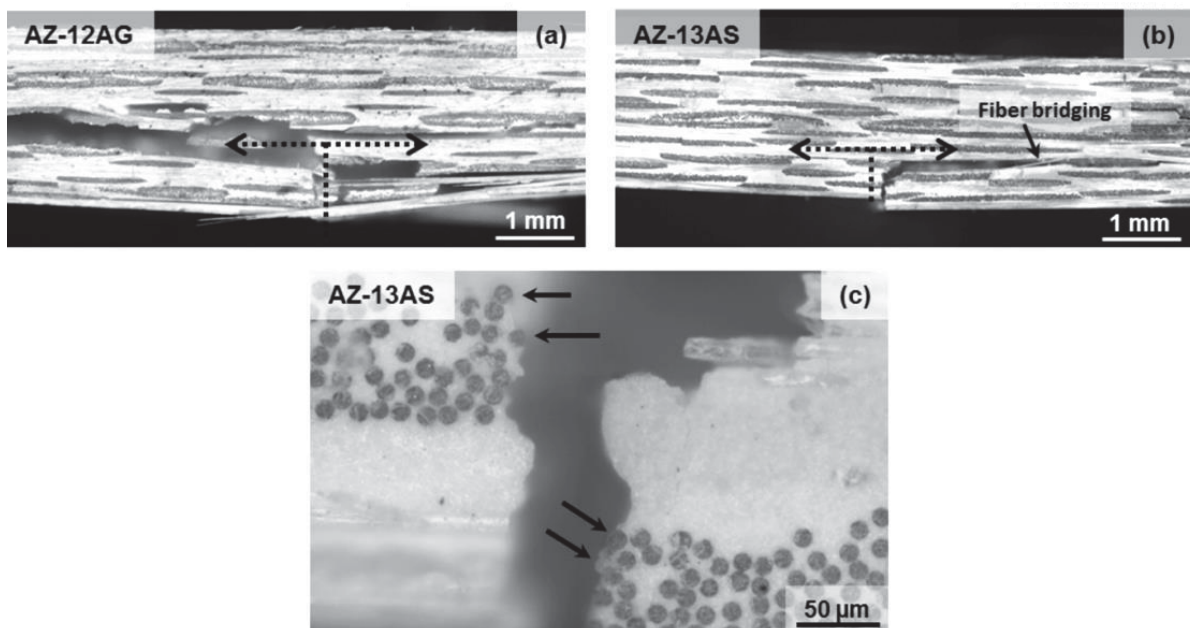


Figure 65: Fracture surfaces of composites AZ-12AG and AZ-13AS. The dashed arrows in (a) and (b) indicate the main crack path. Figure (c) shows a higher magnification picture of the edge crack in sample AS-1300. The solid arrows indicate fibers left intact due to crack deflection.

Apart from the embrittlement, a reduction in the measured flexural strength is observed in the direction of AZ-12AS → AZ-12AG → AZ-13AS, although the fiber volume fractions of composites AZ-12AG and AZ-13AS are slightly higher than that of AZ-12AS. If the normalized flexural strengths are analyzed (Table 5),

the same tendency is observed, being values of 446, 359 and 211 MPa obtained for samples AZ-12AS, AZ-12AG and AZ-13AS, respectively.

This reduction in the flexural strength can be attributed in part to the strength degradation of fibers due to microstructural changes during the heat treatments. In Chapter 3, analysis of polished cross-sections of model composites revealed that polycrystalline alumina fibers endure grain coarsening at temperatures above 1200°C. Here, fiber surfaces of the different A8Z2-matrix composites are investigated. By sintering the composites at 1200°C for 30 min, no significant change in fiber microstructure occurs, so that surfaces are still smooth after sintering (Figure 66(a) and (b)). By ageing this composite at 1100°C for 500 h, the fiber surfaces become considerably rougher, indicating that grain growth may occur even at a relatively low temperature (Figure 66(c) and (d)). As for the samples sintered at 1300°C, apart from the fiber grain growth, some pores were detected on the fiber surfaces (Figure 66(e) and (f)). Additionally, the amount of particles adhered to the fiber surfaces in samples AZ-12AG and AZ-13AS seems to be higher than in the AZ-12AS composite. This feature indicates the strengthening of matrix and consequently of fiber-matrix interfaces during ageing at 1100°C or sintering at 1300°C.

Other indicative of matrix strengthening due to densification is the increase in flexural moduli in the direction of AZ-12AS → AZ-12AG → AZ-13AS. This increase is also observed if the normalized flexural moduli are compared (Table 5). The strengthening of the matrix and, consequently, of the fiber-matrix interfaces may also have an effect on the reduction of flexural strengths, since denser matrices lead to larger stress concentrations in the presence of a crack, favoring a correlated fiber failure [9].

Results of apparent interlaminar shear strength measured by short beam shear are shown in Table 5. A value of 13.3 ± 1.6 MPa was obtained for sample AZ-12AS, which is in good agreement with values reported in the literature for other oxide CMCs tested under short beam shear [6,120,121]. Figure 67 shows the fracture surfaces of representative SBS samples. The arrows in the left-hand side of the pictures indicate the position of the interlaminar cracks. Multiple cracking occurred in samples sintered at 1200°C and analyzed in the as-sintered condition (Figure 67(a) and (b)). Fracture was dominated by one or two cracks in samples

AZ-12AG and AZ-13AS (Figure 67(c) and (d)). In all samples, failure occurred mainly by debonding between the fiber fabrics and the IB matrix, with minor matrix failure. The higher ILSS values of samples AZ-12AG and AZ-13AS are therefore a result of the strengthening of fiber-matrix interfaces due to matrix densification. All AZ-12AS and RB_d-12AS specimens failed under shear, while tensile fracture was observed in most of the AZ-12AG and AZ-13AS samples.

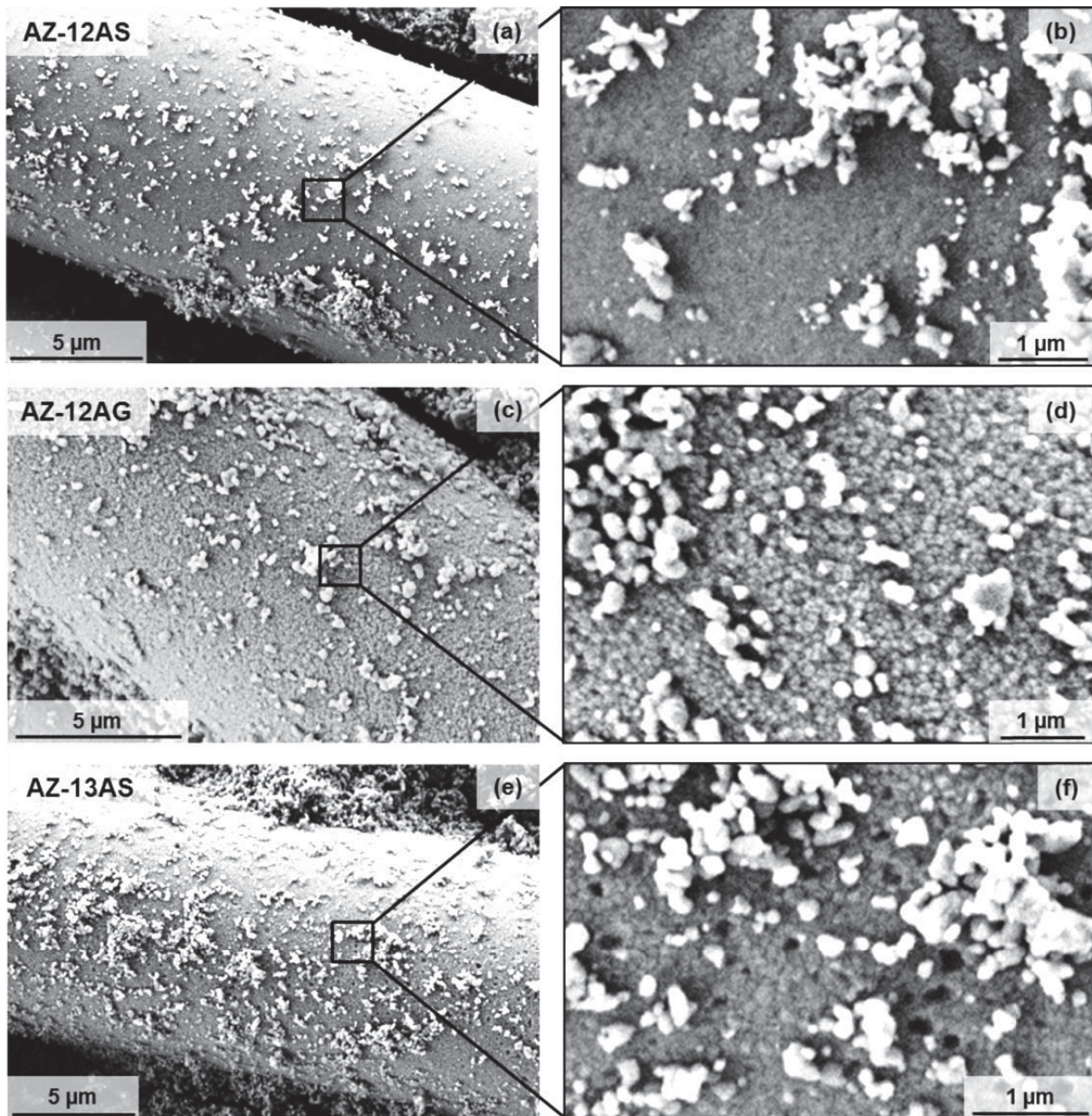


Figure 66: Fiber surfaces of A8Z2-matrix composites submitted to the different heat treatments analyzed in this work.

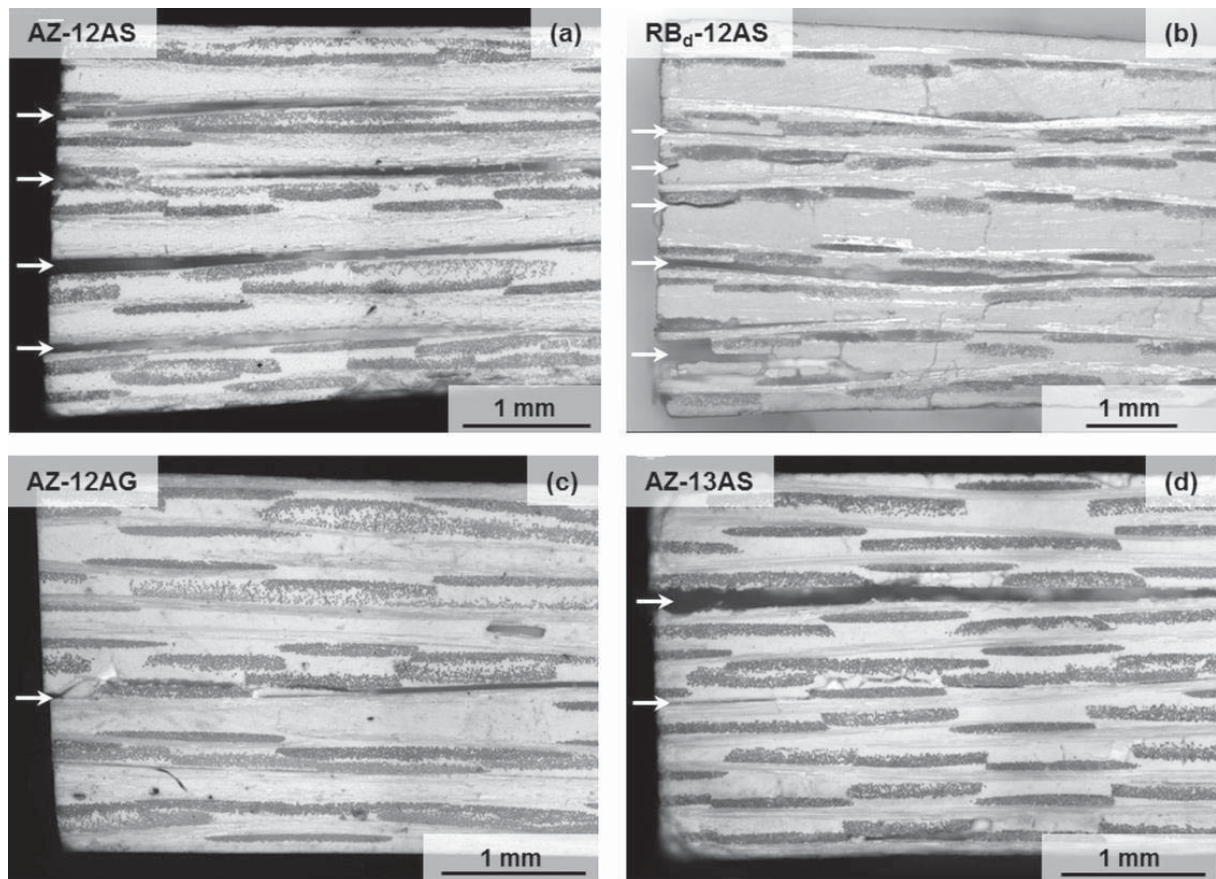


Figure 67: Fracture surfaces of composite samples tested in short beam shear.

7.4 Discussion

Predictions of crack deflection/penetration according to the He and Hutchinson model shown in section 5.3.3 indicated that, in case of AZ-12AS composites, crack deflection was expected not only at the fiber-matrix interfaces, but also at the interfaces between the IB and IT matrices. It was therefore anticipated that these composites could profit from toughening mechanisms of both fiber-reinforced composites and multilayered ceramics.

Results presented in this chapter show that, although no interfacial delamination was observed at the IB-IT interfaces, a stepped stress-strain curve characteristic of multilayered ceramics was obtained for composites sintered at 1200°C and analyzed in the as-sintered condition. Nevertheless, in contrast to layered ceramics, interfacial delamination did not occur here between two monolithic ceramic layers. Instead, the weak interfaces between the fiber fabrics and the IB matrix were responsible for the layer-by-layer failure observed in these materials. The fact that



the 2D reinforcing fabrics were oriented perpendicularly to the applied load during testing favored this behavior.

A consequence of this layer-by-layer fracture is a discrete reduction in the thickness of the composites during flexural tests. Every time a layer fails, the effective thickness of the material reduces, thereby decreasing its stiffness and decreasing the force necessary to break the subsequent layer. As a result, stepped force-displacement curves are obtained. This variation in thickness was however not taken into account in the calculation of the nominal stresses shown in Figure 62. These stresses are therefore *engineering stresses*, since they were calculated from the force-displacement data considering a constant value of thickness equal to the initial thickness of the specimens.

Apart from the stiffness decrease due to the sequential reduction in specimen thickness, another factor that may have contributed to a decreasing stress-strain slope after each layer failure is the propagation of delamination cracks in a direction perpendicular to the applied load. It has been reported elsewhere [122] that such cracks usually propagate at a constant force. Such behavior is observed here in samples AZ-12AG and AZ-13AS, for which the stress plateau after the first failure coincides with crack bifurcation, as shown in Figure 65. The higher stress concentrations associated with the denser matrices of these materials in relation to that of AZ-12AS caused a correlated failure of more than one layer at the same time, so that a stepped stress-strain curve was no longer observed.

In the next sections, the effects of heat treatment and RBAO powder drying condition on the mechanical properties of A8Z2 and RBAO-matrix composites, respectively, will be discussed.

7.4.1 Effect of heat treatment on A8Z2-matrix composites

The best mechanical behavior under 4-point bending was shown by sample AZ-12AS, which combined a high flexural strength with a graceful reduction in the load bearing capacity. The several delamination events during fracture of this composite (both in 4PB and in SBS) indicate the presence of very weak interfaces, mainly between fibers and the IB matrix. Although the stress-strain behavior of this composite is comparable to that of multilayered ceramics, the strain to failure of AZ-12AS is further enhanced by fiber-related toughening mechanisms, such as

crack deflection at fiber-matrix interfaces and subsequent fiber bridging, which are not present in conventional layered ceramics.

Although to a lesser extent than composite AZ-12AS, samples AZ-13AS and AZ-12AG also presented a damage tolerant behavior, comparable to most all-oxide CMCs reported in the literature [9,65,120]. Their stress-strain curves presented a slight non-linearity upon loading, as well as a higher strain at fracture than monolithic ceramics. This is in part due to crack deflection at fiber-matrix interfaces, which occurred even in these rather brittle composites, confirming predictions based on the He and Hutchinson model (Figure 47). In addition, samples AZ-12AG and AZ-13AS present a reduced load bearing capacity after the first failure, characterized by a stress plateau at about 40% to 50% of their flexural strength. This “steady-state” is associated with delamination (crack bifurcation) occurred at fiber-matrix interfaces (Figure 65(a) and (b)).

The large stress drop of samples AZ-12AG and AZ-13AS following the peak stresses can be attributed to the amount of layers broken at the first fracture. While failure in AZ-12AS occurred in single layers, a correlated fracture of more than one layer occurred in samples AZ-13AS and AZ-12AG. The increase in the flexural moduli and interlaminar properties of samples AZ-12AG and AZ-13AS in relation to AZ-12AS indicates the strengthening of matrices and interfaces during the respective thermal treatments. It is therefore assumed that the decrease in matrix porosity causes a higher stress concentration around broken fibers, favoring a correlated fiber failure. As a result, both composite strength and damage tolerance are reduced. Moreover, fiber grain growth and the accompanying microstructural changes, such as surface roughness and pore coarsening also contribute to the decrease in strength of these composites in comparison to the AZ-12AS.

If only the contribution of the fibers to the composite strength is taken into account, then the strength of a long fiber reinforced composite can be estimated by the rule of mixtures according to Eq. 3. In practice, however, efficiency factors should be introduced to account, e.g., for fiber orientation (β) [123] and for the fiber integrity after processing (φ) [124], so that:

$$\sigma_{c_u} = \beta \varphi v_f \sigma_{f_u} \quad \text{Eq. 32}$$

where $\beta = 1/2$ for composites in a $0^\circ/90^\circ$ configuration, since only half of the bundles are mechanically required during loading [123]. In this equation, σ_{f_u} is the tensile strength of the as-received fibers (3100 MPa for Nextel™ 610, according to the supplier [58]) and v_f is the fiber volume fraction.

As a means to assess the effect of heat treatment on the flexural strength obtained for the different A8Z2-matrix composites, values of φ can be estimated and compared. Figure 68 shows the flexural strength values measured on the A8Z2-matrix composites as a function of fiber volume content, together with calculations of composite strength according to Eq. 32, assuming different values of φ . This is a rudimentary way of evaluating how much of the maximum theoretical strength value (for which $\varphi = 1$) was achieved in the samples produced in this work. Values of φ obtained for AZ-12AS samples are $\sim 78\%$, but decrease to $\sim 63\%$ when this composite is aged at 1100°C for 500 h (AZ-12AG). When the A8Z2-matrix composite is sintered at 1300°C , however, values of only $\sim 37\%$ are obtained.

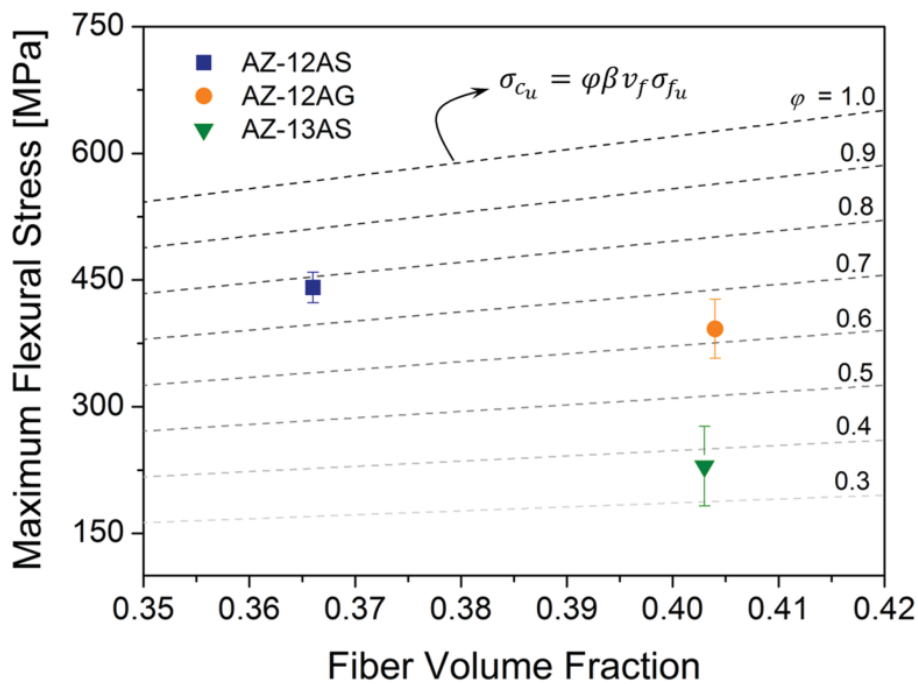


Figure 68: Maximum nominal stress as a function of fiber volume fraction for the different A8Z2-matrix CMCs analyzed in this work. The dashed lines indicate predictions of composite strength according to Eq. 32, considering $\beta = 0.5$, $\sigma_{f_u} = 3.1$ GPa, and different values of efficiency factor (φ).

This decrease in the efficiency factor φ is consistent with microstructural changes endured by the fibers during the respective heat treatments (see Figure 66) and

suggests, again, that 1200°C is the best sintering temperature in order to manufacture high strength composites.

It is important to note that strength values measured in bending are being compared here to theoretical values calculated considering axial loading. Nevertheless, it has been reported that stress values obtained from bending tests on both CMCs and layered ceramics generally exceed the values measured in tension [46,125–127]. This would lead to an overestimation of φ . However, the significant differences observed in the φ values for the different composites analyzed here suffice for the comparison purposes of this work.

Finally, it is important to mention that the fracture mechanisms of multilayered materials under bending depend considerably on the sample orientation during testing [128]. In the present work, multilayered fiber-reinforced composites were loaded in a direction perpendicular to the laminate plane. This sample orientation induces a layer-by-layer failure and facilitates deflection of cracks at weak interfaces, particularly between the fiber fabrics and the IB matrix. If the same material is loaded in a direction parallel to the laminate plane, all composite layers may fail together, considerably reducing the apparent strain at failure of the material [128]. Nevertheless, based on the current state of this research, it is proved that multilayered fiber-reinforced composites produced by the novel lamination route using the A8Z2 matrix and sintered at 1200°C present very promising mechanical properties, characterized by a high flexural strength, accompanied by high energy dissipation during fracture. If this material is to be used at 1100°C, the stepped stress-strain behavior may be lost, but fiber-related toughening mechanisms will still guarantee damage tolerance and a larger strain at fracture than monolithic ceramics.

7.4.2 Effect of powder drying condition on RBAO-matrix composites

Differences in the mechanical behavior of samples RB-12AS and RB_d-12AS (Figure 62(b)) can be attributed to their different fiber volume fractions, as well as to the presence of matrix voids on sample RB-12AS. As mentioned in Chapter 6, the latter contains an average of 6.27 vol% voids, originated from the evolution of gases from the powder surfaces during prepreg manufacturing.



Although lower values of flexural strength and flexural modulus were obtained for sample RB_d-12AS in relation to RB-12AS, higher values are expected for the former if these properties are normalized to a common fiber volume fraction. This indicates that the matrix voids in RB-12AS negatively affect the strength of this material and, certainly, reduce its flexural modulus with respect to a similar material without voids. This is consistent with other studies on the effects of matrix voids on the properties of polymer matrix composites [129–132].

The detrimental effects of voids are usually more pronounced in matrix dominated properties such as interlaminar shear strength and compressive strength [130,131]. This may explain why specimens from the RB-12AS composite endured buckling and subsequent fracture of fiber bundles in the compressive zone during 4-point bending. Such compressive failure is normally favored by low matrix shear strengths or weak fiber-matrix interfaces, since at least one of these two components must fail in order for microbuckling to occur [35,132,133].

7.4.3 Comparison between RBAO-matrix and A8Z2-matrix composites

Even if normalized values of peak stress and flexural modulus are analyzed, RBAO-matrix composites present inferior properties to the reference A8Z2-matrix composites. Contributing to this behavior are the presence of matrix voids in composite RB-12AS and the existence of delamination cracks in the as-processed RB_d-12AS sample (see Figure 61). These delamination cracks may also have contributed to the lower ILSS value measured for RB_d-12AS in relation to those obtained for the A8Z2-matrix composites.

By performing additional mechanical tests on RBAO-matrix composites free of delamination and with a systematical variation of the void content, it may be possible to provide experimental evidence to support these hypotheses. Nevertheless, as discussed in Chapter 6, controlling the manufacturing process of RBAO-matrix composites is not straightforward. This more detailed investigation could not be accomplished in the time frame of this work and remains here as suggestion for future investigation.

Nonetheless, based on the current state of this research, it is concluded that composites produced with a simple, pure oxide matrix (A8Z2) are superior to RBAO-matrix composites, both in microstructure and in mechanical properties.

This leads again to the conclusion that for sintering temperatures lower than 1300°C, the use of the elaborated RBAO process to consolidate defect-free composite matrices is not justified.

7.5 Conclusion

In this chapter, it has been shown that multilayered, all-oxide composites produced by the novel lamination route developed in this work combine fracture mechanisms from both layered ceramics and fiber reinforced CMCs. All composites sintered at 1200°C present a saw-like stress-strain curve, indicating the ability of these materials to tolerate damage and continue carrying reduced loads after the first failure.

RBAO-matrix composites presented lower flexural strengths and flexural moduli than the reference A8Z2-matrix composites, which is attributed to the presence of matrix voids and process-related delamination.

The best mechanical behavior was shown by the A8Z2-matrix composite sintered at 1200°C, which presented a high flexural strength, followed by a stepped stress reduction upon further straining. Ageing of this composite at 1100°C for 500 h caused a sharp reduction in the load bearing capacity after the peak stress. The same was observed in the A8Z2-matrix sample sintered at 1300°C. Nevertheless, fiber-related toughening mechanisms such as crack deflection at fiber matrix interfaces and subsequent bridging were still present in these composites, leading to a non-linear stress-strain behavior up to failure.





8 Summary

This work primarily aimed at investigating the use of a reactive sintering matrix (RBAO) to prevent the formation of shrinkage-related matrix cracks in CMCs. Due to the high reactivity of the aluminum particles present in the RBAO, a new processing route was developed, in which thermoplastic prepregs are manufactured by a two-step impregnation process using organic-based suspensions. Advantages of this novel route include:

- (i) A better filling of the available free spaces in woven fabrics, leading to a more homogenous distribution of matrix particles and, therefore, contributing to the mitigation of matrix cracks in the green state;
- (ii) The possibility of shaping and joining composites in the green state due to the thermoplastic behavior of the paraffin-based suspension used for prepreg manufacture;
- (iii) The long shelf-life of the thermoplastic prepregs, which can be easily handled and stored at room temperature.

By using this route, the production of full-scale, RBAO-matrix composites was shown, for the first time, to be feasible. Nevertheless, several challenges were experienced during the development of these composites. Formation of large matrix voids due to gas evolution from the RBAO particle surfaces and incomplete oxidation of large aluminum particles in powders with high aluminum contents are examples of these challenges. Moreover, several additional processing steps are necessary for the manufacture of RBAO-matrix composites, such as long attrition milling periods and the determination of zero-shrinkage compositions as a function of sintering temperature and powder drying condition.

Superior results were obtained using a reference, pure oxide matrix consisting of 80 vol% Al_2O_3 and 20 vol% t-ZrO_2 (A8Z2 matrix). The combination of the novel route with this matrix system was already effective in mitigating crack formation in the all-oxide CMCs. The addition of zirconia was shown to shift the onset of alumina densification to higher temperatures, such that the A8Z2 matrix system



can be sintered with very low shrinkages up to 1300°C, which enables the mitigation of matrix cracks up to this temperature. Very homogeneous microstructures and fiber volume contents up to ~40 vol% were obtained for the A8Z2-matrix composites. Moreover, the mechanical properties of these reference materials were superior to those of RBAO-matrix composites.

Composites were analyzed after three different heat treatments, namely as-sintered at 1200°C, sintered at 1200°C and aged at 1100°C for 500 h and as-sintered at 1300°C. These temperatures were selected after preliminary investigation of crack deflection on model composites. When tested under 4-point bending, a combination of fracture mechanisms from both layered ceramics and fiber reinforced CMCs was observed for the all-oxide composites produced by the novel lamination route. The best properties were obtained for the A8Z2-matrix composites sintered at 1200°C. An average flexural strength of 440 MPa was obtained, together with a stepwise stress reduction after the first failure. When ageing this composite at 1100°C, the stepped stress-strain behavior is lost, but fiber-related toughening mechanisms such as crack deflection and bridging still ensure inelastic deformation up to failure. RBAO-matrix composites sintered at 1200°C also presented a saw-like stress-strain curve, although the maximum attained stresses were lower than those obtained for the A8Z2-matrix composites. This was attributed to processing-induced defects such as large matrix voids and delamination.

Although the results obtained with the RBAO matrix were not satisfactory, the purpose of using this matrix material was fundamental for the two main findings of this work: (i) the development of a processing route that helps mitigating matrix cracks in the green state and (ii) the use of a simple A8Z2 matrix, which presents very low shrinkages and helps hindering crack formation during sintering. Therefore, the objective of mitigating matrix cracks in CMCs was indirectly achieved in this work, without the need of introducing the elaborated RBAO technique to the processing route.

Therefore, up to a sintering temperature of 1300°C, the use of RBAO to consolidate defect-free CMC matrices is not justified. This will be only interesting when more temperature-stable, new generation oxide fibers are available, which can withstand sintering and service temperatures higher than 1300°C. Above this



temperature, the A8Z2 matrix endures larger shrinkages and will no longer suffice to mitigate the formation of matrix cracks. Although this work presented a feasible methodology to produce full-scale, RBAO-matrix composites, challenges such as void formation, process-related delamination and ineffective milling of RBAO powders containing large amounts of aluminum still remain and should be addressed if this matrix system is to be successfully applied in all-oxide composites.





References

- [1] Chawla, K.K. *Ceramic Matrix Composites*. 2nd ed. Boston: Kluwer Academic Publishers; 2003.
- [2] Lamon, J. Interfaces and Interphases. In: Krenkel, W., editor. *Ceramic Matrix Composites: Fiber reinforced Ceramics and their Applications*. Weinheim: WILEY-VCH Verlag GmbH & Co; 2008. p. 49–67.
- [3] Schmücker, M.; Mechnich, P. All-oxide ceramic matrix composites with porous matrices. In: Krenkel, W. editor. *Ceramic Matrix Composites: Fiber reinforced Ceramics and their Applications*. Weinheim: WILEY-VCH Verlag GmbH & Co; 2008. p. 205–229.
- [4] Zok, F.W. Developments in oxide fiber composites. *J. Am. Ceram. Soc.* 2006;89:3309–24.
- [5] Zok F.W.; Levi, C.G. Mechanical properties of porous-matrix ceramic composites. *Adv. Eng. Mater.* 2001;3:15–23.
- [6] Simon, R.A. Progress in processing and performance of porous-matrix oxide/oxide composites. *Int. J. Appl. Ceram. Technol.* 2005;2:141–9.
- [7] Levi, C.G.; Yang, J.Y.; Dalgleish, B.J.; Zok, F.W.; Evans, A.G. Processing and performance of an all-oxide ceramic composite. *J. Am. Ceram. Soc.* 1998;81:2077–86.
- [8] Rüdinger, A.; Pritzkow, W. Die Entwicklung oxidkeramischer Faserverbundwerkstoffe am Fraunhofer ISC/Zentrum HTL in Zusammenarbeit mit W.E.C Pritzkow Spezialkeramik. *Keramische Zeitschrift* 2013;03:166–9.
- [9] Mattoni, M.A.; Yang, J.Y.; Levi, C.G.; Zok, F.W. Effects of matrix porosity on the mechanical properties of a porous-matrix, all-oxide ceramic composite. *J. Am. Ceram. Soc.* 2001;84:2594–602.
- [10] Mah, T.; Keller, K.A.; Cinibulk, M.K. Method of making crack-free ceramic matrix composites(US 8,562,901 B1); 2009.
- [11] Dryden, J.; Zok, F.W. Thermal resistance of bridged cracks in fiber-reinforced ceramic composites. *J. Appl. Phys.* 2001;89:4599–611.



- [12] McDonald, K.R.; Dryden, J.R.; Zok, F.W. Effects of matrix cracks on the thermal diffusivity of a fiber-reinforced ceramic composite. *J. Am. Ceram. Soc.* 2001;84:2015–21.
- [13] Yang, J.; Weaver, J.H.; Zok, F.W.; Mack, J.J. Processing of oxide composites with three-dimensional fiber architectures. *J. Am. Ceram. Soc.* 2009;92:1087–92.
- [14] Janssen, R.; Scheppokat, S.; Claussen, N. Tailor-made ceramic-based components - advantages by reactive processing and advanced shaping techniques. *J. Eur. Ceram. Soc.* 2008;28:1369–79.
- [15] Claussen, N.; Le, T.; Wu, S. Low-shrinkage reaction-bonded alumina. *J. Eur. Ceram. Soc.* 1989;5:29–35.
- [16] Holz, D.; Wu, S.; Scheppokat, S.; Claussen, N. Effect of processing parameters on phase and microstructure evolution in RBAO ceramics. *J. Am. Ceram. Soc.* 1994;77:2509–17.
- [17] Janssen, R.; Wendorff, J.; Claussen, N. Fiber reinforcement of reaction bonded oxide ceramics. In: Evans, A.G., Naslain, R., editors. *High-Temperature Ceramic-Matrix Composites II: Manufacturing and Materials Development*. Westerville: The American Ceramic Society; 1995. p. 167–173.
- [18] Keller, K.A.; Mah, T.; Boakye, E.E.; Parthasarathy, T.A. Gel-casting and reaction bonding of oxide- oxide minicomposites with monazite interphase. *Ceramic Engineering and Science Proceedings*. 2000;21:525–34.
- [19] Wendorff, J. *Synthese und Eigenschaften langfaserverstärkter oxidkeramischer Verbundwerkstoffe für Hochtemperaturanwendungen*. Düsseldorf: VDI Verlag GmbH; 1997.
- [20] Goushegir, S.M. *Investigation of fiber-matrix compatibility in oxide ceramic matrix composites*. Master Thesis. Institute of Advanced Ceramics, Hamburg University of Technology; 2010.
- [21] Hablitzel, M.P. *Processing and characterization of Al₂O₃/RBAO CMCs produced by a prepreg technique*. Bachelor Thesis. Institute of Advanced Ceramics, Hamburg University of Technology; 2012.
- [22] Evans, A.G. Perspective on the development of high-toughness ceramics. *J. Am. Ceram. Soc.* 1990;73:187–206.

- [23] Jefferson, G.; Keller, K.A.; Hay, R.S.; Kerans, R.J. Oxide/oxide composites with fiber coatings. In: Krenkel, W., editor. *Ceramic Matrix Composites: Fiber reinforced Ceramics and their Applications*. Weinheim: WILEY-VCH Verlag GmbH & Co; 2008. p. 187–204.
- [24] Krenkel, W. *Ceramic Matrix Composites: Fiber reinforced Ceramics and their Applications*. Weinheim: WILEY-VCH Verlag GmbH & Co; 2008.
- [25] Naslain, R.; Harris, B. *Ceramic Matrix Composites: Components, preparation, microstructure, and properties*. London: Elsevier Applied Science; 1990.
- [26] Motz, G.; Schmidt, S.; Beyer, S. The PIP-process: precursor properties and applications. In: Krenkel, W., editor. *Ceramic Matrix Composites: Fiber reinforced Ceramics and their Applications*. Weinheim: WILEY-VCH Verlag GmbH & Co; 2008. p. 165–184.
- [27] Christin, F. CMC materials for space and aeronautical applications. In: Krenkel, W., editor. *Ceramic Matrix Composites: Fiber reinforced Ceramics and their Applications*. Weinheim: WILEY-VCH Verlag GmbH & Co; 2008. p. 327–351.
- [28] Weiß, R. Carbon/carbons and their industrial applications. In: Krenkel, W., editor. *Ceramic Matrix Composites: Fiber reinforced Ceramics and their Applications*. Weinheim: WILEY-VCH Verlag GmbH & Co; 2008. p. 69–111.
- [29] Sambell, R.A.J.; Briggs, A.; Phillips, D.C.; Bowen, D.H. Carbon fibre composites with ceramic and glass matrices: Part 2: Continuous fibers. *J. Mater. Sci.* 1972;7:676–81.
- [30] Phillips, D.C.; Sambell, R.A.J.; Bowen, D.H. The mechanical properties of carbon fibre reinforced pyrex glass. *J. Mater. Sci.* 1972;7:1454–64.
- [31] Heidenreich, B. Melt infiltration process. In: Krenkel, W., editor. *Ceramic Matrix Composites: Fiber reinforced Ceramics and their Applications*. Weinheim: WILEY-VCH Verlag GmbH & Co; 2008. p. 113–139.
- [32] Leuchs, M. Chemical vapor infiltration processes for ceramic matrix composites: manufacturing, properties, applications. In: Krenkel, W., editor. *Ceramic Matrix Composites: Fiber reinforced Ceramics and their Applications*. Weinheim: WILEY-VCH Verlag GmbH & Co; 2008. p. 141–164.

- [33] Koch, D. Microstructural modeling and thermomechanical properties. In: Krenkel, W., editor. *Ceramic Matrix Composites: Fiber reinforced Ceramics and their Applications*. Weinheim: WILEY-VCH Verlag GmbH & Co; 2008. p. 231–259.
- [34] Naslain, R. The design of the fibre-matrix interfacial zone in ceramic matrix composites. *Composites Part A* 1998;29A:1145–55.
- [35] Hull, D.; Clyne, T.W. *An introduction to composite materials*. 2nd ed. Cambridge: Cambridge University Press; 1996.
- [36] Lamon, J. A micromechanics-based approach to the mechanical behavior of brittle-matrix composites. *Compos. Sci. and Techn.* 2001;61:2259–72.
- [37] Kerans, R.J.; Hay, R.S.; Parthasarathy, T.A.; Cinibulk, M.K. Interface design for oxidation-resistant ceramic composites. *J. Am. Ceram. Soc.* 2002;85:2599–632.
- [38] Davis, J.B.; Löfvander, J.P.A., Evans, A.G.; Bischoff, E.; Emiliani, M.L. Fiber coating concepts for brittle-matrix composites. *J. Am. Ceram. Soc.* 1993;76.
- [39] Davis, J.B.; Marshall, D.B.; Morgan, P.E.D. Monazite-containing oxide/oxide composites. *J. Eur. Ceram. Soc.* 2000;20:583–7.
- [40] He, M.; Hutchinson, J.W. Crack deflection at an interface between dissimilar elastic materials. *Int. J. Solids Struct.* 1989;25:1053–67.
- [41] Koch, D.; Tushtev, K.; Grathwohl, G. Ceramic fiber composites: Experimental analysis and modeling of mechanical properties. *Compos. Sci. Techn.* 2008;68:1165–72.
- [42] Fujita, H.; Jefferson, G.; McMeeking, R.M.; Zok, F.W. Mullite/alumina mixtures for use as porous matrices in oxide fiber composites. *J. Am. Ceram. Soc.* 2004;87:261–7.
- [43] Cao, H.; Thouless, M.D. Tensile tests of ceramic-matrix composites: theory and experiment. *J. Am. Ceram. Soc.* 1990;73:2091–4.
- [44] Evans, A.; Marshall, D. Overview no. 85 The mechanical behavior of ceramic matrix composites. *Acta Metall.* 1989;37:2567–83.
- [45] Keller, K.A.; Jefferson, G.; Kerans, R.J. Oxide-oxide composites. In: Bansal NP, editor. *Handbook of Ceramic Composites*. Boston: Kluwer Academic Publishers; 2005. p. 377–421.

- [46] Marshall, D.B.; Evans, A.G. Failure mechanisms in ceramic-fiber/ceramic-matrix composites. *J. Am. Ceram. Soc.* 1985;68:225–31.
- [47] Callister, W.D. *Materials Science and Engineering: An Introduction*. 5th ed.: John Wiley & Sons, Inc; 2000.
- [48] Clauß, B. Fibers for ceramic matrix composites. In: Krenkel, W., editor. *Ceramic Matrix Composites: Fiber reinforced Ceramics and their Applications*. Weinheim: WILEY-VCH Verlag GmbH & Co; 2008. p. 1–20.
- [49] Rebillat, F.; Lamon, J.; Naslain, R. Properties of multilayered interphases in SiC/SiC chemical-vapor-infiltrated composites with “weak” and “strong” interfaces. *J. Am. Ceram. Soc.* 1998;81:2315–26.
- [50] Clegg, W.J.; Kendall, K.; Alford, N.M.; Button, T. W., Brichall, J.D. A simple way to make tough ceramics. *Nature* 1990;347:455–7.
- [51] Bermejo, R.; Danzer, R. High failure resistance layered ceramics using crack bifurcation and interface delamination as reinforcement mechanisms. *Eng. Fract. Mech.* 2010;77:2126–35.
- [52] Davis, J.B.; Marshall, D.B.; Morgan, P.E.D. Oxide composites of Al₂O₃ and LaPO₄. *J. Eur. Ceram. Soc.* 1999;19:2421–6.
- [53] Lange, F.F.; Tu, W.C.; Evans, A.G. Processing of damage-tolerant, oxidation-resistant ceramic matrix composites by a precursor infiltration and pyrolysis method. *Mater. Sci. Eng., A* 1995;A195:145–50.
- [54] Tu, W.C.; Lange, F.F.; Evans, A.G. Concept for a damage-tolerant ceramic composite with “strong” interfaces. *J. Am. Ceram. Soc.* 1996;79:417–24.
- [55] Heathcote, J.A.; Gong, X.; Yang, J.Y.; Ramamurty, U.; Zok, F.W. In-plane mechanical properties of an all-oxide ceramic composite. *J. Am. Ceram. Soc.* 1999;82:2721–30.
- [56] Zok, F.W.; Lange, F.F. Packing density of composite powder mixtures. *J. Am. Ceram. Soc.* 1991;74:1880–5.
- [57] Fujita, H.; Levi, C.G.; Zok, F.W. Controlling mechanical properties of porous mullite/alumina mixtures via precursor-derived alumina. *J. Am. Ceram. Soc.* 2005;88.
- [58] 3M Ceramic Textiles and Composites. Nextel™: Ceramic Textiles Technical Notebook.

- [59] Carelli, E.A.V.; Fujita, H.; Yang, J.Y.; Zok, F.W. Effects of thermal aging on the mechanical properties of a porous-matrix ceramic composite. *J. Am. Ceram. Soc.* 2002;85:595–602.
- [60] Saruhan, B. *Oxide-Based Fiber-Reinforced Ceramic-Matrix Composites: Principles and Materials*. Boston: Kluwer Academic Publishers; 2003.
- [61] Kanka, B.; Schneider, H. Aluminosilicate fiber/mullite matrix composites with favorable high-temperature properties. *J. Eur. Ceram. Soc.* 2000;20:619–23.
- [62] Pritzkow, W.E. Oxide-Fiber-Reinforced Oxide Ceramics. *cfi/Ber. DKG* 2008;85:E31-E35.
- [63] Machry, T.; Koch, D.; Wilhelmi, C. Development of a new oxide ceramic matrix composite. In: Krenkel, W., Lamon, J., editors. *High Temperature Ceramic Materials and Composites*. Berlin: AVISO Verlagsgesellschaft mbH; 2010. p. 435–445.
- [64] Wamser, T.; Scheler, S.; Lehmann, J.; Krenkel, W. Novel processing of porous oxide matrix composites. In: Krenkel, W., Lamon, J., editors. *High Temperature Ceramic Materials and Composites*. Berlin: AVISO Verlagsgesellschaft mbH; 2010. p. 479–484.
- [65] Holmquist, M.G.; Lange, F.F. Processing and properties of a porous oxide matrix composite reinforced with continuous oxide fibers. *J. Am. Ceram. Soc.* 2003;86:1733–40.
- [66] Schmücker, M.; Reh, S. Faserverstärkte, oxidische Keramiken für Hochtemperaturanwendungen. *Konstruktion* 2010;6:8–9.
- [67] Simon, R.A.; Danzer, R. Oxide fiber composites with promising properties for high-temperature structural applications. *Adv. Eng. Mater.* 2006;8:1129–34.
- [68] DIN Deutsches Institut für Normung e.V. Mechanical properties of ceramic composites at room temperature - Part 5: Determination of interlaminar shear strength by short span bend test (three points);81.060.30(DIN EN 658-5:2003-03). Berlin: Beuth Verlag GmbH; 2003.
- [69] DIN Deutsches Institut für Normung e.V. Mechanical properties of ceramic composites at room temperature - Part 3: Determination of flexural strength;81.060.30(DIN EN 658-3:2002-11). Berlin: Beuth Verlag GmbH; 2002.

- [70] Claussen, N.; Travitzky, N.A.; Wu, S. Tailoring of reaction-bonded Al₂O₃ (RBAO) ceramics. *Ceram. Eng. Sci. Proc.* 1990;11:806–20.
- [71] Wu, S.; Claussen, N. Reaction-bonding of ZrO₂-containing Al₂O₃. *Solid State Phenom.* 1992;25-26:293–300.
- [72] Janssen, R.; Claussen, N.; Scheppokat, S.; Roeger, M. Reaction bonding and reactive sintering: a way to low cost manufacturing of alumina based components. *Materials Integration* 2002;15:75–9.
- [73] Claussen, N.; Janssen, R.; Holz, D. Reaction bonding of aluminum oxide (RBAO): Science and technology. *J. Ceram. Soc. Jpn.* 1995;103.
- [74] Watson, M.J.; Chan, H.M.; Harmer, M.P.; Caram, H.S. Effects of milling liquid on the reaction-bonded aluminum oxide process. *J. Am. Ceram. Soc.* 1998;81:2053–60.
- [75] Holz, D. *Herstellung und Charakterisierung von reaktionsgebundenen Al₂O₃-Keramiken (RBAO-Verfahren) am Beispiel des Systems Al₂O₃/ZrO₂*. PhD Thesis. Düsseldorf: VDI-Verlag GmbH; 1994.
- [76] Suvaci, E.; Messing, G.L. Processing parameter effects on the reaction bonding of aluminum oxide process. *J. Mater. Sci.* 1999;34:3249–61.
- [77] Coronel, J.J. *Endkonturnahe Formgebung keramischer Bauteile über pulverbeladene Wachssuspensionen*. PhD Thesis. Düsseldorf: VDI Verlag GmbH; 2004.
- [78] Leverkus, M.; Coronel, J.; Hupert, D.; Gorlov, I.; Janssen, R.; Claussen, N. Novel binder system based on paraffin-wax for low-pressure injection molding of metal-ceramic powder mixtures. *Adv. Eng. Mater.* 2001;3:995–8.
- [79] Wendorff, J.; García, D.E.; Janssen, R.; Claussen, N. Sapphire-fiber reinforced RBAO. *Ceram. Eng. Sci. Proc.* 1994;15:364–70.
- [80] Wendorff, J.; Janssen, R.; Claussen, N. Model experiments on pure oxide composites. *Mater. Sci. Eng., A* 1998;A250:186–93.
- [81] Goushegir, S.M.; Guglielmi, P.O.; da Silva, J.G.P.; Hablitzel, M.P.; Hotza, D.; Al-Qureshi, H.A.; Janssen, R. Fiber-matrix compatibility in an all-oxide ceramic composite with RBAO matrix. *J. Am. Ceram. Soc.* 2012;95:159–64.

- [82] Schmücker, M.; Mechnich, P. Microstructural coarsening of Nextel™ 610 fibers embedded in alumina-based matrices. *J. Am. Ceram. Soc.* 2008;91:1306–8.
- [83] Özcoban, H.; Salikov, V.; Jelitto, H.; Schneider, G.A. Experimental crack front investigation of unpoled soft lead zirconate titanate (PZT) using the Single Edge V-Notched Beam (SEVNB) method. *Exp. Mech.* 2012;52:1565–8.
- [84] Yilmaz, E.D.; Mgbemere, H.E.; Özcoban, H.; Fernandes, R.P.; Schneider, G.A. Investigation of fracture toughness of modified $(K_xNa_{1-x})NbO_3$ lead-free piezoelectric ceramics. *J. Eur. Ceram. Soc.* 2012;32:3339–44.
- [85] Jelitto, H.; Felten, F.; Swain, M.V.; Balke, H.; Schneider, G.A. Measurement of the total energy release rate for cracks in PZT under combined mechanical and electrical loading. *J. Appl. Mech.* 2007;74:1197–211.
- [86] Fett, T.; Munz, D. Stress intensity factors and weight functions. *Computational Mechanics Publications* 1997.
- [87] Oliver, W.C.; Pharr, G.M. Measurement of hardness and elastic modulus by instrumented indentation: Advances in understanding and refinements to methodology. *J. Mater. Res.* 2004;19:3–20.
- [88] Yoshimura, H.N.; Molisane, A.L.; Siqueira, G.R.; de Camargo, A.C., Narita, N.E.; Cesar, P.F.; Goldenstein, H. Effect of porosity on the mechanical properties of a high purity alumina. *Cerâmica* 2005;51:239–51.
- [89] Puchegger, S.; Dose, F.; Loidl, D.; Kromp, K.; Janssen, R., Brandhuber, D.; Hüsing, N. et al. The dependence of the elastic moduli of reaction bonded alumina on porosity. *J. Eur. Ceram. Soc.* 2007;27:35–9.
- [90] Schmücker, M.; Mechnich, P. Improving the microstructural stability of Nextel™ 610 alumina fibers embedded in a porous alumina matrix. *J. Am. Ceram. Soc.* 2010:1–3.
- [91] Coronel, J.J.; Janssen, R.; Claussen, N. Conformado de piezas cerámicas a partir de suspensiones parafínicas cargadas con polvos. *Bol. Soc. Esp. Ceram.* 2004;48:843–8.
- [92] Toki Sangyo. Food products viscosity data chart. [June 16, 2014]; Available from: <http://www.tokisangyo.com/pdf/paper/syokuhin-data.pdf>.

- [93] Aström, B.T. *Manufacturing of polymer composites*. Cheltenham: Nelson Thornes Ltd; 2002.
- [94] Bigg, D.M.; Preston, J.R. Stamping of thermoplastic matrix composites. *Polym. Compos.* 1989;10.
- [95] Cabrera, N.; Alcock, B.; Loos, J.; Peijs, T. Processing of all-polypropylene composites for ultimate recyclability. *Proc. Instn Mech. Engrs, Part L: J. Materials: Design and Applications* 2004;218:145–55.
- [96] Guglielmi, P.O.; Nunes, G.F.; Hablitzel, M.P.; Hotza, D.; Janssen, R. Production of oxide ceramic matrix composites by a prepreg technique. *Mater. Sci. Forum* 2012;727-728:556–61.
- [97] Guglielmi, P.O.; Blaese, D.; Hablitzel, M.P.; Nunes, G.F.; Lauth, V.R.; García, D.; Al-Qureshi, H.A. et al. Multilayered fiber-reinforced oxide composites produced by lamination of thermoplastic prepregs. *Adv. Sci. Technol.* 2014;89:145–50.
- [98] Weiß, R. CMC and C/C-SiC-Fabrication. *Adv. Sci. Eng.* 2006;50:130–40.
- [99] Guglielmi, P.O.; Blaese, D.; Hablitzel, M.P.; Nunes, G.F.; Lauth, V.R.; Hotza, D.; Al-Qureshi, H.A. et al. Microstructure and flexural properties of multilayered fiber-reinforced oxide composites fabricated by a novel lamination route. *Ceram. Int.* 2015;41:7836-46
- [100] GIMP. [July 06, 2014]; Available from: <http://www.gimp.org/>.
- [101] Rasband, W.S. ImageJ, U.S. National Institutes of Health, Bethesda, Maryland, USA, <http://imagej.nih.gov/ij/>, 1997-2014
- [102] Lange, F.F.; Yamagushi, T.; Davis, B.I.; Morgan, P.E.D. Effect of ZrO₂ inclusions on the sinterability of Al₂O₃. *J. Am. Ceram. Soc.* 1988;71:446–8.
- [103] Wang, J.; Raj R. Activation Energy for the Sintering of Two-Phase Alumina/Zirconia Ceramics. *J. Am. Ceram. Soc.* 1991;74:1959–63.
- [104] Masia, S.; Calvert, P.D.; Rhine, W.E.; Bowen, H.K. Effect of oxides on binder burnout during ceramics processing. *J. Mater. Sci.* 1989;24:1907–12.
- [105] Yang, T.C.K.; Chang, W.H.; Viswanath, D.S. Thermal degradation of poly(vinyl butyral) in alumina, mullite and silica composites. *J. Therm. Anal.* 1996;47:697–713.



- [106] Petrovic, J.; Thomas, G. Reaction of aluminum with water to produce hydrogen: A study of issues related to the use of aluminum for on-board vehicular hydrogen storage. US Department of Energy; 2008.
- [107] Guglielmi, P.O.; Silva, W.R.L.; Repette, W.L., Hotza, D. Porosity and mechanical strength of an autoclaved clayey cellular concrete. *Adv. Civ. Eng.* 2010;2010:1–6.
- [108] Scheffler, M.; Colombo, P. (eds.). *Cellular Ceramics: Structure, Manufacturing, Properties and Applications*. Weinheim: WILEY-VCH Verlag GmbH & Co; 2005.
- [109] Chaklader, A.C.D. Hydrogen generation from water split reaction;C01B 3/08(US 6440385 B1); 2000.
- [110] Deng, Z.; Liu, Y.; Tanaka, Y.; Ye, J.; Sakka, Y. Modification of Al particle surfaces by gamma-Al₂O₃ and its effect on the corrosion behavior of Al. *J. Am. Ceram. Soc.* 2005;88:977–9.
- [111] Deng, Z.; Ferreira, J.M.F.; Tanaka, Y.; Ye, J. Physicochemical mechanism for the continuous reaction of gamma-Al₂O₃-modified aluminum powder with water. *J. Am. Ceram. Soc.* 2007;90:1521–6.
- [112] Bunker, B.C.; Nelson, G.C.; Zavadil, K.R.; Barbour, J.C.; Wall, F.D.; Sullivan, J.P. Hydration of passive oxide films on aluminum. *J. Phys. Chem., B* 2002;106:4705–13.
- [113] Digne, M.; Sautet, P.; Raybaud, P.; Toulhoat, H.; Artacho E. Structure and stability of aluminum hydroxides: A theoretical study. *J. Phys. Chem., B* 2002;106:5155–62.
- [114] Wu, S.; Holz, D.; Claussen, N. Mechanisms and kinetics of reaction-bonded aluminum oxide ceramics. *J. Am. Ceram. Soc.* 1993;76:970–80.
- [115] Gitzen, W.H. *Alumina as a Ceramic Material*. Columbus, Ohio: The American Ceramic Society Inc; 1970.
- [116] Sato, T. Thermal decomposition of aluminium hydroxides. *J. Therm. Anal.* 1987;32:61–70.
- [117] Temuujin, J.; Coronel, J.J.; Minjigmaa, A.; Mackenzie, K. Water content and water evolution from reaction-bonded aluminum oxide (RBAO) powder precursors. *Int. J. Appl. Ceram. Technol.* 2008;5:289–94.

- [118] ASTM International. Standard test method for flexural properties of continuous fiber-reinforced advanced ceramic composites(C 1341-00): ASTM; 2000.
- [119] Department of Defense United States of America. Composite Materials Handbook-MIL 17: Volume I: Guidelines for Characterization of Structural Materials: Technomic Publishing Co., Inc. & Materials Science Corporation; 1999.
- [120] Haslam, J.J.; Berroth, K.E.; Lange, F.F. Processing and properties of an all-oxide composite with a porous matrix. *J. Eur. Ceram. Soc.* 2000;20:607–18.
- [121] Zok, F.W.; Levi, C.G. Mechanical properties of porous-matrix ceramic composites. *Adv. Eng. Mater.* 2001;3:15–23.
- [122] Dauskardt, R.H.; Lane, M.; Ma, Q.; Krishna, M. Adhesion and debonding of multi-layer thin film structures. *Eng. Fract. Mech.* 1998;61:141–62.
- [123] Al-Qureshi, H.A.; Stael, G.C. Modified rule of mixtures for natural fiber composites. In: Cloutier L, Rancourt D, editors. *CANCAM 97: Proceedings 16th Canadian Congress of Applied Mechanics: CANCAM Central Committee*; 1997. p. 49–50.
- [124] Hodgkinson, J.M. *Mechanical Testing of Advanced Fiber Composites*. 1st ed.: Woodhead Publishing; 2000.
- [125] Folsom, C.A.; Zok, F.W.; Lange, F.F. Flexural Properties of Brittle Multilayer Materials: I, Modeling. *J. Am. Ceram. Soc.* 1994;77:689–96.
- [126] Hofmann, S.; Öztürk, B.; Koch, D.; Voggenreiter, H. Experimental and numerical evaluation of bending and tensile behaviour of carbon-fibre reinforced SiC. *Composites Part A* 2012;43:1877–85.
- [127] Steif, P.S.; Trojnacki, A. Bend strength versus tensile strength of fiber-reinforced ceramics. *J. Am. Ceram. Soc.* 1994;77:221–9.
- [128] Folsom, C.A.; Zok, F.; Lange, F.F. Mechanical behavior of a laminar ceramic/fiber-reinforced epoxy composite. *J. Am. Ceram. Soc.* 1992;75:2969–75.
- [129] Varna, J.; Joffe, R.; Berglund, L.A.; Lundström, T.S. Effect of voids on failure mechanisms in RTM laminates. *Compos. Sci. Technol.* 1995;53:241–9.



- [130] Jeong, H. Effects of voids on the mechanical strength and ultrasonic attenuation of laminated composites. *J. Compos. Mater.* 1997;31:276–92.
- [131] Costa, M.L.; de Almeida, S.F.M.; Rezende, M.C. The influence of porosity on the interlaminar shear strength of carbon/epoxy and carbon/bismaleimide fabric laminates. *Compos. Sci. Technol.* 2001;61:2101–8.
- [132] Hagstrand, P.; Bonjour, F.; Manson, J.E. The influence of void content on the structural flexural performance of unidirectional glass fiber reinforced polypropylene composites. *Composites Part A* 2005;36:705–14.
- [133] Knoll, J. *Analysis of damage mechanisms in CFRP crossply laminates through dynamic and flexural testing monitored with infrared techniques.* Diplomarbeit. Institute of Product Development and Mechanical Engineering Design, Hamburg University of Technology.



Curriculum Vitae

Name	de Oliveira Guglielmi
Vorname	Paula
Geburtsdatum	16.09.1984
Geburtsort, -land	Criciúma/SC, Brasilien
03.1991 – 11.2001	“Colégio Marista” in Criciúma/SC, Brasilien
02.2002 – 05.2007	Studium an der “Universidade Federal de Santa Catarina” in Florianópolis/SC, Brasilien Studiengang: Werkstoffingenieurwesen Abschluss: Bachelor
08.2005 – 07.2006	Praktikum am Fraunhofer Institut für Produktionstechnologie in Aachen
10.2007 – 10.2009	Studium an der Technischen Universität Hamburg-Harburg Studiengang: „Joint European Master in Materials Science“ Abschluss: Master
08.2008 – 01.2009	Austauschsemester an der Aalborg Universität im Rahmen des „Joint European Master in Materials Science“ in Aalborg, Dänemark
11.2009 – 04.2014	Wissenschaftliche Mitarbeiterin am Institut für Keramische Hochleistungswerkstoffe an der Technischen Universität Hamburg-Harburg
08.2014 – heute	Wissenschaftliche Mitarbeiterin am Institut für Werkstoffforschung, Werkstoffmechanik, Abteilung für Experimentelle Werkstoffmechanik am Helmholtz-Zentrum Geesthacht





